

Air Force Institute of Technology

AFIT Scholar

---

Theses and Dissertations

Student Graduate Works

---

9-2003

## Electron Paramagnetic Resonance Spectroscopy and Hall Effect Studies of the Effects of Low Energy Electron Energy on Gallium Nitride (GAN)

Kevin D. Greene

Follow this and additional works at: <https://scholar.afit.edu/etd>



Part of the [Nuclear Engineering Commons](#)

---

### Recommended Citation

Greene, Kevin D., "Electron Paramagnetic Resonance Spectroscopy and Hall Effect Studies of the Effects of Low Energy Electron Energy on Gallium Nitride (GAN)" (2003). *Theses and Dissertations*. 4138.  
<https://scholar.afit.edu/etd/4138>

This Dissertation is brought to you for free and open access by the Student Graduate Works at AFIT Scholar. It has been accepted for inclusion in Theses and Dissertations by an authorized administrator of AFIT Scholar. For more information, please contact [richard.mansfield@afit.edu](mailto:richard.mansfield@afit.edu).



**ELECTRON PARAMAGNETIC RESONANCE SPECTROSCOPY  
AND HALL EFFECT STUDIES OF THE EFFECTS OF LOW  
ENERGY ELECTRON IRRADIATION ON GALLIUM NITRIDE  
(GAN)**

DISSERTATION

Kevin D. Greene, Major, USAF

AFIT/DSP/ENP/03-02  
DEPARTMENT OF THE AIR FORCE  
AIR UNIVERSITY

**AIR FORCE INSTITUTE OF TECHNOLOGY**

Wright-Patterson Air Force Base, Ohio

APPROVED FOR PUBLIC RELEASE; DISTRIBUTION UNLIMITED

## Report Documentation Page

*Form Approved*  
OMB No. 0704-0188

Public reporting burden for the collection of information is estimated to average 1 hour per response, including the time for reviewing instructions, searching existing data sources, gathering and maintaining the data needed, and completing and reviewing the collection of information. Send comments regarding this burden estimate or any other aspect of this collection of information, including suggestions for reducing this burden, to Washington Headquarters Services, Directorate for Information Operations and Reports, 1215 Jefferson Davis Highway, Suite 1204, Arlington VA 22202-4302. Respondents should be aware that notwithstanding any other provision of law, no person shall be subject to a penalty for failing to comply with a collection of information if it does not display a currently valid OMB control number.

1. REPORT DATE <b>AUG 2003</b>	2. REPORT TYPE	3. DATES COVERED -	
4. TITLE AND SUBTITLE <b>ELECTRON PARAMAGNETIC RESONANCE SPECTROSCOPY AND HALL EFFECT STUDIES OF THE EFFECTS OF LOW ENERGY ELECTRON ENERGY ON GALLIUM NITRIDE (GAN)</b>		5a. CONTRACT NUMBER	
		5b. GRANT NUMBER	
		5c. PROGRAM ELEMENT NUMBER	
6. AUTHOR(S) <b>KEVIN GREENE</b>		5d. PROJECT NUMBER	
		5e. TASK NUMBER	
		5f. WORK UNIT NUMBER	
7. PERFORMING ORGANIZATION NAME(S) AND ADDRESS(ES) <b>Air Force Institute of Technology, 2950 Hobson Way, Wright-Patterson AFB, OH, 45433-7765</b>		8. PERFORMING ORGANIZATION REPORT NUMBER <b>AFIT/DSP/ENP/03-02</b>	
9. SPONSORING/MONITORING AGENCY NAME(S) AND ADDRESS(ES)		10. SPONSOR/MONITOR'S ACRONYM(S)	
		11. SPONSOR/MONITOR'S REPORT NUMBER(S)	
12. DISTRIBUTION/AVAILABILITY STATEMENT <b>Approved for public release; distribution unlimited</b>			
13. SUPPLEMENTARY NOTES			
14. ABSTRACT <b>The nature of native donors in GaN, types and interactions of radiation-induced defects, and damage creation coefficients for 1.0 MeV electron irradiation have been ascertained by the concerted application of electron paramagnetic resonance spectroscopy and Hall effect measurements to virgin and electron-irradiated GaN epilayers. Samples produced via molecular beam epitaxy and hydride vapor phase epitaxy, both silicon doped and nominally undoped, were subjected to Van de Graff generator produced monoenergetic electron beams with total fluences of <math>10^{16}</math>- <math>10^{18}</math> electrons/cm<sup>2</sup>. Nitrogen vacancies are rejected as a possible cause of n-type conductivity in nominally undoped GaN due to the decrease of shallow donor populations following irradiation. Damage constants for a donor-defect complex formation or defect compensation are found to be approximately 0.15 cm<sup>-1</sup>. Identification by resolved hyperfine splitting is accomplished for radiation-induced Ga interstitial complexes.</b>			
15. SUBJECT TERMS			
16. SECURITY CLASSIFICATION OF:			17. LIMITATION OF ABSTRACT
a. REPORT <b>unclassified</b>	b. ABSTRACT <b>unclassified</b>	c. THIS PAGE <b>unclassified</b>	
			18. NUMBER OF PAGES <b>186</b>
			19a. NAME OF RESPONSIBLE PERSON

The views expressed in this thesis are those of the author and do not reflect the official policy or position of the United States Air Force, Department of Defense, or the United States Government.

AFIT/DSP/ENP/03-02

**ELECTRON PARAMAGNETIC RESONANCE SPECTROSCOPY  
AND HALL EFFECT STUDIES OF THE EFFECTS OF LOW  
ENERGY ELECTRON IRRADIATION ON GALLIUM NITRIDE  
(GAN)**

DISSERTATION

Presented to the Faculty

Graduate School of Engineering and Management

Air Force Institute of Technology

Air University

Air Education and Training Command

in Partial Fulfillment of the Requirements for the

Degree of Doctor of Philosophy

Kevin D. Greene, BS, MS

Major, USAF

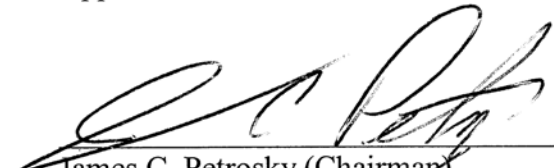
September 2003

APPROVED FOR PUBLIC RELEASE; DISTRIBUTION UNLIMITED

**Electron Paramagnetic Resonance Spectroscopy and Hall Effect  
Studies of the Effects of Low Energy Electron Irradiation on  
Gallium Nitride (GaN)**

Kevin D. Greene, BS, MS  
Major, USAF

Approved:

  
James C. Petrosky (Chairman)

Date

04SEP03

  
Meir Pachter (Dean's Representative)

16 Sept. 03

  
Robert L. Hengehold (Member)


4 Sep '03

  
David E. Weeks (Member)

4 Sep 03

  
Mark E. Oxley (Member)

4 Sep 03

Accepted: 

Robert A. Calico, Jr.  
Dean, Graduate School of Engineering and Management

9 Sept 03

Date

## **Abstract**

Irradiation effects on the wide-bandgap semiconductor material GaN are of interest to the USAF due to this material's applicability for a wide range of on-orbit uses. Irradiation is also a valuable tool in analyzing the damage and defect formation dynamics of the material which is of great use in determining and correcting deficiencies in material growth processes.

GaN samples representing several different growth methods and doping profiles were irradiated by 1.0 – 1.5 MeV electron beams to induce defects such as vacancies and interstitial atoms in the material. Following irradiation, the samples were analyzed using Electron Paramagnetic Spin Resonance (EPR) spectroscopy to determine effects of the irradiation, with particular attention to the effects of irradiation on the shallow donors in the material.

EPR allows the direct inspection of paramagnetic impurity or defect sites, providing information on site density as well as, in some cases, identity. Samples subjected to EPR analysis prior to irradiation show a strong signal attributed to the shallow donor in GaN that is without resolved hyperfine structure. Following low-temperature irradiation with 1.0 MeV electrons to a total dose of approximately 40 MRad (GaN), the same samples showed a marked decrease in the shallow donor signal and the introduction of a broad EPR signal with resolved hyperfine structure.

The decrease in the shallow donor signals is attributed to the formation of a deep band-gap complex of the nitrogen interstitial with the shallow donor sites, perhaps in

combination with compensation by defect-related centers. The damage constant for the formation of this process is calculated as  $0.14\text{cm}^{-1}$ . This *decrease* in the shallow donor concentration in undoped GaN demonstrates that the native shallow donor in *n*-type GaN *cannot* be the nitrogen vacancy, as has been previously suggested.

A broad EPR signal imparted by low-temperature 1.0 MeV electron irradiation is identified as a gallium interstitial by modeling of the hyperfine spectrum. The Breit-Rabi formula is used with parameters characteristic of the two naturally occurring gallium isotopes to reproduce the observed spectrum. This is the first observation of the gallium interstitial by EPR, as well as the first simultaneous resolvable measurement of nitrogen and gallium sublattice damage in a single sample following irradiation.



AFIT/DSP/ENP/03-02

Dedicated to my family

## Acknowledgements

Good research is not done by individuals, but by the families, advisors, and team members who support the researcher. Thus, in any work of ground-breaking research, much of the responsibility for success must be shared with those who support and assist the researcher.

However, even in a work such as this there is some credit that must be shared, if those responsible are willing to reveal their identities. In light of this, the following individuals have proven critical to the successful completion of this research effort and instrumental in the maintenance of the researcher's sanity.

LTC James Petrosky, my advisor, provided sound technical advice, but perhaps more importantly kept me motivated and focused when things seemed bleak. While his efforts in securing resources saved this project, his encouragement and insight were equally valuable.

Dr. William Carlos of the Naval Research Laboratory allowed this neophyte researcher to commandeer his EPR lab for days at a time, allowing me to collect the required data. His insight into the conduct of EPR spectroscopy and helpful advice also paved the way for a successful conclusion to this research.

Dr. Gary Farlow of the Wright State University was responsible for providing the Van de Graff facility. He arranged the beam time, operator certification, and experimental guidance required to safely and effectively conduct the electron irradiations we needed.

Dr. David Look of the Wright State University provided not only samples of the highest quality GaN available, but the use of his Hall measurement facility and insight into the conduct of Hall analysis and the interactions of radiation in GaN.

Dr. Joe Van Nostrand provided several batches of samples – he never failed to come up with a set of samples to fulfill our requests. Without this resource, this research would never have gotten off of the ground. Dr. Omar Manasreh of the University of New Mexico also provided samples, useful discussions about radiation interactions, and the offer of lab space and time.

Dr. Mary Ellen Zvanut, of the University of Alabama, Birmingham was instrumental in getting this research effort started off on the right foot. She shared insights and resources to get me started with the EPR spectroscopy.

Dr. Robert Mantz, Dr. Joel Johnson, and Dr. Mike Donley of the Air Force Research Laboratory, MLBT were responsible for letting me use their EPR spectrometer and were patient with the scattering of dewars, gas tanks, transfer lines, tools and cords in their lab space. They never failed to offer an encouraging word and their assistance.

Some of the most important people to the successful conduct of any research project are the technicians that help ensure that the equipment continued to function, measurements were conducted on time, and samples were prepared. Mr. Eric Taylor was instrumental in making sure equipment repairs were conducted correctly and that the LHe was in the right place. Mr. Tim Cooper conducted all of the Hall measurements in a quick fashion, never failing to work us into his busy schedule. Mr. Larry Callaghan was responsible for the dicing of the samples. Mr. Russ Hastings and his crew in the AFIT

Model Shop were very helpful in creating and modifying whatever experimental equipment I dreamt up.

My family may never know how helpful they were in getting this research done. Their patience with my extended absences and commitment to see the effort through were critical to this entire effort.

God gave me the opportunity and strength to complete this course, as in all things. It is to my Savior, Jesus Christ, that my thanks will always be and will always fall short of what He has done for me.

My thanks go out to everyone listed above, and to anyone I may have missed. Your efforts kept this research on track and maintained my level of sanity.

# Table of Contents

	Page
Abstract .....	iv
Dedication .....	vi
Acknowledgements .....	vii
List of Figures .....	xii
List of Tables.....	xix
List of Symbols .....	xx
I. Introduction.....	1
II. Background.....	4
Gallium Nitride (GaN) Applications And Testing.....	4
Physical Properties of GaN .....	5
GaN Growth Methods .....	15
Molecular Beam Epitaxy (MBE) .....	15
Hydride Vapor Phase Epitaxy (HVPE).....	16
Metal-Organic Vapor Phase Epitaxy (MOVPE).....	17
Radiation Interactions .....	18
Electron Paramagnetic Resonance (EPR) Spectroscopy.....	23
Applicability of EPR Spectroscopy to Radiation Effects Studies.....	30
EPR Measurements in GaN.....	31
Hall Effect Measurements .....	33
III. Theoretical Considerations.....	36
EPR Theoretical Considerations .....	36
Donor Passivation Models .....	36
Development and Application of the Hyperfine Coupling Constants.....	45
Spin Hamiltonian and Resonance Analysis for the GaN System.....	49

Hall Effect Analyses.....	56
IV. Experimental Procedures .....	65
Sample Preparation and Handling.....	65
Irradiation Experiments.....	68
Dosimetry .....	74
Spectroscopy .....	78
Hall Effect Measurements .....	84
V. Experimental Results.....	85
Sapphire (Al <sub>2</sub> O <sub>3</sub> ) Results.....	85
MBE GaN On Sapphire Substrate Results .....	87
Pre-Irradiation EPR Spectroscopy.....	87
Post-Irradiation EPR Spectroscopy .....	90
Free-Standing GaN Sample Results .....	112
Pre-Irradiation EPR Spectroscopy.....	112
Post-Irradiation EPR Spectroscopy .....	113
Supporting Experimental Results.....	117
Pre-Irradiation Hall Effect Measurements .....	117
Post-Irradiation Hall Effect Measurements .....	125
VI. Analysis and Discussion .....	130
Hall Effect Measurements .....	130
EPR Spectroscopy .....	134
Hyperfine Structure Analysis .....	148
VII. Conclusions.....	155
Experimental Conclusions.....	155
Proposed Experimental Direction .....	156
Bibliography.....	158

## List of Figures

Figure	Page
1. Estimated fundamental bandgap energy dependence upon temperature in wurtzite phase GaN. Dotted vertical lines represent liquid He, liquid N, and room temperature points. Data shown here was generated by equation 1. ....	7
2. Wurtzite GaN band-structure as computed by Suzuki [14], et al via a plane-wave pseudopotential calculation method. All energy values are at 300°K. ....	7
3. Calculated atomic locations for wurtzite crystal structure of GaN. The graph on the right illustrates the orientation of the (0001) direction, with Ga represented by black and N by white balls. Axis units are in angstroms. Plot on the left is presented looking down the (000 $\bar{1}$ ) direction for a Ga face surface. ....	8
4. Temperature dependence of the intrinsic carrier concentration in GaN [12]. ....	11
5. Normalized breakdown field ( $F_i$ ) and voltage ( $V_i$ ) in GaN samples. Normalization is to $1\text{-}2\cdot 10^6$ V/cm and 42 V respectively. Samples are p <sup>+</sup> -p-n diodes. [12].....	13
6. Maximum energy transfer for gallium and nitrogen as a function of the incident electron energy. The average and minimum displacement energies for both gallium and nitrogen are shown as horizontal lines. Values are calculated via Equation 4. ....	20
7. Band Gap states of GaN, with as-grown states depicted by solid lines and radiation induced effects by dotted lines. [38] [13] .....	22
8. Relationship between magnetic field modulation (vertical waveform), absorption spectrum ( $Y(x)$ ), and resultant signal (horizontal waveform). [44].....	30
9. Results of the numerical solution of equation 20 for different initial donor concentrations. For each of the pre-irradiation donor concentrations the virgin EPR system response is shown along with the post-irradiation results for the “complex only” model and the “complex + compensation” model.....	43
10. Breit-Rabi energy levels for the coupling of the a single electron with the spin 3/2 nucleus <sup>69</sup> Ga. Resonance locations for 9.5GHz microwave photons are shown as dashed vertical lines. The spacing between resonance locations is non-symmetric, as shown in the indicated intervals. ....	54

11. Hall measured mobility data from sample A342, pre- and post-correction. The effect of the degenerate layer in skewing the mobility measurement downward is apparent.....	59
12. Hall carrier concentration for sample A342, pre- and post-correction. The effect of the degenerate interfacial layer is apparent at low temperatures (high 1/T). The corrected data are recognized as a standard double shallow donor case. ....	60
13. Examples of the donor fitting model, curves labeled <i>A</i> are one donor models, <i>B</i> are two donor models, and <i>C</i> curves are three donor models. Curves labeled <i>1</i> are for acceptor densities of $1.5 \times 10^{16} \text{ cm}^{-3}$ and the curves labeled with <i>2</i> are for acceptor concentrations of $5 \times 10^{15} \text{ cm}^{-3}$ . ....	63
14. Cold head and sample mount assembly. ....	70
15. Typical temperature profile for long irradiations. Data is from a.....	71
16. Electron stopping powers as calculated by XGEN for materials of interest.....	76
17. Dose deposition profiles for GaN (2 $\mu\text{m}$ ) on Al <sub>2</sub> O <sub>3</sub> (1 mm) for particle energies of 0.5, 1.0, and 1.5 MeV. Calculation was performed using 200,000 histories in 20 batches in TIGER.....	77
18. Dose curves (MRad(GaN) vs $\phi$ ) produced via TIGER. Results for 2 $\mu\text{m}$ GaN films on Al <sub>2</sub> O <sub>3</sub> are shown as solid lines and filled symbols. Results for 200 $\mu\text{m}$ free-standing layers are shown with dashed lines and open symbols. ....	78
19. Sample mount and cooling flow arrangement. Open-ended tube arrangement shown is required to cool samples to near 4K. ....	80
20. Wide field scans of sapphire substrate materials at approximately 30K. Marked angular anisotropy is evident in this series of scans. ....	86
21. Representative EPR scan of the signal originating in quartz sample tube (tube #2). The resultant signal is isotropic and not easily saturated. This spectrum was obtained at approximately 4K. ....	89
22. Spectra from irradiated GaN on sapphire (9-30-02). Spectra are shown for various angles ( $\theta$ ) with respect to the instrument magnetic field. ....	91
23. EPR absorption signal imparted to GaN/sapphire signals after irradiation (9-30-02). This figure shows the non-symmetric form of the signal, with a slight hump on the high-g side of the signal, and a deeper low-g side, characteristic of multiple overlapping absorption signals. ....	92



24. EPR spectrum of crystallized vacuum grease after irradiation. The signal shown here is identical to that identified in earlier GaN samples (see Figure 23).....	94
25. Comparison of virgin and irradiated ( $\phi = 10^{16} e^- / cm^2$ ) GaN on sapphire (Sample Aa342-1/2). Measurements were conducted on the same day. Note that the data of the lower plot display spurious signals (at $g=1.93$ and $g=1.985$ ) as well as differences in $TO_1$ linewidths and lineshapes. Magnetic field angles of $0^\circ$ to $90^\circ$ are shown in each plot.....	97
26. Temperature and beam current profile for 11 April 2003 Irradiation ( $\phi \approx 1 \times 10^{17} e^- / cm^2$ ). Temperature scale is on the left axis, beam current scale is on the right axis. Temperature spike at 0.75 hours is due to loss of chamber vacuum.....	98
27. Comparison of virgin and irradiated ( $\phi \approx 10^{17} e^- / cm^2$ ) GaN on Sapphire (Sample A342). Measurements conducted under identical conditions, same day. Magnetic field angles of $0^\circ$ to $90^\circ$ are shown in each plot. ....	99
28. Comparison of virgin and irradiated ( $\phi \approx 10^{17} e^- / cm^2$ ) GaN on Sapphire (Sample A351). Measurements conducted under identical conditions, same day. Variation in the $g=1.95$ signal location is due to rotational anisotropy. Experimental difficulties resulted in collection of only two good spectra in the irradiated sample. Magnetic field angles of $0^\circ$ to $90^\circ$ are shown in each plot. ....	100
29. Temperature and beam current profile for 12 May 2003 Irradiation ( $\phi \approx 1 \times 10^{18} e^- / cm^2$ ). Temperature scale is the left axis, beam current scale is on the right axis.....	102
30. Comparison of virgin and irradiated ( $\phi \approx 10^{18} e^- / cm^2$ ) GaN on Sapphire (Sample A363). Measurements conducted under identical conditions, same day. Variation in the $g=1.95$ signal location is due to rotational anisotropy. Magnetic field angles of $0^\circ$ to $90^\circ$ are shown in each plot. ....	104
31. Comparison of virgin and irradiated ( $\phi \approx 10^{18} e^- / cm^2$ ) GaN on Sapphire (Sample A350). Measurements conducted under identical conditions, same day. Variation in the $g=1.95$ signal location is due to rotational anisotropy. Magnetic field angles of $0^\circ$ to $90^\circ$ are shown in each plot. ....	105

32. Comparison of A350 after 17 hours room temperature annealing with virgin and irradiated ( $\phi \approx 10^{18} e^- / cm^2$ ) GaN on Sapphire. Variation in the $g=1.95$ signal location is due to rotational anisotropy. The lower curve is after annealing. Magnetic field angles of $0^\circ$ to $90^\circ$ are shown in each plot. ....	106
33. Comparison of virgin and irradiated ( $\phi \approx 10^{18} e^- / cm^2$ ) GaN on Sapphire (Sample A351). Measurements conducted under identical conditions, same day. Variation in the $g=1.95$ signal location is due to rotational anisotropy. Magnetic field angles of $0^\circ$ to $90^\circ$ are shown in each plot. ....	107
34. Comparison of virgin and irradiated ( $\phi \approx 10^{18} e^- / cm^2$ ) GaN on Sapphire (Sample A342-1/2). Measurements conducted under identical conditions, same day. Variation in the $g=1.95$ signal location is due to rotational anisotropy. Magnetic field angles of $0^\circ$ to $90^\circ$ are shown in each plot. ....	108
35. Comparison of virgin and irradiated ( $\phi \approx 10^{18} e^- / cm^2$ ) GaN on Sapphire (Sample A342-1). Measurements conducted under similar experimental conditions, on identical sample subsections. Variation in the $g=1.95$ signal location is due to rotational anisotropy. Magnetic field angles of $0^\circ$ to $90^\circ$ are shown in each plot. ...	109
36. Comparison of scaled, integrated EPR signals (pre- and post-irradiation) versus post-growth room temperature carrier concentration as determined by Hall measurements. Note that sample A342 was probably under-dosed in this exposure. Sample SB0009B has been adjusted for the increased volume of the sample. ....	110
37. Wide magnetic field scan ( $\vec{B} \perp \vec{c}$ ) of sample A363-1 after irradiation ( $\phi = 10^{18} e^- / cm^2$ ). The sharp signal appearing at approximately 3400 G is the ubiquitous tube signal. Magnetic field units are used as the dependent variable due to the width of the scan. ....	111
38. Comparison of virgin and irradiated ( $\phi \approx 10^{18} e^- / cm^2$ ) free-standing GaN (Sample SB0009B-1). Measurements conducted under similar experimental conditions, same sample subsection. Variation in the $g=1.95$ signal location is due to rotational anisotropy. Measurements were conducted at 4K sample temperature. ....	114
39. Comparison of virgin and irradiated ( $\phi \approx 10^{18} e^- / cm^2$ ) free-standing GaN (Sample SB0009B-1). Measurements conducted under similar experimental conditions, same sample subsection. Variation in the $g=1.95$ signal location is due to rotational anisotropy. Measurements were conducted at 22K sample temperature. ....	115

40. Wide magnetic field scan ( $\bar{B} \perp \bar{c}$ ) of sample SB0009B-11 after irradiation ( $\phi = 10^{18} e^- / cm^2$ ). The sharp signal appearing at approximately 3400 G is the ubiquitous tube signal. Magnetic field units are used as the dependent variable due to the width of the scan. ....	116
41. Corrected Hall mobilities of virgin materials used in the current study. Good Hall data was not available on SB0009B. Measurements are limited to the 30K-320K regime due to the use of 20K measurements to perform multiple-layer corrections. ....	117
42. Multi-layer corrected Hall carrier concentrations of virgin materials used in the current study. Good Hall data was not available on SB0009B. Hall data is limited to the 30K-320K regime due to the need to use the lowest T points in the multi-layer analysis. ....	119
43. Pre-irradiation temperature dependent Hall data for sample A363. Model (line) is for a two donor fit with ( $N_{D1}=6.3E16$ , $E_{D1}=22.9$ meV, $N_{D2}=5.5E16$ , $E_{D2}=79.2$ meV, $N_A=2.3E15$ ). ....	120
44. Pre-irradiation temperature dependent Hall data for sample A350. Model (line) is for a two donor fit with ( $N_{D1}=2.18E17$ , $E_{D1}=8.2$ meV, $N_{D2}=4E17$ , $E_{D2}=50.2$ meV, $N_A=1E15$ ). ....	121
45. Pre-irradiation temperature dependent Hall data for sample A351. Model (line) is for a two donor fit with ( $N_{D1}=3.58E17$ , $E_{D1}=5.7$ meV, $N_{D2}=6.6E17$ , $E_{D2}=47.2$ meV, $N_A=1.0E15$ ). ....	122
46. Pre-irradiation temperature dependent Hall data for sample A342. Model (line) is for a two donor fit with ( $N_{D1}=1.28E18$ , $E_{D1}=14.2$ meV, $N_{D2}=5.0E16$ , $E_{D2}=79.2$ meV, $N_A=1.0E16$ ). ....	123
47. Pre-irradiation temperature dependent Hall data for sample SB0009B. Model (line) is for a two donor fit with ( $N_{D1}=4.8E15$ , $E_{D1}=22.0$ meV, $N_{D2}=3.6E15$ , $E_{D2}=70.2$ meV, $N_A=2.1E15$ ). ....	124
48. Post-irradiation temperature dependent Hall data for sample A350. For the $\phi = 10^{17} e^- / cm^2$ case the donor fit yields ( $N_{D1}=1.9E17$ , $E_{D1}=6.0$ meV, $N_{D2}=3.60E17$ , $E_{D2}=50$ meV, $N_A=1.0E16$ ). For the $\phi = 10^{18} e^- / cm^2$ case, fit parameters are ( $N_{D1}=2.8E16$ , $E_{D1}=10.8$ meV, $N_{D2}=2.10E17$ , $E_{D2}=27.5$ meV, $N_A=1.0E16$ ). ....	126

49. Post-irradiation temperature dependent Hall data for sample A350. For the $\phi = 10^{17} e^- / cm^2$ case the donor fit yields ( $N_{D1}=3.38e17$ , $E_{D1}=5.3 meV$ , $N_{D2}=7.60E17$ , $E_{D2}=50.2meV$ , $N_A=1.0E15$ ). For the $\phi = 10^{18} e^- / cm^2$ case, fit parameters are ( $N_{D1}=1.65E17$ , $E_{D1}=8.5 meV$ , $N_{D2}=1.5E17$ , $E_{D2}=31.7meV$ , $N_A=1.5E16$ ). Low temperature data ( $10^3/T > 25$ ) in this case exhibited instabilities and may not be reliable. ....	127
50. Measured Hall mobility for sample A350, at three different radiation doses.....	128
51. Measured Hall mobility for sample A351, at three different radiation doses.....	128
52. Fit of the empirical screening equation with data from samples SB0009B, A342, A363, A350, and A351. The fit yields values of $\alpha_D = 3.071 \times 10^{-5} meV \cdot cm$ and $E_{D0} = 29.6 meV$ .....	132
53. Shallow donor concentrations as a function of the radiation fluence. ....	134
54. $SD_1$ scaled EPR magnitude plotted against the calculated shallow donor concentration. Least squares fit is shown as dotted line. ....	136
55. Pre- and post-irradiation values of the scaled EPR signal intensity as a function of the measured Hall carrier concentration. The black stars represent the post-irradiation value predicted for $\sigma = 2.34 \times 10^{-18} cm^2$ . The point labeled A351-1I(Apr) is the only irradiated data point at $\phi=10^{17} e^- / cm^2$ , all other irradiated values .....	143
56. $SD_1$ spectra in sample A351 at fluences of $0 e^- / cm^2$ , $10^{17} e^- / cm^2$ , and $10^{18} e^- / cm^2$ . Data marked with filled dots was collected in April 2003 and the data marked with open squares was collected in May 2003. Peaks have been arbitrarily placed along the x axis by varying amounts to ease comparison.....	144
57. Linear fit to the dose dependence of the shallow donor passivation in sample A351. The $R^2$ value of the linear fit is 0.9898. ....	145
58. Comparison of EPR $SD_1$ magnitudes and Hall concentration in A351 and A350, before and after irradiation to $10^{18} e^- / cm^2$ . The ratio of post-irradiation to pre-irradiation values is shown over the irradiated column in each set. ....	146
59. Measured annealing of the radiation effect in sample A350. Annealing was a room temperature over a 17 hour period.....	148

60. Breit-Rabi levels modeled for $^{69}\text{Ga}$ and $^{71}\text{Ga}$ . Vertical arrows represent the resonant magnetic field strengths corresponding to the resonant microwave energy (9.50 GHz) .....	150
61. Model output showing placement of equal width Gaussian derivative functions at the calculated resonant field values. Curves are shown for the transitions due to $^{71}\text{Ga}$ transitions (lower curve), $^{69}\text{Ga}$ transitions (middle curve), and the weighted sum of these transitions (upper curve) plotted with the experimental data for sample A363. ....	151
62. Plot A: Sample A363 widescan data (baseline subtracted). Plot B: Breit-Rabi formula model with $A_{\parallel}^{69} = 0.0530 \pm 0.001 \text{ cm}^{-1}$ and $g_{\parallel} = 2.116 \pm 0.005$ , summed for $^{69}\text{Ga}$ and $^{71}\text{Ga}$ . Vertical arrows are added to aid in comparison of the plots. ....	153

## List of Tables

Table	Page
1. Selected Physical Properties of GaN .....	6
2. Electron and Hole Effective masses in GaN (derived from [15]).....	9
3. Observed EPR Signals in GaN .....	32
4. EPR Hyperfine Parameters for Ga and N [53].....	33
5. Sample Physical Characteristics .....	67
6. VDG Irradiation Parameters .....	69
7. Irradiation Specifications .....	73
8. Material Parameters used for Dose Calculations .....	75
9. Spectrometer Parameters.....	82
10. Calculated donor densities and energies derived from two-donor fit.....	124

## List of Symbols

$\alpha_D$	empirical screening parameter (meV-cm)
$E_{D0}$	Unscreened or dilute donor activation energy (meV)
$E_D$	Effective donor activation energy (meV)
$g$	g factor
$\gamma_N$	nuclear magnetogyric ratio
$\phi, f$	electron fluence ( $e^- / cm^2$ )
$m_e, m_0$	electron mass
$m^*$	carrier effective mass
$m_v$	Density of States effective mass
$\mu$	magnetic moment
$\mu_B$	Bohr magneton
$N_A^{eff}$	Total effective acceptor concentration
$n_D$	donor concentration
$n_D^{tot}$	total donor concentration
$n_0$	pre-irradiation carrier concentration ( $cm^{-3}$ )
$\nu_{\mu w}$	microwave frequency
$R$	Hall coefficient
$SD_1$	EPR signal identified as primary shallow donor
$\sigma$	process cross section ( $cm^2$ )
$\sigma^s$	Hall sheet conductivity
$TO_1$	EPR signal identified as quartz tube signal

# I. Introduction

The rapidly developing field of wide-bandgap semiconductor research, and in particular III-Nitride research, is of current interest to the United States Air Force due to the potential applications of devices based upon these materials in militarily important environments and roles. Gallium Nitride (GaN) specifically exhibits material properties that make it well suited to applications where high-temperature operation [1], efficient high-frequency operation [2], and high-power density properties are required [3]. In addition to these unique properties, the wide bandgap of GaN is well suited for use in short wavelength opto-electronic devices [4].

The development of high-power density, high frequency devices capable of operating in high-temperature environments is readily seen to be of military interest due to the potential for rugged, all-weather communications systems, on-orbit processing and communications capabilities, and the inclusion of solid-state devices in aerospace applications where temperature and environmental conditions have previously limited their use. With these properties, GaN and related wide-bandgap semiconductors would seem to be a panacea for shortfalls in military and commercial systems design; however, growth problems have severely limited the production of efficient devices [5] and have slowed the maturity of GaN based systems to the point of commercial availability and military feasibility. Additionally, previous research has determined that native GaN materials are relatively “radiation hard”, or resistant to radiation effects [6] in comparison to other materials.



Radiation effects testing is thus important for two distinct reasons: 1) the interactions of radiation with materials sheds light upon the formation and dynamics of the types of defects that have limited device development, and 2) the supposed application of these materials to military (specifically on-orbit) applications will be aided by the existence of information on device and material radiation hardness. As devices cross the threshold from laboratory experiments to commercial production and military usefulness, as is happening at present, it is appropriate to carry out radiation effects studies to fulfill these two purposes.

This dissertation and accompanying research efforts were designed to fill this niche, offering information on the basic radiation interactions in GaN material. This will hopefully serve as a solid basis for the development of device testing research efforts (which the Department of Defense and Air Force Office of Scientific Research are currently sponsoring), as well as providing answers to some of the more contentious questions that have developed in the GaN growth community. To this end, we have applied a novel experimental methodology to the study of irradiation effects on GaN materials: the application of Electron Paramagnetic Resonance (EPR) Spectroscopy in concert with Hall effect studies of irradiated materials. The use of these methods in a “symbiotic” fashion offers more information than the application of either could produce independently.

This work provides conclusive answers some outstanding questions concerning the nature of growth problems in GaN layers, identifies some of the direct products of irradiation in these materials, and directly measures the impact of these products on material parameters which will directly impact device performance. As such, it is hoped

that this research shall provide a bridge to span the divide between material development and radiation effects testing of viable, militarily useful devices.

## II. Background

### ***Gallium Nitride (GaN) Applications and Testing***

Gallium Nitride (GaN), along with the related compounds Aluminum Nitride (AlN) and Aluminum Gallium Nitride (AlGaN) offer advantages and challenges in the production of novel semiconductor devices. GaN displays unique properties among the III-V compounds as well as difficulties both in doping and crystal growth.

GaN is of interest to the United States Air Force (USAF) and US Department of Defense (DoD) because of the promise of high-power, high-temperature, and high-frequency semiconductor applications [1],[2],[3] as well as for its unique optical uses in short wavelength diode lasers and light emitting diodes (LEDs) [4]. These unique areas of operational promise are quite likely to be employed in radiation exposure situations such as on-orbit communications hardware which is exposed to the space radiation environment, high-temperature devices for use in reactor monitoring and control, or high-power switches which may one day replace existing silicon-based switches in military and civilian power grids, bringing the necessity of radiation hardening against man-made sources or solar disruptions. GaN and its related compounds are already coming into widespread commercial use for many of these optical applications [7] and are beginning to be produced commercially for high-power density applications [8]. Given the radiation environments in which GaN-based devices will eventually be tasked to perform, it is prudent for radiation studies of the underlying materials to be undertaken at the

current stage of development to aid in the modeling and simulation of GaN based devices in these environments.

The study of energetic electron interactions in GaN will form a baseline from which future radiation effects studies may proceed. In addition to the emphasis on device performance in radiation environments, the radiation testing of GaN materials provides valuable insight into material defect formation processes and dynamics – insight that can be used to improve growth processes and produce better materials. Irradiation of semiconductor materials is a valued means of producing the same types of point defects in GaN [9] that material growth processes seek to minimize. Irradiation-induced defects can be used to study the dynamics and interactions of defects with band-gap states to include defect donors, acceptors, and trap states; compensation rates and complexation behavior of defects with band-gap states can be determined as well.

### ***Physical Properties of GaN***

GaN is a wide-bandgap semiconductor material with a 300K direct bandgap of 3.43 eV (361.2 nm) in the thermodynamically stable wurtzite crystalline phase. GaN is recognized as the most widely studied III-Nitride compound, but even at the current time, much research remains to be done on the properties of GaN. Some selected physical properties of wurtzite GaN are given in Table 1.

**Table 1. Selected Physical Properties of GaN**

Property (units)	Symbol	Value
Molecular weight (gm/mol) [10]	W	83.728
Density (gm/cm <sup>3</sup> ) [11]	$\rho$	6.15
Thermal Conductivity (W/cm·K) [10]	$\kappa$	1.3
Specific Heat (cal/mol·K) [10]	$C_p$	$9.1 + (2.15 \cdot 10^{-3} T)$
Static Dielectric Constant [12]	$\epsilon_p$	9.0
High Frequency Dielectric Constant [13]	$\epsilon_\infty$	5.35
Electron mobility, bulk (cm <sup>2</sup> /V·sec) [12]	$\mu_e$	1000
Hole mobility, bulk (cm <sup>2</sup> /V·sec) [12]	$\mu_H$	300
Debye Length @ 300K, $N_d=10^{18} \text{ cm}^{-3}$ (nm)	$\lambda_D$	3.586
Index of Refraction @ 1 $\mu\text{m}$ [10]	n	2.35
Electron affinity (eV) [14]	$\chi$	4.1

The bandgap of the wurtzite phase varies with temperature as given in the empirical Varshni equation

$$E_g(T) = E(0) - \frac{\alpha T^2}{(T + \beta)} \quad (1)$$

where, for bulk GaN,  $\alpha = -7.7 \cdot 10^{-4} \text{ eV/K}$  and  $\beta = 600 \text{ K}$  and  $E(0)$  is the fundamental bandgap energy. The most widely accepted value of  $E(0)$  is  $3.47 \text{ eV}$  [14]. The temperature dependant bandgap for the wurtzite phase of bulk GaN is shown in Figure 1 as generated by the analysis of Equation (1). In addition to its large bandgap energy, GaN is a direct bandgap semiconductor. Details of the 300K bandgap near the  $\Gamma$  symmetry point are shown in Figure 2, demonstrating the direct-bandgap nature of GaN materials.

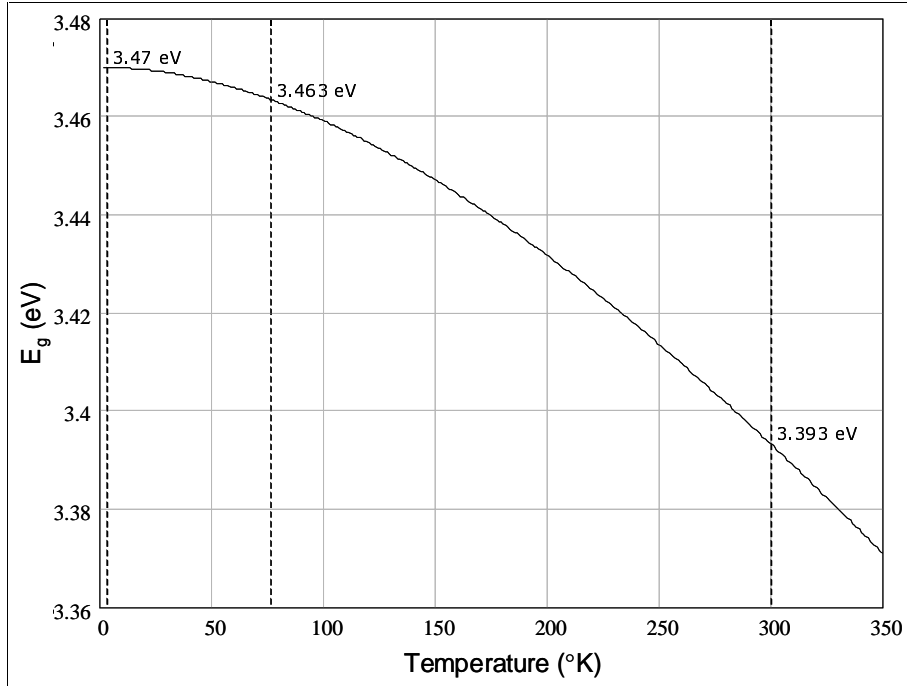


Figure 1. Estimated fundamental bandgap energy dependence upon temperature in wurtzite phase GaN. Dotted vertical lines represent liquid He, liquid N, and room temperature points. Data shown here was generated by equation 1.

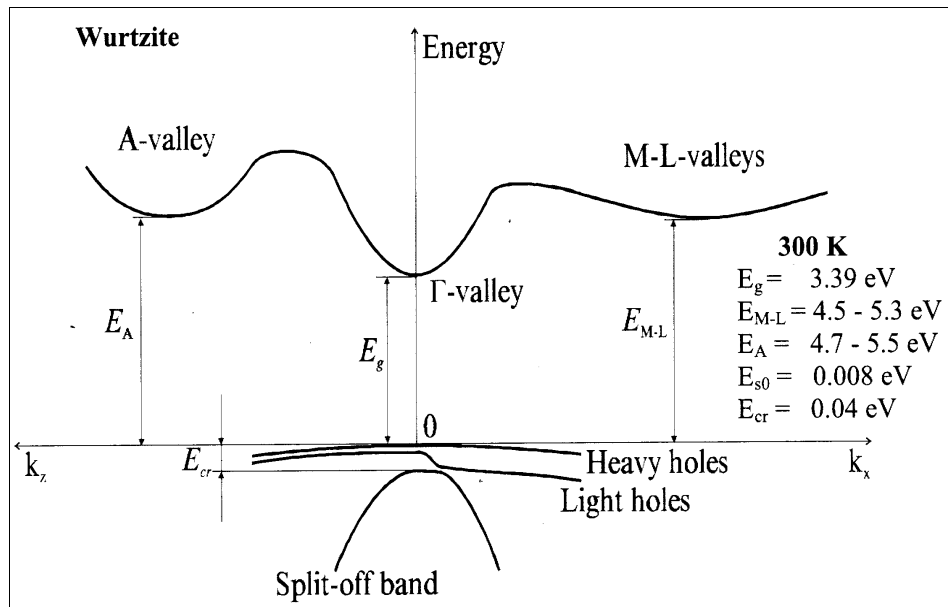


Figure 2. Wurtzite GaN band-structure as computed by Suzuki [15], et al via a plane-wave pseudopotential calculation method. All energy values are at 300°K.

A metastable zinc-blende phase also occurs with a 300K bandgap of approximately 3.2 eV (387.5 nm) [16]. Although the zinc-blende phase can be formed by epitaxial stabilization, the wurtzite crystalline structure is the dominant structure in device construction, and is the most thoroughly studied of the two forms. Models of the wurtzite structure in GaN are shown in Figure 3 for two views of interest. All further references to GaN refer to the wurtzite phase unless otherwise noted.

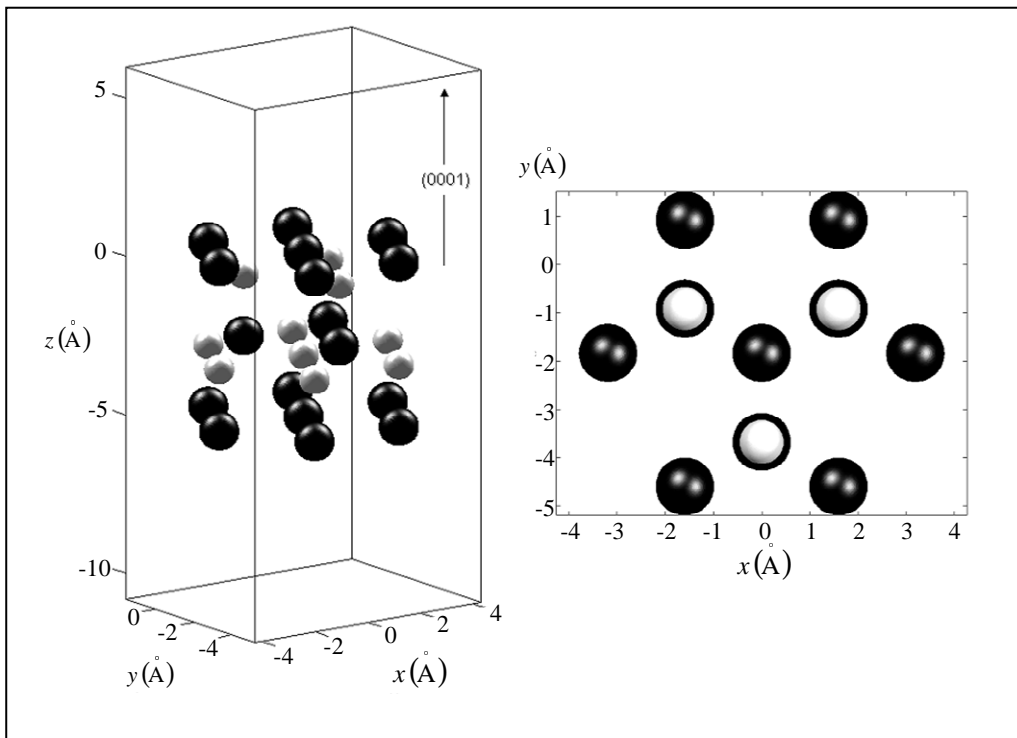


Figure 3. Calculated atomic locations for wurtzite crystal structure of GaN. The graph on the left illustrates the orientation of the  $(0001)$  direction, with Ga represented by black and N by white balls. Axis units are in angstroms. Plot on the right is presented looking down the  $(000\bar{1})$  direction for a Ga face surface.

Wurtzite GaN has lattice constants  $a = 3.189 \text{ \AA}$  and  $c = 5.185 \text{ \AA}$  with thermal coefficients given by  $\frac{\Delta a}{a} = 5.59 \cdot 10^{-6} K^{-1}$  and  $\frac{\Delta c}{c} = 3.17 \cdot 10^{-6} K^{-1}$  [10]. These values are important in evaluating the effects of various substrate materials on GaN film quality and device performance.

The value of the electron effective mass is commonly accepted to be  $0.22 \cdot m_0$  although the effective mass is not presently determined to great precision. Heavy hole masses are known to be greater than  $0.6 \cdot m_0$ , where  $m_0$  is the free-electron mass, but the value is not well characterized. A sizable number of studies have attempted to determine the ranges of effective mass both for electrons and holes, and are summarized for both theoretical and experimental studies in Table 2 below [17].

**Table 2 Electron and Hole Effective masses in GaN (derived from [17])**

Carrier type	Source (exp/calc)	Effective Mass ( $\times m_0$ )
$m_e^*$	Experimental	0.20 – 0.27
$m_e^*$	Calculated	0.18 – 0.22
$m_e^\perp$	Experimental	0.20 – 0.23
$m_e^\perp$	Calculated	0.18 – 0.23
$m_e^\parallel$	Experimental	0.20
$m_e^\parallel$	Calculated	0.17-0.20
$m_{HH}^*$	Experimental	1.0 – 2.2
$m_{HH}^\perp$	Experimental	0.75 – 0.9
$m_{HH}^\parallel$	Experimental	1.3
$m_v$ (DOS effective mass)	Calculated	1.5



GaN is typically strongly n-type, with the source of the shallow native donor being the subject of much contention. Early efforts seemed to point to a nitrogen vacancy ( $V_N$ ) [18] as the source, which was contested by initial theoretical results. The nature of the native donor in GaN is not firmly established at present, with arguments having been put forth for both a defect donor and for impurity doping. As recently as June of 2000, Van Nostrand [19] laid out many theoretical and experimental studies which illustrate the controversy; after first listing the sources supporting the “overwhelming evidence [that] the residual donor concentration in native GaN is due to N vacancies”, the “substantial body of works to the contrary” is presented. While it is still not conclusively resolved, the nitrogen vacancy (rather than impurities such as Si or O) is the leading candidate for the *n*-type auto-doping (or defect doping) in GaN, which can reach carrier concentrations of  $10^{19} \text{ cm}^{-3}$  at 300K [10]. High quality GaN crystals are now available with room temperature electron concentrations of  $5 \cdot 10^{16} \text{ cm}^{-3}$  [10].

Within the last year experimental evidence has pointed to impurity doping as the source of the *n*-type autodoping in GaN [20]; the impurity doping hypothesis is therefore gaining acceptance. There is still some controversy associated with this view.

Figure 4 shows the temperature dependence of the intrinsic carrier concentration in GaN [14]. Fitting the temperature dependence, as taken from the data of Figure 4, yields the relationship

$$n_i = 1 \cdot 10^{22} e^{-21.67 \left( \frac{1000}{T} \right)} \text{ cm}^{-3} \quad (2)$$

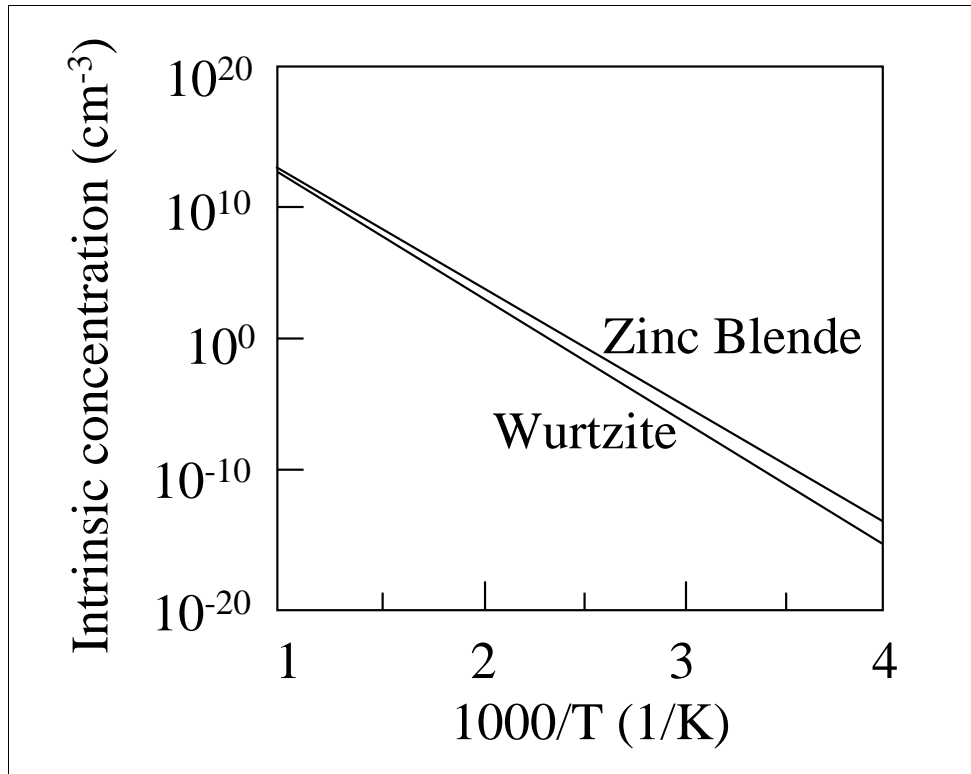


Figure 4. Temperature dependence of the intrinsic carrier concentration in GaN [14].

The *n*-type nature of undoped GaN has contributed to the well-noted difficulty in *p*-type doping of GaN. The large *n*-type conductivity tends to compensate acceptor dopants and results in highly resistive materials. Historically, the only acceptor that has been successfully used is Mg [21], when used in conjunction with electron beam irradiation or thermal annealing to convert the resistive compensated material to conductive *p*-type. The thermal annealing process has been observed to remove hydrogen, the primary compensating agent. These processes were observed to be of little utility in reducing the compensation of other group II elements, and to date no reliable process has been found to effectively acceptor dope GaN with any element besides Mg [10].

Even though Mg is the most prominent p type dopant in GaN, the acceptor level of Mg in GaN has been shown to be hundreds of meV above the valence band level – approximately 220 meV for optical determinations of ionization energy and varying with acceptor concentration from 125 meV to 180 meV for thermal ionization energies. These values, when extrapolated to a zero acceptor density, are consistent with the optical value of 220 meV to within the experimental uncertainty of  $\pm 20$  meV [22].

The large band-gap (3.49 eV) of GaN, which leads to a thermally insensitive semiconductor material, also leads to a large breakdown field. This large breakdown field strength, calculated to be greater than 3 MV/cm [23] and indicated by some sources to be greater than 5 MV/cm, makes GaN a good candidate for high power operation. These values are between five and eight times the values of Si and GaAs [12]. Measured values of the breakdown field and voltage for GaN are shown in Figure 5 as a function of sample temperature.

GaN also has large carrier velocities, which enable high speed and high frequency operation for switching and RF devices. GaN has exhibited peak electron velocities of  $3.0 \cdot 10^7$  cm/sec and saturation velocities of  $1.5 \cdot 10^7$  cm/sec [12].

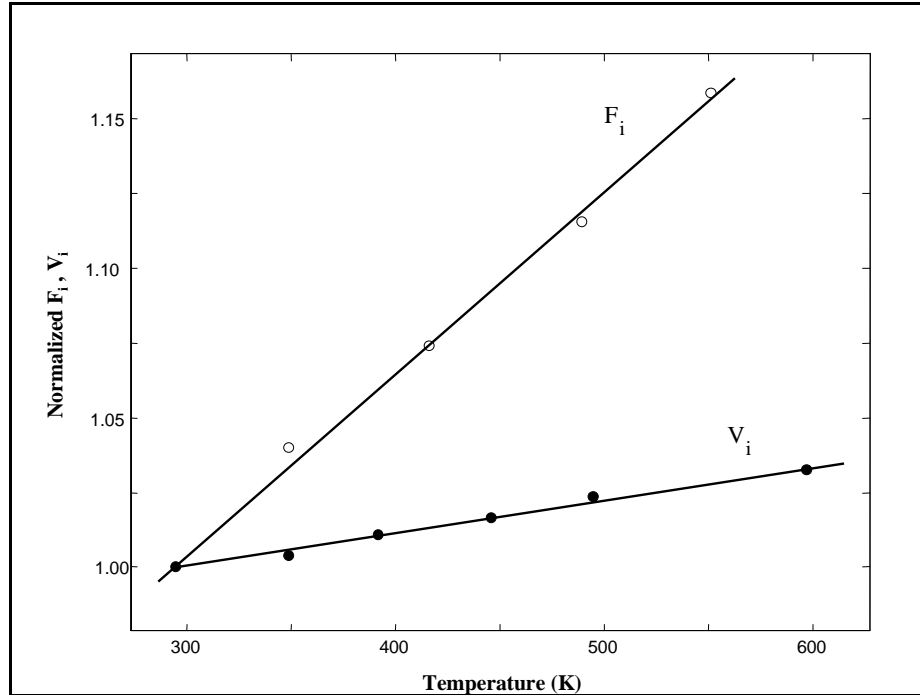


Figure 5. Normalized breakdown field ( $F_i$ ) and voltage ( $V_i$ ) in GaN samples. Normalization is to  $1\text{-}2 \cdot 10^6$  V/cm and 42 V respectively. Samples are  $p^+$ -p-n diodes. [14]

GaN, like all of the III-Nitrides, is highly piezoelectric and is highly polarized, by semiconductor standards. The piezoelectric and spontaneous (zero field) polarization of GaN is ten times that of conventional compound semiconductors. The field due to spontaneous polarization of III-Nitrides can reach 3.0 MV/cm and for AlGaIn/GaN heterostructures the piezoelectric field may reach 2.0 MV/cm [24].

One of the biggest challenges in the use of GaN for electronic devices has been the development of suitable substrates for GaN device growth. GaN has proven very difficult to produce in a large crystal formats, primarily due to a low solubility of  $N_2$  in Ga, and is still not commercially available. SiC and  $Al_2O_3$  (sapphire) are the substrate materials of choice today for GaN devices, although each has associated difficulties. AlN substrates may soon solve some of these difficulties with lattice mismatch and thermal

conductivity issues and become commercially available. Fifteen millimeter (mm) substrates are commercially available, and substrates up to 50 mm are projected to be available soon [25]. Thick (over 200  $\mu\text{m}$ ) free-standing GaN films with low defect densities have been produced by HVPE growth and subsequent removal of sapphire substrate material. These films have low defect densities due to the removal of the substrate interface region and hold promise for production of large GaN wafers [26]

Sapphire substrate materials offer the advantages of widespread availability, low cost, hexagonal crystal symmetry, and ease of handling. Due to the low solubility of  $\text{N}_2$  in Ga and high vapor pressure of  $\text{N}_2$  over Ga, extremely high temperatures and pressures (in excess of  $1200^\circ$  and 12 kbar) are required for HVPE and MOVPE GaN growth – making the high temperature stability of sapphire an important factor [10].

Sapphire substrate issues are primarily centered around the lattice mismatch ( $\approx 16\%$  on the (0001) plane) [10], which induces large dislocation defect densities near the interface, and the extremely low thermal conductivity of sapphire ( $0.42 \text{ W/cm}\cdot^\circ\text{K}$ ), which is untenable for the high-power devices that GaN is suited for. It is possible to compensate for the interface defect density by growing a thin GaN buffer layer before the device layers are grown. This process tends to isolate the defects from the active device region, but adds an additional processing step to the growth process, increasing time and cost to produce devices. The difficulty with the low thermal conductivity of sapphire is not easily solved; as a result, most high power devices where thermal energy dissipation is an issue are grown on SiC substrates to take advantage of its high thermal conductivity.

Factors that SiC has in its favor as a GaN substrate include a smaller lattice mismatch than sapphire ( $> 3.5\%$ ) and good binding qualities to GaN epilayers [27], much

better thermal conductivity, and easier formation of facets than in sapphire. However; SiC is much more expensive to produce than sapphire substrates and there are issues associated with differing crystal symmetries (which produce structural defects in the GaN epilayer), as well as surface preparation difficulties that must be considered [10]. SiC is the substrate of choice for high-power applications due primarily to its ability to conduct thermal energy away from the device.

### ***GaN Growth Methods***

A variety of growth methods and techniques are used to produce epitaxial GaN layers on the substrates mentioned previously. Short descriptions of the methods used to produce the materials in this dissertation are provided below.

### **Molecular Beam Epitaxy (MBE)**

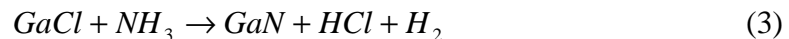
Much of the material studied in this dissertation was produced via MBE, a growth method used to produce thin layers of GaN on a prepared substrate material via atomic deposition in ultra-high vacuum (UHV) conditions. The primary limiting factor inherent in this technology is the relatively low growth rate. Growth rates are limited indirectly by the requirement to produce atomic N; cracking of the N<sub>2</sub> precursor into atomic nitrogen is a high energy process requiring formation of a plasma to extract atomic N. The requirement to dissociate the N<sub>2</sub> precursor limits the use of conventional effusion cell MBE systems and drives the GaN production process to an RF or Electron Cyclotron Resonance (ECR) microwave plasma source for the N cell [28]. The resulting trade-off is between the growth rate, which demands higher plasma excitation powers, and ion-

beam damage, which is limited by lower excitation power. If higher temperatures are used (700° C and above) an ammonia source can be used as the N<sub>2</sub> precursor, limiting ion beam damage [29]; however, this introduces defects due to thermal cycling.

Primary advantages of MBE epitaxial growth are the relatively low growth temperature and the low impurity content (particularly with respect to H impurities) due to the UHV deposition [30]. Low growth temperatures lead to lower thermal stresses and thus to lower levels of gross defects than occur with high temperature growth processes. The UHV deposition process limits the amount of impurities in the material, particularly with respect to oxygen and hydrogen at the cost of introducing lattice defects due to ion beam damage.

### **Hydride Vapor Phase Epitaxy (HVPE)**

HVPE is was one of the first growth methods used to prepare GaN epitaxial layers and is today a leading contender for the growth of large diameter, thick, high quality GaN layers [30]. HVPE is conducted in a hydrogen environment at temperatures near 1000C, where the precursor compounds, typically NH<sub>3</sub> and GaCl (produced by flowing HCl over metallic gallium), react via the following equation



and are deposited on the substrate material. The hydrogen-rich environment leads to incorporation of H impurities into the material.

HVPE material is characterized by low defect densities and correspondingly good material properties. GaN material grown by HVPE and dissociated from the underlying substrate is currently the world's highest mobility GaN [20]. Dissociation from the

underlying substrate layer insures that conductive interface layers are not formed, and the high-quality, relatively defect free bulk material is retained. Free-standing GaN layers over 200  $\mu\text{m}$  in thickness can be produced by this means, with carrier concentrations in the mid to high  $10^{16}$  range, and have been used in this study.

## **Metal-Organic Vapor Phase Epitaxy (MOVPE)**

MOVPE is a method of epitaxial growth using metal alkyls (such as trimethylgallium,  $\text{Ga}(\text{CH}_3)_3$ ) as group III precursors and ammonia as a nitrogen precursor for a high-temperature, vapor phase deposition of GaN. MOVPE was used extensively early in the production of the III-nitrides and is still the prevalent method of commercial production [31].

MOVPE GaN deposition using trimethylgallium and ammonia as precursors proceeds by a complicated set of reactions, based on the intermediary formation of acid-base pairs [31]. The complex chemical nature of this growth process, which is still not completely understood, is a source of defect formation in MOVPE GaN layers since the adduct pairs created may be deposited in the material intact. Other defect sources inherent in this growth method include the formation of nitrogen vacancies due to the high temperatures required to dissociate the ammonia precursor, and the inclusion of carbon and methyl molecules into the lattice [32].

MOVPE grown materials, while not used in this dissertation, were analyzed by Carlos using EPR [33]. Measurements in MOVPE GaN were shown to be very similar to those made in HVPE GaN.



## ***Radiation Interactions***

The expected effects of ionizing radiation on solid state materials such as GaN are two-fold: dose rate dependent ionization effects and total dose dependent persistent effects. In the case of energetic electron bombardment both effects are produced; however, we are concerned primarily in this study with the persistent effects of the radiation interaction and will not consider dose-rate dependent transient effects (mainly photo-ionization).

The primary mechanism for introduction of persistent radiation effects is the displacement of lattice atoms (Ga or N) through elastic collisions with energetic particles. Binding energies of the lattice constituents vary with the particular sublattice considered and are anisotropic in nature [34]. The rates of displacement damage for Ga and N sublattices are a function of both atomic binding energy and collisional energy transfer. In general, Ga atoms are bound less tightly than the N atoms in GaN; however, the energy deposited through an elastic collisional process is heavily dependent on the lattice atom's mass and so much more energy can be imparted to the less massive nitrogen atoms. Over the ranges of energy considered in this study (0.5-1.5 MeV) both types of damage are expected to occur simultaneously.

Displacement energies for the lattice constituents in GaN have been calculated by Nord [35]. The minimum displacement energies are  $22 \pm 1 eV$  for gallium and  $25 \pm 1 eV$  for nitrogen, where the minimum is taken over all angles. For an average over all possible angles, the displacement energies are  $45 \pm 1 eV$  for gallium and  $109 \pm 2 eV$  for

nitrogen. The maximum energy that may be imparted to a lattice atom by an energetic electron via coulomb scattering is given by

$$E_{trans}^{max} = 2 \frac{(E_{e^-} + 2m_{e^-}c^2)}{m_{atom}c^2} E_{e^-} \quad (4)$$

so that the maximum energy available to a lattice atom via an interaction with a 1 MeV electron is 62 eV for gallium atoms and 309 eV for nitrogen atoms. The maximum energy transfer as a function of the incident particle energy is shown in Figure 6 for both gallium and nitrogen. Calculations of equation 4 shown in Figure 6 indicate that not only can one expect point defects on the nitrogen sublattice at incident electron energies above 0.3 MeV, but that gallium sublattice point defects should appear at incident electron energies around 0.5 MeV. Thus, point defects on both sublattices are expected for electron irradiation at 1.0 MeV. The possibility of knock-on damage exists, although large damage cascades are not expected from the knock-on particles, which are limited to about 290 eV of kinetic energy for nitrogen atoms and 41 eV for gallium atoms. This follows from Nord's calculations of secondary defect production which show that for recoil energies of 200 eV, less than one additional point defect in either sublattice (per recoil atom) is expected from either species of recoil atom [35].

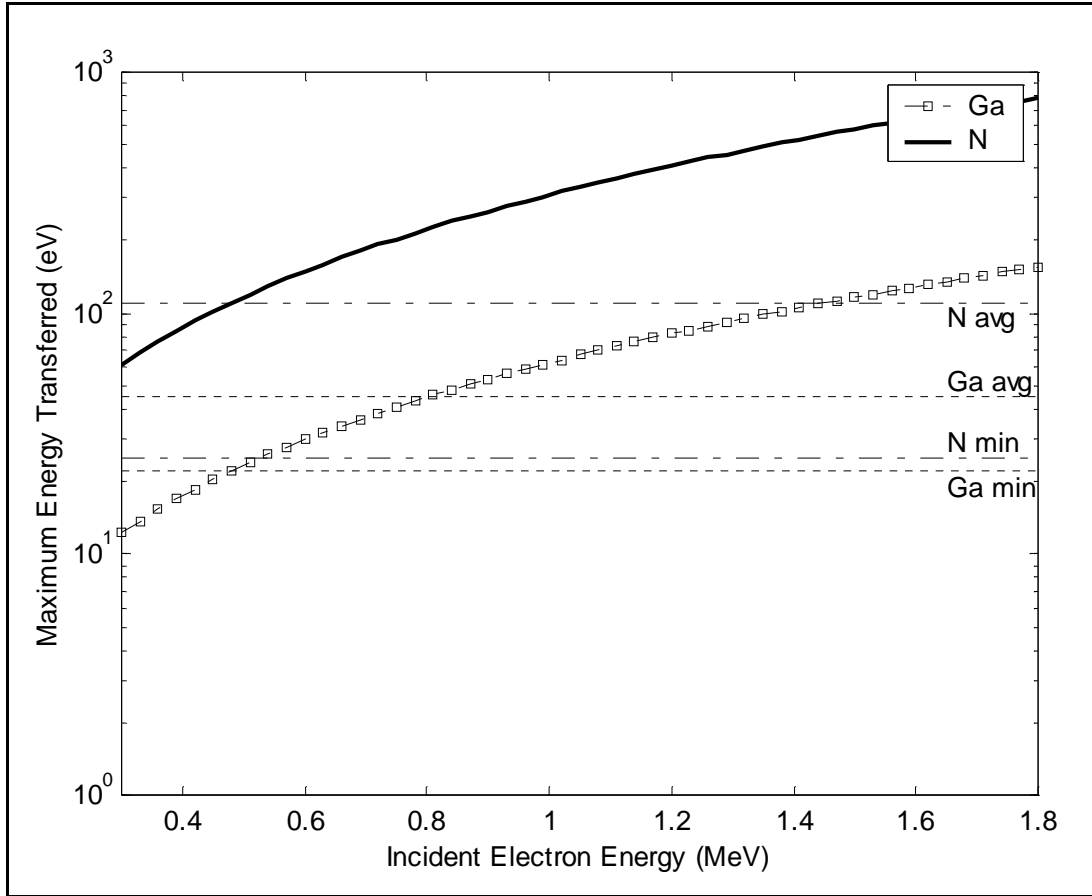


Figure 6. Maximum energy transfer for gallium and nitrogen as a function of the incident electron energy. The average and minimum displacement energies for both gallium and nitrogen are shown as horizontal lines. Values are calculated via Equation 4.

This evaluation is reinforced by the reported observation of dislocation damage in GaN following electron irradiation at approximately 300-350 keV irradiation energies [36].

The types of radiation-induced point defects produced will primarily be nitrogen vacancies ( $V_N$ ), nitrogen interstitials ( $I_N$ ), and the corresponding gallium sublattice point defects  $V_{Ga}$  and  $I_{Ga}$ . These point defects are expected to be mobile in the lattice for all but the lowest temperatures [37], leading to the potential formation of a variety of complexes with impurities in the lattice or with other defects.

Introduction rates of electron irradiation induced defects in GaN are not well characterized due to the inherent difficulty in separating the effects of different types of sublattice damage and the compensating effects of the various defects. While the exact classification of defect types in GaN is uncertain, many defects (both shallow and deep states) have been experimentally observed by Hall effect measurements, DLTS, PL, and various magnetic resonance techniques, including radiation induced states. The activation energies and identity of these states are catalogued graphically in Figure 7. While many of the states depicted are identified with a particular impurity or defect type, one should bear in mind the tentative nature of many such identifications and the controversy which surrounds some of these assignments.



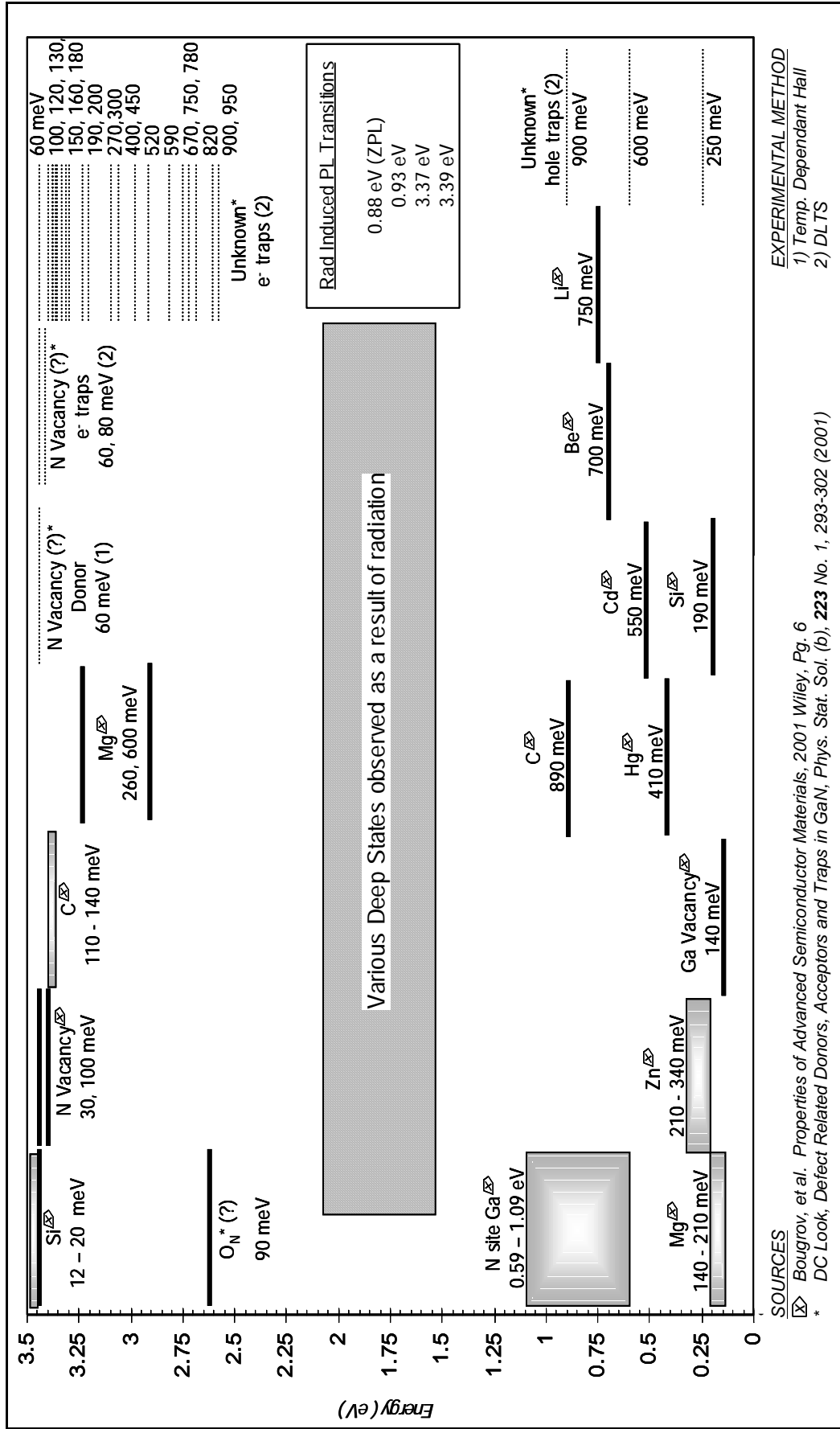


Figure 7. Band Gap states of GaN, with as-grown states depicted by solid lines and radiation induced effects by dotted lines. [38] [13]

## ***Electron Paramagnetic Resonance (EPR) Spectroscopy***

Basic elements of EPR spectroscopy will be discussed in this section, while elements of EPR theory appropriate to the analysis of measurements in this dissertation will be discussed in the EPR Theoretical Considerations section. Elements of EPR theory introduced in this section will present a meaningful introduction to the physics of the technique and provide a background for the theoretical methods presented later.

EPR spectroscopy is a powerful experimental technique allowing direct observation of unpaired electron spins, including unpaired spins associated with a defect or impurity site in a solid state material via microwave absorption. In some instances, identification of the host site or atom is available via interpretation spectral features created by the spin coupling with the host nucleus; however, this is not guaranteed. Electron Spin Resonance (ESR) and Electron Paramagnetic Resonance (EPR) are generally accepted as synonymous terms; EPR will be used in the balance of this work since it succinctly captures the essence of the technique.

Since the recording of the first EPR spectrum, by Zavoisky in 1945, studies of impurities in solid-state crystal structures have been an important part of this experimental field. The early development of EPR techniques was performed primarily at Clarendon Laboratory in Oxford, where the primary application was the study of metal ions in crystalline lattices [39]. Abragam was similarly engaged in crystalline studies when he pioneered the analysis of hyperfine spectra, particularly with regard to analysis of large hyperfine coupling constant materials [40]. Indeed, by 1967 Bleaney would write that,

“Electron Paramagnetic Resonance has developed primarily into a tool for investigation of effects in the solid state, in which additional information is provided by hyperfine structure; for example the latter can identify the nucleus (or nuclei) with which magnetic electrons interact, and give the strength of the interaction” [41]

Since Bleaney’s writing, EPR has become an important tool in molecular chemistry where it is used as a sensitive probe of the bond structures and bonding electron states; it remains a powerful tool for investigation of the solid state.

Today, EPR spectroscopy remains a valued tool for defect studies in crystalline materials, along with methods that have been derived from traditional EPR. Derivative methods of EPR include: Optically Detected Magnetic Resonance (ODMR), a method that obtains increased sensitivity but must depend upon photonic transitions between states [42]; Electronic Nuclear Double Resonance (ENDOR), a method that stimulates both electronic and nuclear resonances [43]; and Electrically Detected Magnetic Resonance (EDMR), a method using electrical measurements to enhance detection sensitivity [44]. Many of these methods trade increased signal sensitivity for the inclusion of secondary processes, such as photonic transitions or nuclear magnetic resonances, that can convolute the analysis of the resulting data. Many good references are available on EPR spectroscopy and related methods, including Atherton [39], Weil [45] and Poole [46].

At its most basic level, EPR spectrometry is based on measuring the transition energies and probabilities of photon induced transitions between Zeeman levels of a



charged particle in a magnetic field ( $\vec{B}$ ). Zeeman splitting for an electron in a magnetic field of magnitude  $|\vec{B}|$  is described by the expression

$$\Delta E = \pm \mu_B g_e |\vec{B}| \quad (5)$$

where the Bohr magneton is given by

$$\mu_B = \frac{e\hbar}{2m_e} \quad (6)$$

and  $g_e = 2.00233$  is the measured gyromagnetic ratio of the free electron. The g-value is a scaling factor that describes the magnitude of the energy splitting of a charged particle in a magnetic field. A naïve classical electromagnetic model of a free electron as a spinning charged sphere interacting with an external field predicts energy levels of

$$\Delta E = \pm \mu_B |\vec{B}| \quad (7)$$

Therefore, when experiments determined the scaling factor between  $\Delta E$  and  $|\vec{B}|$  to be  $2.0023 \cdot \mu_B$ , the value  $2\mu_B$  was referred to as the “anomalous electron magnetic moment” of the electron [39], a term which has fallen out of use. The g-value can thus be thought of as the scale of the departure from the classically expected magnetic moment values of a magnetic particle.

The term “electron paramagnetic resonance” arises from the requirement for the electron to be in an unpaired, or paramagnetic, spin state in order to carry out spectroscopy. For electrons in diamagnetic (paired) states, all quantum numbers are identical with the exception of the spin quantum number  $m_s$ , which takes on values of  $+1/2$  and  $-1/2$  for the paired electrons. In the diamagnetic state, photon absorption is

prohibited by the exclusion principle; thought of in another way, absorption and emission at the excitation frequency would be exactly balanced, making spectroscopy impossible.

In a real system such as transition metals in crystalline structures, organic radicles, or donor bound electrons, the  $g$ -value can and does vary from the free-electron  $g$ -value. These variations in the  $g$ -value are attributed to the admixture of the orbital angular momentum with the spin angular momentum [47] (even though the application of the external field quenches the orbital angular momentum of the ground state due to arguments stemming from the non-degenerate nature of the states [48]). Non-spherical symmetry is often associated with this admixture, producing anisotropy in the  $g$ -value, which is therefore properly termed the  $g$ -tensor, with respect to the orientation of the applied magnetic field. In crystalline systems,  $g$  value anisotropy is typically present, with the relationship between angle  $\theta$  and  $g$ -value given by [33]

$$g(\theta) = (g_{\perp}^2 \cdot \sin^2(\theta) + g_{\parallel}^2 \cdot \cos^2(\theta)) \quad (8)$$

for the case of two dimensional anisotropy (for a more general treatment in three dimensions, see [46]). Here the parallel and perpendicular subscripts indicate the angle of the semiconductor  $c$  axis with the applied magnetic field.

Calculation of the  $g$ -value from the experimental data is performed by comparing the measured Zeeman transition energy (derived from the microwave frequency via  $\Delta E = h\nu_{\mu w}$ ) and the measured magnetic field strength  $|\vec{B}|$  at the microwave absorption peak. Given the experimentally determined values of  $\nu_{\mu w}$  and  $B_{res}$  (the resonant magnetic field strength), the gyromagnetic ratio is calculated by

$$g = \frac{h\nu_{\mu w}}{\mu |\bar{B}|} \quad (9)$$

This g-value is unique to the species and site depending upon binding status and surroundings. According to equation 9, the g-value of a site may also be expressed in terms of the resonant magnetic field value and this is used extensively in laboratory practice. In certain instances, coupling of the electron and nuclear spins associated with the site lead to a splitting of the Zeeman energy levels into “hyperfine” levels. The magnitude of this splitting is dependent upon the magnetic properties of the nucleus, allowing the identification of the nuclear species involved in the coupling. When instrument sensitivity and resolution are sufficient, additional splittings due to coupling with surrounding (nearest neighbors) nuclei may be resolved as well.

As described above, coupling of the electron spin ( $\bar{S}$ ) with a nuclear spin or spins ( $\bar{I}$ ) leads to a splitting of the Zeeman levels into  $(2I + 1)$  levels. To first order the splitting is described by the hyperfine coupling constant ( $A$ ) and the nuclear spin of the interacting nuclei, with energy levels given by

$$\Delta E = \mu_B g |B| + \frac{1}{2} A m_I \quad (10)$$

where the  $m_I = (-I, -I + 1, \dots, I)$ , producing the  $(2I + 1)$  equally spaced equal magnitude lines in the resulting spectrum. For traditional EPR measurements, where nuclear spin modes are not excited, the allowed transitions measured are determined by the selection rules  $\Delta m_S = \pm 1, \Delta m_I = 0$ . This simple view of the effects of hyperfine coupling is insufficient to explain all spectral features and must be modified; however, it serves to

communicate the basic nature of the hyperfine interaction. Further developments will be left until the section on EPR Theoretical Considerations in the theory section, in which derivations appropriate to the cases in this dissertation will be provided.

Since the sites under study are not truly isolated spin states or systems of states, interactions with the surroundings (termed the *lattice*) are important in EPR spectroscopy, and enter into our consideration primarily through the process of *spin-lattice relaxation*. The process of microwave absorption disturbs the thermodynamic equilibrium concentrations of the electrons under study and relaxation to the equilibrium levels proceeds through the exchange of energy with the surrounding lattice. This relaxation is characterized by a lattice relaxation time constant ( $\tau$ ). This relaxation time is related to the linewidth (or the uncertainty in the energy of the transition) by the uncertainty relationship

$$\Delta E \Delta t \geq \hbar \text{ or } \tau \Delta \omega \geq 1 \quad (11)$$

which asserts that as the lifetime ( $\tau$ ) becomes short, to the point of equaling the inverse of the microwave frequency, linewidths can become so large as to make the signal unmeasurable [49]. For this reason, EPR measurements on solid state materials are typically made at cryogenic temperatures ( $< 20K$ ) to limit the phonon-mediated interactions of the spin states with the crystalline lattice [50]. A benefit of conducting measurements at these temperatures is the enhanced population difference between the upper and lower states. The EPR signal is proportional to the population imbalance, and is given by

$$Y_{Diff} = Y_0 \cdot \left[ \frac{n_1 - n_2}{n_1 + n_2} \right] = Y_0 \cdot \left[ \frac{1 - e^{-\hbar\omega/kT}}{1 + e^{-\hbar\omega/kT}} \right] \quad (12)$$

where  $Y_0$  is the signal as the temperature approaches 0 °K. For X band (10 GHz) cavities, and  $g$  values near 2.0, the population of the lower levels is greatly enhanced at cryogenic temperatures. In this range the sensitivity is not a strong function of temperature, as  $\hbar\omega \gg kT$  and the signal strength approaches the constant value  $Y_0$ .

EPR spectroscopy systems are tasked with measuring a relatively low intensity signal against a noisy background, prompting the use of magnetic field modulation and a lock-in amplifier system to increase signal to noise ratios. The magnetic field strength is varied in X-band EPR systems and the microwave frequency held constant due to difficulty in designing variable frequency microwave sources and cavities. The signal resulting from this magnetic field modulation is the derivative of the absorption profile and must be integrated to obtain the absorption behavior. Given this magnetic field sweeping and the magnetic field modulation, the evolution of the first derivative absorption signal becomes clear. This is illustrated in Figure 8, borrowed from [46]. Note that in Figure 8, the independent variable is the magnetic field intensity  $\mathbf{H}$  rather than the magnetic flux density  $\mathbf{B}$  that has been used to this point; the two values are simply related by the magnetic permeability via  $\vec{B} = \mu\vec{H}$ .

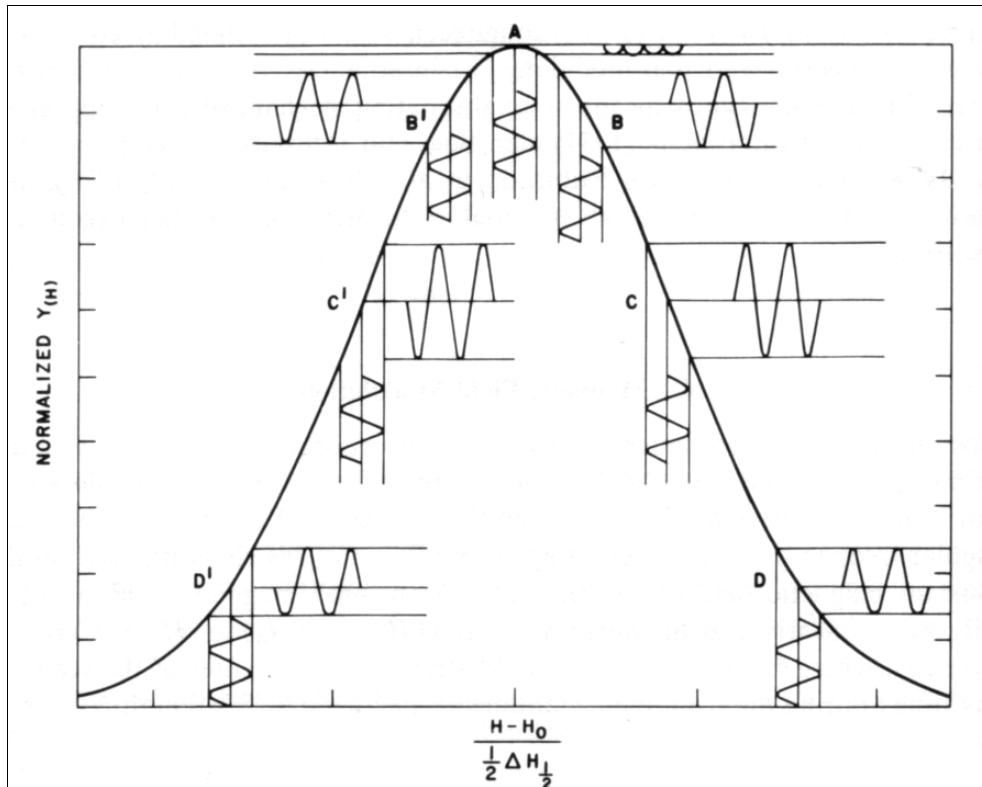


Figure 8. Relationship between magnetic field modulation (vertical waveform), absorption spectrum ( $Y(x)$ ), and resultant signal (horizontal waveform). [46]

## Applicability of EPR Spectroscopy to Radiation Effects Studies

EPR spectroscopy is distinguished from many of the derivative methods (such as ODMR, EDMR, etc.) by the direct observation of paramagnetic states without the requirement for corresponding transitions to/from other discrete energy levels in the material. This fact simplifies the analysis of EPR data with respect to relative changes in the population of the sites under investigation; the signal observed is not influenced by changes in the population states of other energy levels, an important distinction to remember when comparing EPR and Hall effect data. The direct measurement of a particular site's (such as the unionized shallow donors) population makes the application

of the EPR method to radiation studies attractive because of the inherent ability to determine relative changes in the pre-irradiation and post-irradiation site populations.

Although ODMR or PL-ODMR both can offer enhanced signal sensitivity, they suffer from the inter-dependence of different states to produce the observed resonance. Resonance signals in these methods must meet the resonance requirements in the applied magnetic field and must meet resonance requirements for the optical transitions between inter-bandgap energy transitions. While the ability to selectively excite these optical transitions allows greater sensitivity, at least two states (and often more) are involved in the transition process, with all of the participating states conceivably exhibiting spin dependent excitation properties. Unfortunately, the population statistics of any of these states may prove a transition rate-limiting factor, making determination of the actual population of the state of interest impossible.

## **EPR Measurements in GaN**

GaN has been studied via EPR and ODMR spectroscopy since the early 1990's, due primarily to interest in the nature of the native defects which plagued early growth efforts. For effective mass (hydrogenic) donors in GaN the g-value is typically near 1.95 ( $1.93 \leq g \leq 1.96$ ) and is anisotropic. Gyromagnetic ratios of effective mass donors are slightly anisotropic with respect to magnetic field direction, with values of  $g_{\perp} = 1.9485 \pm 0.0002$  and  $g_{\parallel} = 1.9515 \pm 0.0002$  as determined by several studies [51]. Several other signals, characteristic of various defects or impurities, have also been detected via EPR and ODMR, and are shown in Table 3. GaN grown on sapphire substrates also displays strong signals from substrate transition metals, and these are

differentiated by their strong angular dependencies and saturation at low microwave powers [33]. It is important to note that effective g-value of hydrogenic donors in GaN is dominated by the conduction band structure; therefore, any effective mass donor should exhibit behavior similar to the anisotropic 1.95 g-value of the shallow native donor in GaN reported by Carlos [33].

**Table 3. Observed EPR Signals in GaN**

$g_{\parallel}$	$g_{\perp}$	<i>Linewidth</i> ( $\Delta B$ Gauss)	<i>Ascribed Nature / Source</i>
$1.9515 \pm 0.0002$	$1.9485 \pm 0.0002$	22-170	EM Donor [51]
$1.989 \pm 0.001$	$1.992 \pm 0.001$	130	Deep Donor [51]
$2.004 \pm 0.001$	$2.008 \pm 0.001$	*	Ga <sub>i</sub> [52]
$1.960 \pm 0.002$	$\approx 2.03$	*	Unknown [52]
1.989	1.992	*	Unknown [52]
$2.08 \pm 0.01$	$2.00 \pm 0.01$	260	Mg [51]

\* Reported after 2.5 MeV electron irradiation, via ODMR.

Hyperfine splitting in GaN has been observed via ODMR in GaN [52]. Hyperfine splitting in GaN is expected to occur predominantly with the primary lattice constituents exhibiting non-zero nuclear spin. In the case of GaN, both of the primary lattice constituents have non-zero nuclear spins, and both have two naturally occurring isotopes. The isotropic hyperfine coupling constants, nuclear spin values, nuclear g-values, and isotopic abundances are shown in Table 4 for each of the isotopic species occurring in the GaN lattice.



**Table 4. EPR Hyperfine Parameters for Ga and N [53]**

<i>Nuclide</i>	<i>Nuclear Spin</i>	<i>Natural Abundance</i>	<i>Isotropic Hyperfine Splitting Constant (mT)</i>	<i>Nuclear g-value</i>
<sup>14</sup> N	1	99.63%	64.62	0.4038
<sup>15</sup> N	1/2	0.366%	-90.65	-.5664
<sup>69</sup> Ga	3/2	60.1%	435.68	1.3444
<sup>71</sup> Ga	3/2	39.9%	553.58	1.7082

Simple, first order approximations to the hyperfine splitting ( $\frac{1}{2} A m_l$ ) are insufficient to predict the resonance positions ( $B_{res}$ ) when the hyperfine coupling constant becomes large with respect to the Zeeman splitting. Wiel gives a rule of thumb for comparing these magnitudes at microwave frequencies near 10 GHz as [54]

$$A_0 / g_e \mu_e \geq 10 mT . \quad (13)$$

where  $A_0 / g_e \mu_e$  is the hyperfine coupling constant expressed in magnetic field units.

Since the measured values of the isotropic hyperfine splitting constants for both gallium isotopes are in the 450-500 mT range and is approximately 64 mT for the predominant isotope of nitrogen, it is immediately obvious that a more sophisticated approach to computing hyperfine splittings will be necessary. This approach will be outlined in the Theoretical Considerations section.

### **Hall Effect Measurements**

In addition to EPR measurements, temperature dependent Hall effect measurements of samples were performed to determine carrier density and mobility of samples before and after irradiation. Hall measurements are used to determine the energy levels and concentrations of donor and acceptor populations before and after irradiation.

The most powerful use of Hall effect measurements in this study occurs when the data is linked with the EPR measurements to determine the relative contributions of the EPR active centers to carrier concentration. The history and theory of Hall effect measurements are widely available [55] and will not be repeated here except as is necessary for the current analysis.

Carrier concentration measurements in this study are made more difficult by the existence of a degenerate, conductive channel at the sapphire/GaN interface, a result of the high defect density found at this interface [56]. After analyzing the impact of this conductive channel and isolating the behavior of the GaN epilayers as outlined in the theory section, estimates of the GaN carrier concentration are possible. Donor and acceptor concentrations in a sample can be determined by fitting a donor activation model to the carrier concentration data. The resulting donor concentrations, when compared with the relative concentration changes in EPR active sites, may substantiate the EPR data and allow an estimate of the relative contribution of the EPR site to the carrier concentrations.

The most important distinction between the concentrations measured via the Hall effect and the EPR measured concentrations is in the source of the concentration data: the Hall effect measures the carrier density and mobility whereas the EPR process measures the concentration of the donor or acceptor sites themselves, as identified by a unique g-value. Donor and acceptor concentrations must be extracted from Hall effect data by modeling, while they may be directly measured by EPR if paramagnetic. Thus, the combination of these two experimental methods allows a complete analysis of both donor and acceptor populations and the conduction band electron concentration derived

from these sites. When these data are combined, there is much less ambiguity regarding the nature of the changes in carrier concentrations and the changing donor site populations may be correlated with the changes observed in the conduction band populations.

### **III. Theoretical Considerations**

Theoretical discussion in this section are limited to development of theoretical models found to be useful for analysis of the experimental data collected during the research. The development of a mathematical model to explain the observed changes in shallow donor concentrations following irradiation is presented first. Development of the spin Hamiltonian and the hyperfine coupling analysis of a spin  $3/2$  nucleus and a single electron is then presented. Both of these topics prove to be useful in later analysis.

#### ***EPR Theoretical Considerations***

##### **Donor Passivation Models**

EPR measurements measure absorption due to spin state transitions of unpaired electrons. Since EPR measurements in solid-state materials are typically made at temperatures below 10K, almost all EPR active impurity donors, such as silicon or oxygen in GaN, will be in their un-ionized state, and the EPR signal can safely be assumed to arise from the excitation of the loosely bound donor electrons. Ionization of these shallow donors thus promotes the donor bound, unpaired electrons to the conduction band, rendering the resulting positively charged donor site diamagnetic and un-measurable by EPR. Any process which isolates these donors in the positively charged state at low temperatures or which involves the unpaired electron in a bonding arrangement will render the site insensitive to EPR absorption.

Particle balance considerations dictate that the number of ionized donors is given by

$$n_D^{tot} = n_D^0 + n_D^+ \quad (14)$$

where  $n_D^{tot}$  is the total number of shallow donors,  $n_D^0$  is the number of neutral donor atoms at low temperature, and  $n_D^+$  is the number of ionized donors. The doubly ionized donor state is not considered as a possibility at the temperatures of interest. Donor sites in the material can be compensated by acceptors or electron traps, occurring during the growth process or as a result of irradiation respectively; while  $n_D^+$  typically goes to zero at low temperatures, the inclusion of acceptor sites or electron traps may increase their concentration by reducing conduction band electron populations to the point that electrons are not available to fill the ionized donor sites. This effectively results in the pinning of the Fermi level near the donor level to account for the increased population of ionized donors at a particular temperature [57].

From charge balance considerations the carrier, donor and acceptor concentrations may be expressed as

$$n + \sum_k N_{Ak}^- = p + \sum_j N_{Dj}^+ \approx \sum_j N_{Dj}^+ \quad (15)$$

where  $k$  and  $j$  are summed over the acceptor sites with  $\epsilon_{Ak} < \epsilon_f$  and donor sites with  $\epsilon_{Dj} \geq \epsilon_f$  respectively,  $n$  represents the total conduction band electron concentration and  $p$  is the hole concentration. Again the  $N_{Ak}^-$  and  $N_{Dj}^+$  represent the ionized acceptor and donor concentrations respectively. As the temperature drops towards 0K, the expression above reduces to

$$n_D^+ - N_A^- = 0 \quad (16)$$

where  $N_A^-$  is the concentration of acceptor sites (summation over  $k$  levels in equation 15) occupied by an electron and assuming a single donor level is at or above the Fermi level. At low temperatures, we may assume that all of the acceptors are in the “occupied” state, at least to the point where there is a higher acceptor concentration than there are donor electrons. When equations (14) and (16) are combined and solved for the un-ionized donor concentration the result is

$$n_D^0 = n_D - n_D^+ = n_D - N_A^- \quad (17)$$

so that the EPR measured quantity is the uncompensated donor concentration, as is expected. This result suggests that two types of processes can change the measured EPR signal: processes which remove or change the substitutional donor sites by involving the loosely bound donor electron in a donor-defect complex bond, or processes which change the acceptor concentration and thereby change the Fermi level pinning energy with respect to the shallow donor energy level.

In the case of complex formation, mobile point defects which exhibit acceptor-like properties and are negatively ionized will bond with the positively charged, ionized donor sites due to the coulombic attraction between the sites. An example of this process would be a bound state of silicon substitutional donors with mobile nitrogen interstitials in GaN. The resulting donor-defect complex may not exhibit paramagnetic properties and certainly will be distinct in those properties from the donor site which it replaces. This process will clearly require a level of mobility by the defect sites, and would not be expected to occur for very low temperature irradiations; this has been experimentally

verified by ODMR measurements on electron irradiated GaN [37] by observations of reduced complex formation with decreasing temperature. The marked temperature dependence observed in this study is indicative of a mobility limited process such as donor-defect complex formation.

Donor-defect complex formation will reduce donor concentration in a manner that is dependent upon both radiation fluence (by way of the defect formation rates) and donor concentration, as given by Boudinov, *et al* [58] as:

$$n_{complex} = \alpha(T)n_D n_{def} \left( 1 - \frac{n_{complex}}{n_D} \right) \quad (18)$$

where  $\alpha(T)$  is a temperature dependent “rate constant” for the donor complex formation process,  $n_D$  is the number of ionized donors,  $n_{def}$  is the number of point defects available to react with the donors, and  $n_{complex}$  is the number of complexes present in the material. While Boudinov did not cast the rate constant as a temperature dependent function, the dependence of the process on the defect mobility clearly requires that this rate constant be temperature dependent. It is also clear from the above equation that the rate of donor-defect complex formation is dependent upon the number of unbound impurity donor sites ( $n_D - n_D^{Complex}$ ) and that the process must slow as more of these donors are converted to the complexed state.

Donor compensation by acceptor sites is observed in as-grown materials; irradiation is also expected to produce additional acceptor states in the material since some radiation-induced point defects, such as the N interstitial, are expected to be acceptor-type sites [6]. To first order there is no reason to expect that the process of defect formation is dependent upon the doping density in the virgin material, thus the

process of acceptor or trap compensation of shallow donors is a function only of the radiation dose (or fluence). The distinction between the acceptor state and the acceptor trap state is subtle: an acceptor level lies below the Fermi level, while an acceptor trap is a state above the Fermi level which exhibits a tendency to “trap” an electron in an unfilled electron orbital or bond. The trap state, being above the Fermi level, will trap electrons which are then thermally excited to the conduction band, a process which is characterized by the state lifetime.

Formation of compensating acceptor trap sites is thus independent of the donor concentration and is of a completely different nature than the complexation process described above. This process may be described by the following relationship

$$N_A^{rad} = \alpha_A \phi \quad (19)$$

where  $N_A^{rad}$  is the concentration of radiation induced acceptor-type defects,  $\alpha_A$  is the damage constant associated with this defect type, and  $\phi$  is the radiation fluence. As shown previously, donor sites are compensated by impurity acceptors in the virgin material and, to first order, irradiation should not affect this native acceptor concentration. Therefore, in any relative comparison the native impurity acceptor concentrations may be ignored and the radiation induced acceptor states treated as the predominant contributor to the change in donor charge state. Unlike the complexation process described above, the compensation process does not change the fundamental identity of the donor site *nor its bandgap level*, the acceptors instead acting to affect the Fermi level and thus the charge states of the donors.



The rate equation governing the implantation and population of radiation-induced defects and donor-defect complexes is given by Titov and Kucheyev as [59]

$$\rho f \Delta t - n_{def} \tau^{-1} - \alpha(T) n_D n_{def} \left( 1 - \frac{n_{complex}}{n_D} \right) - n_A^{rad} = 0 \quad (20)$$

where their formulation has been modified slightly to allow the inclusion of a “stable” radiation-induced acceptor concentration  $n_A^{rad}$ . In equation (20)  $\rho$  is the defect introduction rate,  $f$  is the radiation flux and other variables are as they have been defined previously. In this formulation, the strict rate balance between defect production, annealing, and donor-defect complex formation is not preserved since the build-up of an uncomplexed defect concentration is allowed due to the introduction of the  $n_A^{rad}$  term. This expression is amenable to a numerical solution, which is presented later in this discussion.

If the formulation of equation (20) for the radiation-induced trap density and donor-defect complex formation are considered in the context of charge balance, the following equation is the result

$$n_D^+ = (n_D^{tot} - n_D^{complex}) - (N_A^- + (N_T^{Rad})^-). \quad (21)$$

and the difference between the pre-irradiation and post-irradiation EPR measured donor populations must be given by

$$\Delta n_D^+ = -(N_T^{Rad})^- - n_D^{complex} \quad (22)$$

so that the change in EPR signal is a function of the fluence, which is implicit in both of these terms, and the initial donor concentration, which is implicit in the  $n_D^{complex}$  term.

When the effects of the defect interactions listed above are evaluated, it is clear that there are three cases of interest:

- a. Donor-defect complex formation is the only process affecting the donor population (“complex only” model);
- b. Radiation induced acceptors limit the donor population that can be maintained in the neutral, “EPR visible” charge state (“compensation only” model); or
- c. Both complex formation and trap introduction combine to reduce the “EPR visible” donor population (“complex + compensation” model).

The effect of these competing processes can be determined to some extent by the evaluation of equation (20) by numerical means and determining the effect on EPR or Hall measurements by use of equation (21).

Results of this modeling indicate that the effects of the processes listed above on the donor population can be identified to some extent. Figure 9 supports this contention by illustrating the difference between the “donor complex only” and “complex + compensation” models presented above. From the simulation results shown in Figure 9 it is clear that for the correct radiation doses a distinction can be drawn between the models, with the “complex only” model displaying a dependence upon the initial donor concentration that the “complex + compensation” results do not show. The model for “compensation only” donor passivation predicts a constant decrease in the donor population for a given fluence, up to the point of saturation. The same is true for the “complex + compensation” model, as all of the defects not involved in complex formation are available to compensate any remaining donors. In both of these situations, the effect of the irradiation is to simply reduce the donor concentration by a constant

amount equal to the number of radiation-induced donors. The linear relationship of the pre-irradiation data is thus reproduced in the post-irradiation case, with the slope of the linear relationship preserved and the intercept moved from zero to the donor saturation value (ie, the initial donor concentration).

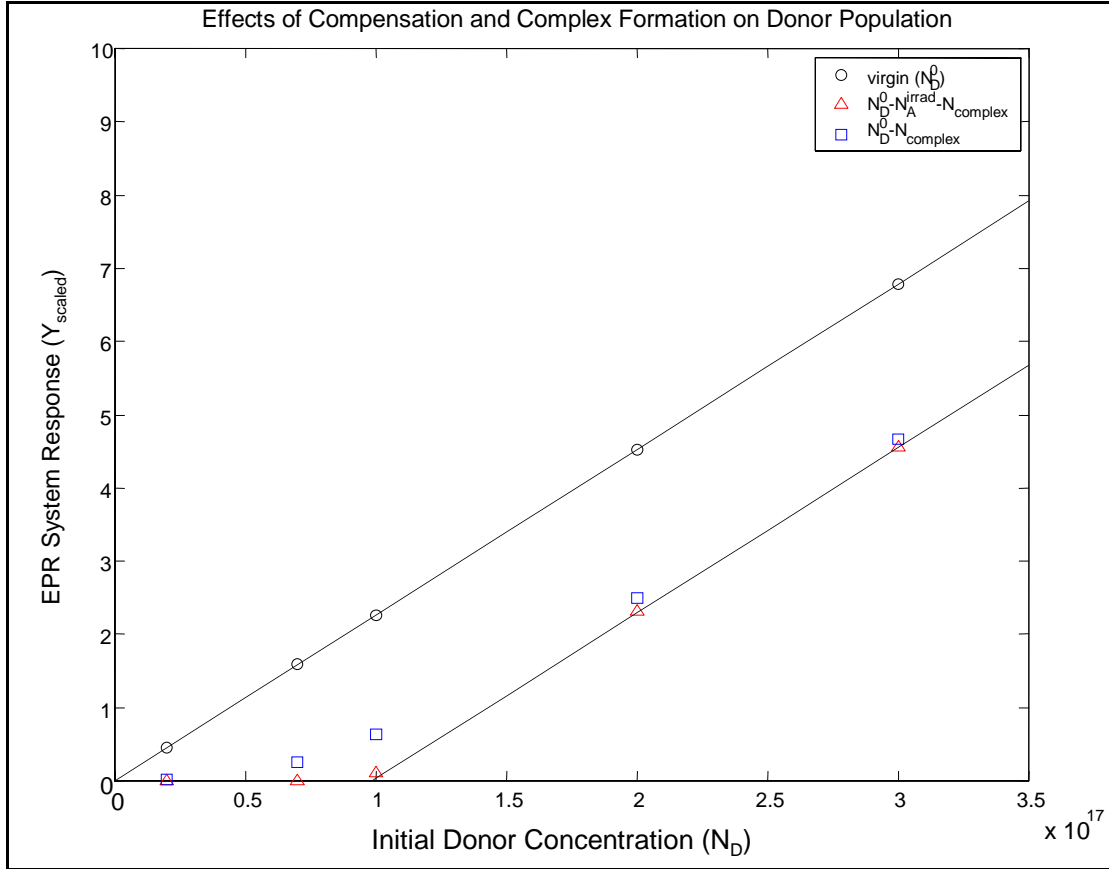


Figure 9. Results of the numerical solution of equation 20 for different initial donor concentrations. For each of the pre-irradiation donor concentrations the virgin EPR system response is shown along with the post-irradiation results for the “complex only” model and the “complex + compensation” model.

In contrast, the “complex only” model predicts that the post-irradiation donor concentrations vary from the linear pre-irradiation values. This relationship is not linear, and the limiting value in the high donor concentration regime is the total defect

concentration, as expected since a high initial donor concentration raises the probability of all radiation induced defects being bound into donor-defect complexes, especially when the total number of defects is much smaller than the initial donor concentration.

The impact of the  $\alpha$  parameter appearing in equation (20) is important in this analysis, particularly since it is a free parameter in this model, not having been experimentally determined. As  $\alpha$  approaches zero, the complexation process is “turned off” and does not occur in appreciable concentrations regardless of the defect and donor concentrations. Conversely, as  $\alpha$  goes to very large values the complexation process loses the non-linear dependence upon the donor concentration since almost every defect site available will be complexed despite dwindling concentrations of uncomplexed donor sites. It is only for values of  $\alpha$  on the order of  $10^{-18}$  to  $10^{-21}$   $\text{cm}^3/\text{sec}$  that the nonlinear donor density dependence is obvious. Therefore, differences in complex formation and defect compensation effects may be obvious only with *a priori* knowledge about the magnitude of this interaction rate constant; however, an observed deviation from linearity in the pre- and post-irradiation donor concentrations would positively indicate that complex formation is the predominant process arising from irradiation.

These results imply that it will be very difficult to differentiate between these models in an experimental setting, since the nitrogen interstitial is known to be an acceptor site and the presence of any of these defects outside of a donor-defect complex will mask the effects of the complex formation by compensating the uncomplexed donors to the level of the total defect concentration.

## Development and Application of the Hyperfine Coupling Constants

The A tensor, as described previously in the introductory section dealing with EPR spectroscopy, determines the magnitude of the EPR signal splittings due to coupling of electronic and nuclear spins. As was previously demonstrated, in the case of GaN the hyperfine coupling constants of the lattice constituents are large enough to require a complete analysis of the hyperfine splitting. We proceed with the analysis of the hyperfine spectra in GaN by first examining the development of the hyperfine coupling constant and then applying this development to the particular case of Ga or N nuclear spin coupling. Finally, the determination of the spin Hamiltonian, analysis of the resulting eigenvalues, and identification of resonant magnetic field values is presented.

The A tensor is comprised of two primary components, an isotropic term (also called the {Fermi} contact term) and a dipole term which is anisotropic due to the asymmetry of the dipole interaction. The derivation of these terms and their development is available in several texts [60] [54] and will not be repeated here; however, the dependence of the interaction on electron spin states and orbital configurations is pertinent to the discussion and will be addressed.

The dipole term is derived from a quantum mechanical computation of the magnetic dipole interaction and is given by a matrix with the elements

$$A_{\alpha,\alpha} = \frac{\mu_0}{4\pi} \mu_B g_e \gamma_N \left\langle \frac{3\alpha^2 - r^2}{r^5} \right\rangle \quad (23)$$

$$A_{\alpha,\beta} = \frac{\mu_0^2}{4\pi} g_e \gamma_N \left\langle \frac{3\alpha\beta}{r^5} \right\rangle \quad (24)$$

where the brackets indicate integration over the spatial variables, and  $\alpha$  and  $\beta$  take on values of these spatial values (such as xx, xy, yy, etc). The matrix resulting from the evaluation of these terms is traceless (i.e. zero trace) and symmetric, representing the tensor coupling of the angular momentum operators  $\vec{I}$  and  $\vec{S}$ ; therefore, we borrow Atherton's notation and call this matrix the dipolar hyperfine coupling tensor ( $\vec{A}^0$ ). This matrix can be diagonalized to recover the spatial dependence of the anisotropy. Atherton points out that the integration over the electron wavefunction leading to the development of the matrix values above exhibits a singularity at the origin. This singularity is of no consequence when the electron orbital momentum is greater than zero (all but the  $s$  orbitals), as the electron wave functions go to zero at the origin much more quickly than the singularity. For  $s$  electrons, the symmetry of the electron wave function insures that the dipole-dipole interaction upon which the expression is based is zero. Thus, the anisotropic portion of the hyperfine coupling constant arises from the interactions of electrons with nonzero orbital angular momentum ( $\ell > 0$ ).

It was initially recognized from experimental data that there must be a non-zero isotropic hyperfine coupling term due to observations of hyperfine splitting in EPR spectra of samples in solution. The isotropic component of the hyperfine coupling arises from the interaction of the spherically symmetric  $s$  orbital electrons with the nucleus. The contributions of these electrons are deduced following a quasi-classical analysis after

Atherton [60] which was first proposed by Fermi. Treating the nucleus as a spinning charged shell of radius  $r$ , angular velocity  $\bar{\omega}$ , and charge density  $\sigma$ , the magnetic field imposed for  $r < a$  is given by

$$\bar{B} = \frac{2\mu_0 \sigma a}{3} \bar{\omega} = \frac{\mu_0}{2\pi a^3} \bar{\mu}_N \quad (25)$$

where the nuclear magnetic moment is determined by calculating the field at  $r > a$  and determining the magnitude of an equivalent point dipole required to produce this field.

The energy of the interaction between the electron and the nucleus at any point within the shell is approximated by the product of the respective magnetic moments multiplied by the probability of the electron being found at the point under consideration. The electron wave function ( $\Psi(r \leq a)$ ) is taken to be approximately the value at the origin (since  $a$  is very small) and the energy is integrated over the volume of the spherical shell, yielding

$$E = -\left(\frac{4\pi a^3}{3}\right) \times |\Psi(0)|^2 \times \left\{ \mu_e \left(\frac{\mu_0}{2\pi a^3}\right) \mu_N \right\} \quad (26)$$

where  $\Psi(0)$  is the value of the electron wave function at the origin, and  $\mu_0$  is the Bohr magneton. When the magnetic moments are recast in the form of the equivalent spin operators,

$$H = \left(\frac{2\mu_0}{3}\right) |\Psi(0)|^2 (\mu_0 g_e \bar{S}) \cdot (\gamma_N \bar{I}) \quad (27)$$

The terms multiplying the spin operator dot product are collected and termed the *isotropic hyperfine coupling constant*:

$$a = \left( \frac{2\mu_0}{3} \right) \mu_0 g_e \gamma_N |\Psi(0)|^2 \quad (28)$$

Since the isotropic hyperfine constant is obviously dependent upon the electron wave function probability density at the origin, it has also been termed the *Fermi contact interaction*. This term goes to zero for any orbital possessing orbital angular momentum, since the electron wave functions must go to zero at the origin; thus the isotropic hyperfine coupling is due solely to the interactions of the  $\ell = 0$  *s* electrons. The total hyperfine coupling term may thus be represented by summing the isotropic and anisotropic portions:

$$\vec{A} = \vec{A}^0 + a\vec{I} \quad (29)$$

where  $\vec{I}$  is the identity matrix rather than the nuclear spin operator.

The effective hyperfine coupling constant  $\mathbf{A}$  is the sum of isotropic and anisotropic components. Since for gallium and nitrogen the unpaired electrons are expected to occur in the p shells, the first expectation is that the hyperfine coupling constant is comprised of the anisotropic dipole term alone; however, it has been determined that in most cases a hyperfine component exists even for filled *s* shell atoms due to screening effects of the partially filled outer shells which shield the spin up and spin down *s* states differentially, producing a non-zero *s* type spin density at the nucleus. This result implies that there will always be some admixture of isotropic and anisotropic components in the measured hyperfine components [39]



## Spin Hamiltonian and Resonance Analysis for the GaN system

The spin Hamiltonian describing nuclear coupling of the EPR active  $s=1/2$  site is composed of several terms which, depending upon the relative magnitudes of the magnetic field strength and the hyperfine coupling constant, may or may not be important to the analysis. These terms are included in the Hamiltonian below and will be discussed in turn:

$$H_{spin} = \mu_B g \vec{B} \cdot \vec{S} + \gamma_N \vec{B} \cdot \vec{I} + \vec{I} \cdot \vec{A} \cdot \vec{S} \quad (30)$$

The first term,  $\mu_B g \vec{B} \cdot \vec{S}$ , is the Zeeman splitting term and is typically the largest term in the Hamiltonian. For small values of the hyperfine coupling constant ( $\mathbf{A}$ ) or in the high-magnetic field limit, the Zeeman splitting term dominates and the other terms may be treated as perturbations or neglected.

The second term,  $\gamma_N \vec{B} \cdot \vec{I}$ , is the nuclear Zeeman term (the measured term in NMR) and is small for most nuclei since  $\gamma_N \ll \mu_B g$  and can generally be disregarded or treated as a perturbation. However, when diagonalization of the full Hamiltonian is called for, the inclusion of this term admits no additional complexities in the analysis and is typically preserved.

For the case of a large hyperfine coupling constant (or conversely of a small value of the magnetic field) the  $\vec{I} \cdot \vec{A} \cdot \vec{S}$  term must be included in the computation. The inclusion of the hyperfine coupling term introduces off-diagonal terms into the matrix representation of the Hamiltonian because the operator representation used to calculate

the contribution from the hyperfine coupling constant is comprised of the raising and lowering operators for both the nuclear and electronic spins

$$\bar{I} \cdot \bar{S} \rightarrow I_z S_z + (I_- S_+ + I_+ S_-) \quad (31)$$

where we have not included the hyperfine coupling tensor, implicitly assuming that for a single orientation it may be represented by a scalar constant,  $a$ , the hyperfine coupling constant. The operators  $I_{\pm}$  and  $S_{\pm}$  represent the application of the generic raising and lowering operators  $j_{\pm}$  to the nuclear and electronic spin states, respectively. The action of the raising and lowering operators on a given spin state is expressed as

$$j_+ |j, m_j\rangle = \sqrt{j(j+1) - m_j(m_j+1)} |j, m_j+1\rangle \quad (32)$$

$$j_- |j, m_j\rangle = \sqrt{j(j+1) - m_j(m_j-1)} |j, m_j-1\rangle \quad (33)$$

where  $|j, m_j\rangle$  is an arbitrary spin eigenvector [61].

In this operator representation the Hamiltonian for a single orientation with respect to the external magnetic field becomes

$$\mathcal{H}_{spin} = \mu_B g \bar{B} \cdot \bar{S} + \gamma_N \bar{B} \cdot \bar{I} + a I_z S_z + a(I_- S_+ + I_+ S_-) \quad (34)$$

This Hamiltonian can now be represented in matrix form in the  $\begin{pmatrix} S & I \\ m_s & m_I \end{pmatrix}$  basis, which

will be referred to as the  $|m_s, m_I\rangle$  basis for notational simplicity, with the  $S$  and  $I$

understood. For the case of a spin  $\frac{3}{2}$  nuclei and a single, spin  $\frac{1}{2}$  electron the

Hamiltonian may be expressed in matrix form as:

$$\mathcal{H} = \begin{array}{c|cccccccc}
& \left| \frac{1}{2}, \frac{3}{2} \right\rangle & \left| -\frac{1}{2}, \frac{3}{2} \right\rangle & \left| \frac{1}{2}, \frac{1}{2} \right\rangle & \left| -\frac{1}{2}, \frac{1}{2} \right\rangle & \left| \frac{1}{2}, -\frac{1}{2} \right\rangle & \left| -\frac{1}{2}, -\frac{1}{2} \right\rangle & \left| \frac{1}{2}, -\frac{3}{2} \right\rangle & \left| -\frac{1}{2}, -\frac{3}{2} \right\rangle \\
\left\langle \frac{1}{2}, \frac{3}{2} \right| & \Omega + \frac{3}{4}a & 0 & 0 & 0 & 0 & 0 & 0 & 0 \\
\left\langle -\frac{1}{2}, \frac{3}{2} \right| & 0 & \Sigma - \frac{3}{4}a & \sqrt{3}a & 0 & 0 & 0 & 0 & 0 \\
\left\langle \frac{1}{2}, \frac{1}{2} \right| & 0 & \sqrt{3}a & \Phi + \frac{1}{4}a & 0 & 0 & 0 & 0 & 0 \\
\left\langle -\frac{1}{2}, \frac{1}{2} \right| & 0 & 0 & 0 & \kappa - \frac{1}{4}a & 2a & 0 & 0 & 0 \\
\left\langle \frac{1}{2}, -\frac{1}{2} \right| & 0 & 0 & 0 & 2a & -\kappa - \frac{1}{4}a & 0 & 0 & 0 \\
\left\langle -\frac{1}{2}, -\frac{1}{2} \right| & 0 & 0 & 0 & 0 & 0 & -\Phi + \frac{1}{4}a & \sqrt{3}a & 0 \\
\left\langle \frac{1}{2}, -\frac{3}{2} \right| & 0 & 0 & 0 & 0 & 0 & \sqrt{3}a & -\Sigma - \frac{3}{4}a & 0 \\
\left\langle -\frac{1}{2}, -\frac{3}{2} \right| & 0 & 0 & 0 & 0 & 0 & 0 & 0 & -\Omega + \frac{3}{4}a
\end{array}$$

where

$$\begin{aligned}
\Omega &\equiv \left(\frac{1}{2}\right)\mu_B gB + \left(\frac{3}{2}\right)\gamma_N B, & \Sigma &\equiv -\left(\frac{1}{2}\right)\mu_B gB + \left(\frac{3}{2}\right)\gamma_N B \\
\Phi &\equiv \left(\frac{1}{2}\right)\mu_B gB + \left(\frac{1}{2}\right)\gamma_N B, & \kappa &\equiv -\left(\frac{1}{2}\right)\mu_B gB + \left(\frac{1}{2}\right)\gamma_N B
\end{aligned} \tag{35}$$

There are three immediately apparent results of this matrix formulation: 1) the matrix is still block diagonal, making an analytical solution possible without unreasonable complexity, 2) the eigenvalues will be explicit, nonlinear functions of the magnetic field strength, and 3) the eigenvalues associated with the block diagonal elements will be associated with mixed quantum states of the  $|m_s m_l\rangle$  wavefunctions.

The eigenvalues associated with the matrix above were originally given in analytical form by Breit and Rabi [62]. The eigenvalue formula, or *Breit-Rabi Formula*, is expressed in a convenient form by [63] as

$$E_{F,I,m_F} = -\frac{\Delta E_{HFS}}{2(2I+1)} + g_N \mu_N |B| m_F \pm \frac{\Delta E_{HFS}}{2} \sqrt{1 + \frac{m_F x}{2I+1} + x^2} \tag{36}$$

Where

$$x = \frac{(g_s \mu_B - g_I \mu_N) B}{\Delta E_{HFS}} \quad (37)$$

$$\Delta E_{HFS} = A \cdot \left( I + \frac{1}{2} \right) \quad (38)$$

where the parameterization is by the quantum numbers  $F$  ( $F = I + S$ ),  $I$ , and  $m_F$ ; these are good quantum numbers only in the spin coupled low-field region but are commonly used to *label* the energy levels throughout the magnetic field regime. The  $A$  parameter appearing in equation (38) is an effective hyperfine coupling constant representing some combination of the isotropic and anisotropic coupling constants. The nonlinear dependence of the energy eigenvalues on  $|\bar{B}|$  appears in the Breit-Rabi formula in the treatment of the  $x$  parameter. The eigenvalues  $E\left(\bar{B}\right)$  are shown in Figure 10 (page 54) for a spin  $\frac{3}{2}$  nuclei coupled with a single spin  $\frac{1}{2}$  electron, calculated using the Breit-Rabi formula above and parameters appropriate to a gallium nucleus.

The wavefunctions that result from the eigen-solution of the Hamiltonian matrix of equation (35) are properly labeled by the total angular momentum,  $F$ , only at zero applied field since the electron and nuclear spins are completely coupled. In the high-field regime, the electronic Zeeman term dominates and the resultant wave functions are approximately given by the simple product wavefunctions of the electron and nuclear spins  $|m_s, m_I\rangle$ . However, in the intermediate field range where the hyperfine splitting constant is of the order of the applied magnetic field mixing of the spin wavefunctions is appreciable. In this case, the mixed eigenstates that correspond to the eigenvalues obtained from the diagonalization of the Hamiltonian may be determined by application of the Clebsch-Gordan coefficients [64] for the spin coupling of interest, but common

practice in the EPR community is to label the manifold of eigenvalues by their zero-field spin labels  $F$  and  $m_F$ .

Mixing of the eigenstates of the nuclear and electron spin in the energy eigenvalue solution leads to ambiguity in the determination of which transitions are allowed EPR transitions. In the low field regime, where the Hamiltonian may be approximated by a diagonal matrix and corrections treated as perturbations, the transitions may be classified as EPR transitions or NMR transitions based upon the following rules:

$$\text{NMR} : \Delta m_I = \pm 1, \Delta m_S = 0 \quad (39)$$

$$\text{EPR} : \Delta m_I = 0, \Delta m_S = \pm 1 \quad (40)$$

However, the admixture of nuclear and electron spin states in the eigenvalues in the intermediate field region dictates that transitions cannot be so simply labeled, since the labels  $m_I$  and  $m_S$  are no longer unambiguous. The final arbiter of which states are allowed is the experimental data; many instances of “EPR forbidden” transitions occur in EPR measurements and the appearance of “NMR transitions” in EPR spectra has precedent [47]. For the purpose of this analysis, no possible transitions are discarded except those that clearly fall outside of the magnetic field regime of the experiment.

The magnetic field values at which transitions between the energy eigenstates, or “Breit-Rabi levels”, occur is determined by the resonance condition with respect to the microwave source energy,

$$\Delta E(\vec{B}) = h\nu_{\mu w} \quad (41)$$

so that once the eigenvalues are determined as a function of the magnetic field, the values of the magnetic field resonance locations ( $B_{res}$ ) may be calculated for each transition as shown in Figure 10.

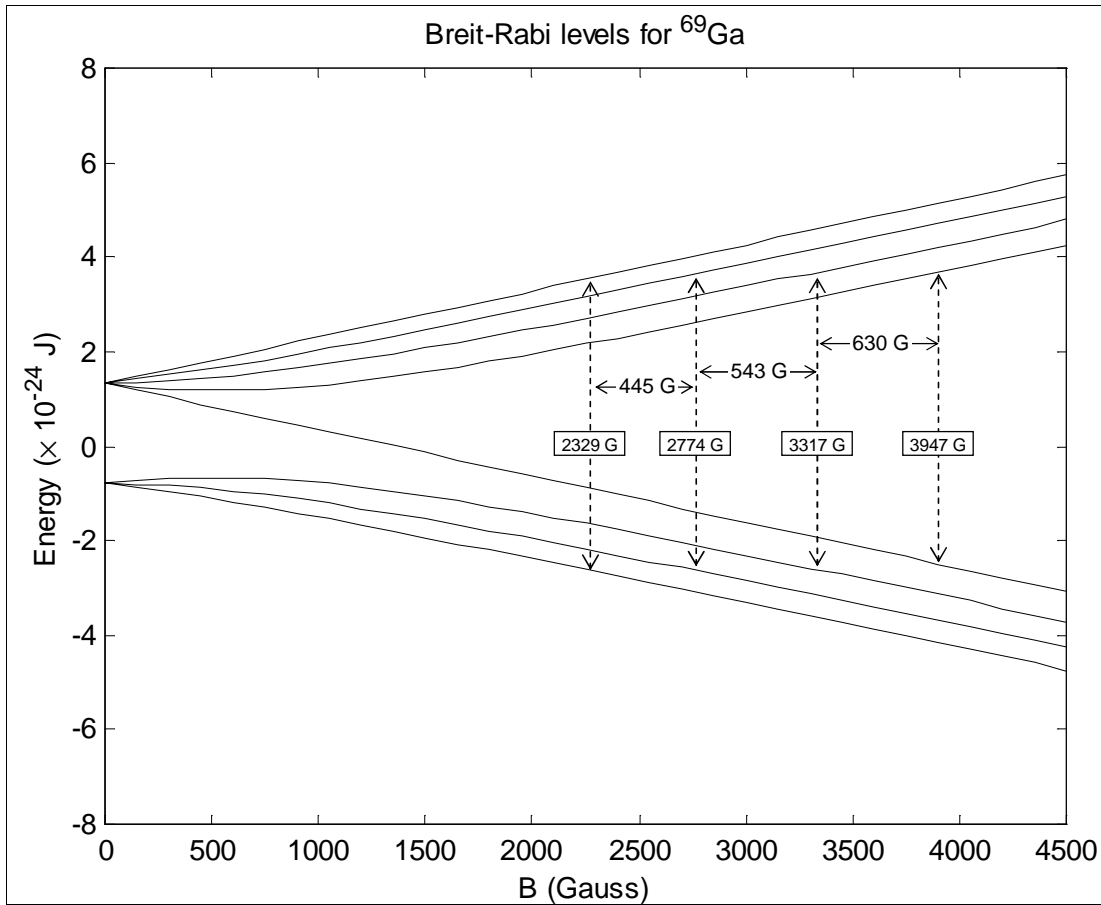


Figure 10. Breit-Rabi energy levels for the coupling of a single electron with the spin  $3/2$  nucleus  $^{69}\text{Ga}$ . Resonance locations for 9.5GHz microwave photons are shown as dashed vertical lines. The spacing between resonance locations is non-symmetric, as shown in the indicated intervals.

The model outlined above for determining the resonance values of the magnetic field is parameterized by three values: the electronic g-value, the nuclear g-value, and the

hyperfine coupling constant. The values of these three parameters which produce the best fit to the experimental data are determined and from these values a comparison with known nuclear parameters is made to identify the nucleus involved in the coupling. Other factors may affect the fitting of the experimental data, as will be discussed in the following paragraphs, but these three parameters remain the basis of the nuclear identification.

The presence of more than one naturally occurring isotope of a spin-coupled nucleus adds some complexity to the analysis of the hyperfine coupling resonances. In the case where isotopic species have differing nuclear spin values, a different Hamiltonian matrix must be determined for each of the isotopes and solutions unique to the isotope determined. Fortunately, in many cases the nuclear spins are the same and the spectral contributions of different isotopes may be calculated by simply changing the parameters associated with the isotope, primarily the hyperfine coupling constants. In the case of a nucleus having two naturally occurring isotopes (labeled  $a$  and  $b$ ) with identical spin, the hyperfine coupling constants must be related by the relationship

$$\frac{g_N^a}{g_N^b} = \frac{a^a}{a^b} \quad (42)$$

so that the relative magnitudes of the hyperfine coupling constants are constrained and do not introduce any additional degrees of freedom to the modeling process. The relationship between the ratios of the nuclear  $g$ -values and hyperfine coupling constants is a consequence of the definition of the hyperfine coupling constants discussed previously, where the hyperfine coupling constants were shown to be linearly dependent upon the nuclear  $g$ -value ( $a \propto g_N \propto \gamma_N$ ).

After the resonance locations (in magnetic field units) are determined, the hyperfine spectrum is modeled by summing the contributions of the various naturally occurring isotopes, weighted by their isotopic abundances. The resonance locations calculated by the analysis method above represent the peak locations of the microwave absorption spectrum, or the *null* locations (zero crossings) of a first-derivative spectrum. In order to facilitate simple visual comparison a Gaussian or Lorentzian derivative function is placed at each of the constituent resonant  $B$  values and it is these functions that are summed. The placement and summing of the derivative functions admits an additional fitting parameter to the model, the width of the underlying distribution function. It is not uncommon for the components of an isotropic hyperfine spectrum to display different linewidths [65], and although this is typically observed in liquid solutions where tumbling of the molecules may broaden lines anisotropically, chemical or physical processes may exist that cause anisotropic line broadening in solid state centers. The most conservative approach to choosing linewidths is to assume isotropic broadening of the hyperfine spectral components unless theoretical considerations dictate otherwise, limiting the added fitting parameters to a single linewidth parameter. Analyses presented in this work are based upon a single linewidth fit unless otherwise noted.

### ***Hall Effect Analyses***

Hall measurements performed on GaN epilayers grown upon sapphire substrates often show anomalous low temperature behavior characterized by large measured values of the carrier concentration [66]. The source of this anomalous concentration is a highly conductive, degenerate, high defect density region at the GaN/sapphire interface. This



layer is observed in MBE and HVPE grown layers as a consequence of the lattice spacing mismatch between the epilayer and substrate material.

The major impact of this degenerate layer is to mask the carrier concentration decrease at low temperatures and thus skew the interpretation of shallow donor concentrations, although Look [67] has shown that this interfacial conduction layer influences even high-temperature data. Analysis of samples exhibiting this degenerate layer is accomplished by either physically removing the layer to conduct Hall measurements on the remaining material or by compensating for the effects of this layer by a multi-layer analysis which isolates the behavior of the bulk region. This model has been developed by Look [67] and salient details are provided here as they related to the analysis of Hall measurements performed in this research.

Measurement of sample conductivity and Hall coefficients as a function of temperature are typically used to determine the carrier concentration and mobility of the samples via the relations  $\mu_H = R_H \sigma$  and  $n_H = (e R_H)^{-1}$ . Application of a multiple conducting layer model (after Look) will allow the simultaneous correction of the measured mobility and carrier concentration data. The basic relationships for a multi-layer model are simple summations

$$\sigma^S = \sum_j \sigma_j^S = \sum_j \mu_{Hj} R_{Hj}^{-1} = \sum_j \mu_{Hj} (e n_{Hj}^S) \quad (43)$$

and

$$R^S (\sigma^S)^2 = \sum_j R_j^S (\sigma_j^S)^2 = \sum_j (\mu_{Hj} R_{Hj}^{-1})^2 (R_{Hj}) = \sum_j \mu_{Hj}^2 (e n_{Hj}^S) \quad (44)$$

where the  $S$  superscript is written explicitly to denote a measured sheet ( $\text{cm}^{-2}$ ) parameter. For the case of a two layer model, we label the layers as layer 1 (the bulk or epilayer) and

layer 2 (the degenerate interfacial layer). Writing the Hall mobility and concentration in terms of  $R_H$  and  $\sigma$  and recasting the resulting equations in the form of the summations above yields expressions that can be solved for the mobility and concentration in the layer of interest (layer 1):

$$\mu_{H1} = \frac{\mu_H^2 n_H - \mu_2^2 n_{S2} / d}{\mu_H n_H - \mu_2 n_{S2} / d} \quad (45)$$

$$n_{H1} = \frac{(\mu_H n_H - \mu_2 n_{S2} / d)^2}{\mu_H^2 n_H - \mu_2^2 n_{S2} / d} \quad (46)$$

The values of the mobility and concentration in the degenerate interfacial layer ( $\mu_2, n_{S2}/d$ ) are determined by taking the values of the measured mobility and concentration in the low temperature limit, where the degenerate layer is dominant. As carriers in the non-degenerate bulk layer are frozen out with lowering temperatures, the carrier concentration measurements approach the value of the degenerate carrier density, allowing the determination of the degenerate interfacial carrier density. The application of the two layer model presented above produces mobility and concentration curves which are amenable to conventional donor/acceptor model fitting. The effects of the degenerate conduction layer and the resulting correction on a representative data set are shown in Figure 11 and Figure 12.

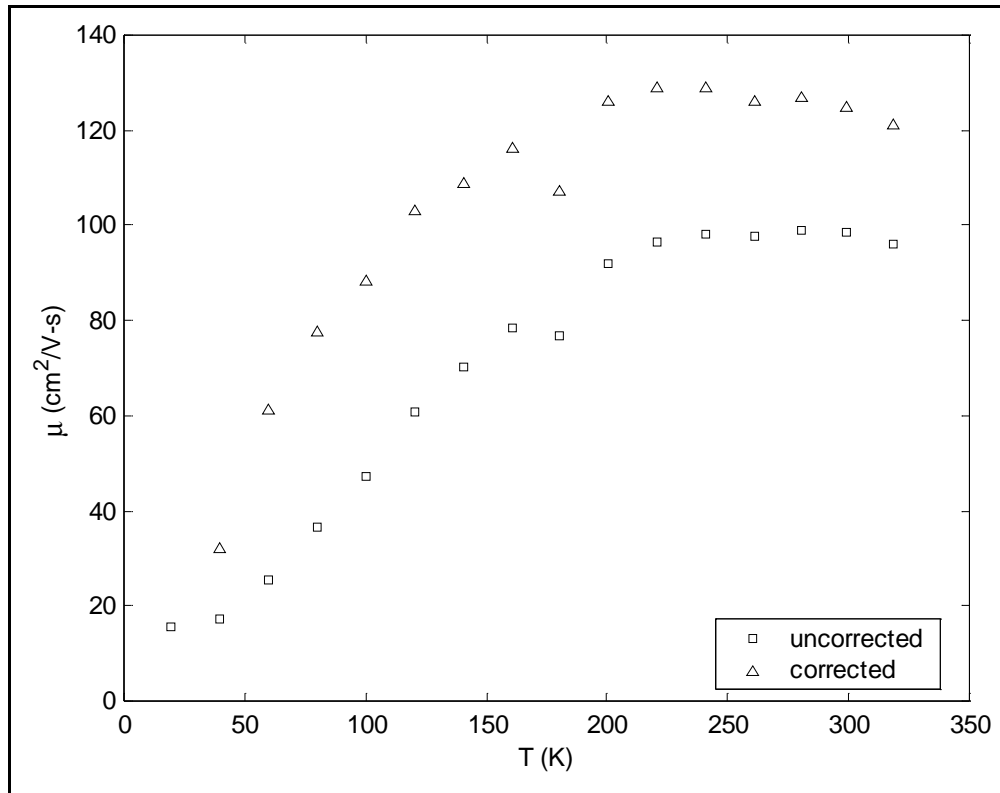


Figure 11. Hall measured mobility data from sample A342, pre- and post-correction. The effect of the degenerate layer in skewing the mobility measurement downward is apparent.

As expected, the effect of removing the degenerate, high defect density region's contribution to the carrier mobility is to increase the estimate of the mobility in the bulk region. This result is compatible with the existence of a high defect density interfacial region and a higher quality bulk region.

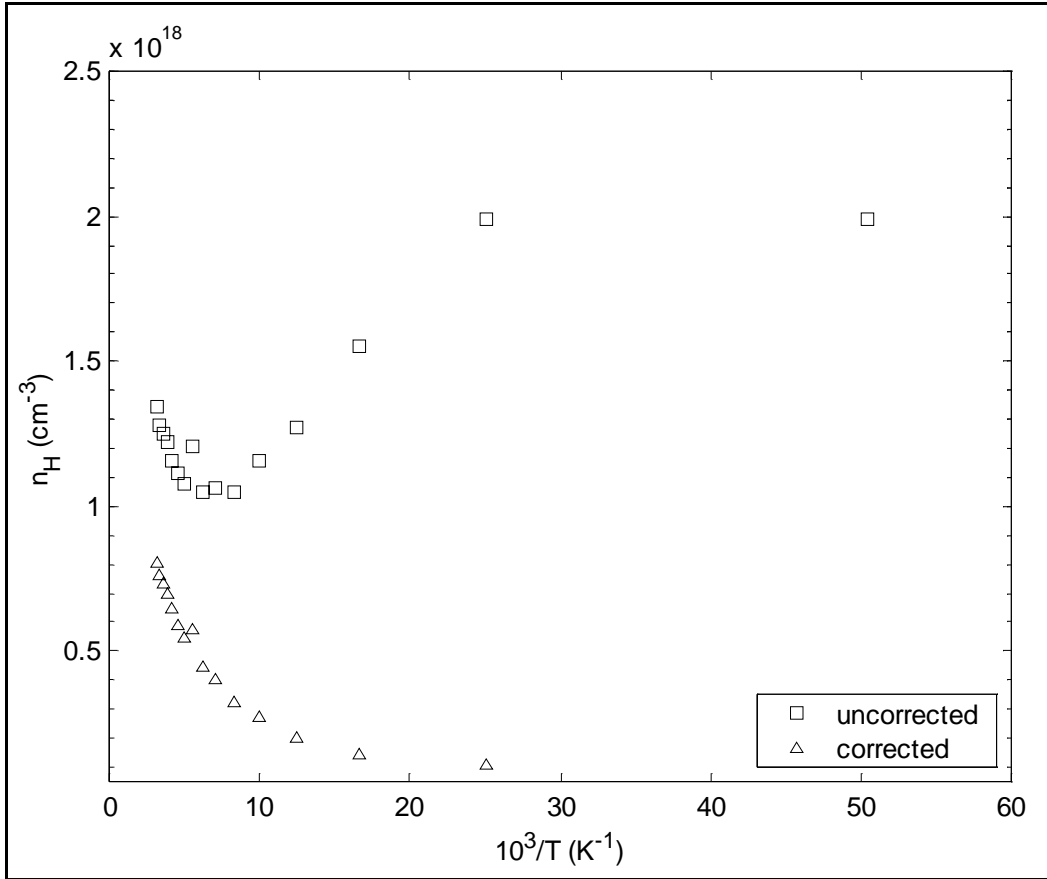


Figure 12 . Hall carrier concentration for sample A342, pre- and post-correction. The effect of the degenerate interfacial layer is apparent at low temperatures (high  $1/T$ ). The corrected data are recognized as a standard double shallow donor case.

The corrected Hall concentration data in the bulk region, as shown in Figure 12, reflect a typical  $n$  versus  $T$  curve for a non-degenerate, two donor dominant semiconductor. The corrected carrier concentration in the bulk GaN is seen to be significantly lower at all temperature values.

After the Hall data has been corrected for the interfacial layer effects, the donor and acceptor concentrations are determined by fitting a simple donor activation model to the data. The development of this model relies heavily on the single donor analysis presented by Look [68], although the specific case of two or three single shallow donors

is not explicitly covered in this reference. The two donor case is of interest because many of the samples examined in this dissertation will be shown to be of this type.

The Fermi distribution function applicable for shallow donor states is given by

$$n = \frac{N_D}{1 + \frac{1}{2} e^{(\epsilon_1 - \epsilon_f)/kT}} \quad (47)$$

where  $\epsilon_1$  is essentially the binding energy of the highest energy electron on the donor site,  $N_D$  is the donor site concentration, and  $n$  is the donated electron concentration due to the  $N_D^+$  sites. The charge balance equation in the semiconductor is given as

$$n + \sum_k N_{Ak}^- = p + \sum_m N_{Dm}^+ \quad (48)$$

where the ionized acceptor sites are summed over the index  $k$  and the ionized donor sites over the index  $m$ . In a strongly n-type material, such as GaN, we may take  $n \gg p$  and neglect the hole concentration, yielding

$$n = \sum_m N_{Dm}^+ - \sum_k N_{Ak}^- \quad (49)$$

If the range of measurement temperatures is such that the Fermi level may be assumed to vary by only a small amount in the upper regions of the band-gap, then we may assume that donors or acceptors more than a few kT from this range are temperature independent, either being completely ionized or un-ionized depending on their band-gap location. Since the Hall measurement temperatures used in this study vary from approximately 20K to 320K, it is reasonable to treat the acceptors as being completely ionized throughout. We may thus dismiss with the sum over  $k$ , being unable to differentiate between the  $k$  acceptor levels in any case, and define an effective acceptor concentration

$$N_A^{eff} = \sum_k N_{Ak}^- \approx \sum_k N_{Ak} \quad (50)$$

The effective acceptor concentration is thus just a constant to be subtracted from the carrier concentration over the temperature ranges considered.

The total carrier concentration may be related to the Fermi energy by

$$n = N_C e^{(\epsilon_f - \epsilon_C)/kT} \quad (51)$$

where  $N_C$  is the conduction band density of states,  $N_C = 2(2\pi m^*k)^{3/2} h^{-3}$ , and  $\epsilon_C$  is the conduction band-edge energy. The value of  $N_C$  is computed to be  $4.98 \times 10^{14} K^{-3/2} cm^{-3}$  for GaN ( $m^* = 0.22m_0$ ). Defining the activation energy of a site with respect to the value of the band-gap energy ( $\epsilon_G$ ) so that  $E_D = \epsilon_G - \epsilon_1$ , and combining equations 7,8 and 10, the net carrier concentration as a function of temperature may be determined:

$$n = \sum_m \frac{N_{Dm}}{1 + \frac{1}{2} \frac{n}{N_C} e^{E_{Dm}/kT}} - N_A^{eff} \quad (52)$$

where the degeneracy ratio ( $g_0/g_1$ ) is taken as  $1/2$  for the shallow donor states. The carrier concentration for two shallow donors and an undetermined number of deep acceptors, in the low to moderate temperature regime, is thus

$$n = \frac{N_{D1}}{1 + \frac{1}{2} \frac{n}{N_C} e^{E_{D1}/kT}} + \frac{N_{D2}}{1 + \frac{1}{2} \frac{n}{N_C} e^{E_{D2}/kT}} - N_A^{eff} \quad (53)$$

where the donor concentrations ( $N_{D1}$  and  $N_{D2}$ ) and activation energies ( $E_{D1}$  and  $E_{D2}$ ) may differ for donors 1 and 2. Equation 12 is parameterized by these donor concentrations and activation energies, as well as by the effective acceptor concentration ( $N_A^{eff}$ ). Given these parameters,  $n$  may be calculated numerically as a function of the temperature. In order to develop a sense of the dependencies, examples of this fitting procedure are

shown in Figure 13 for one, two and three donor models with various acceptor concentrations.

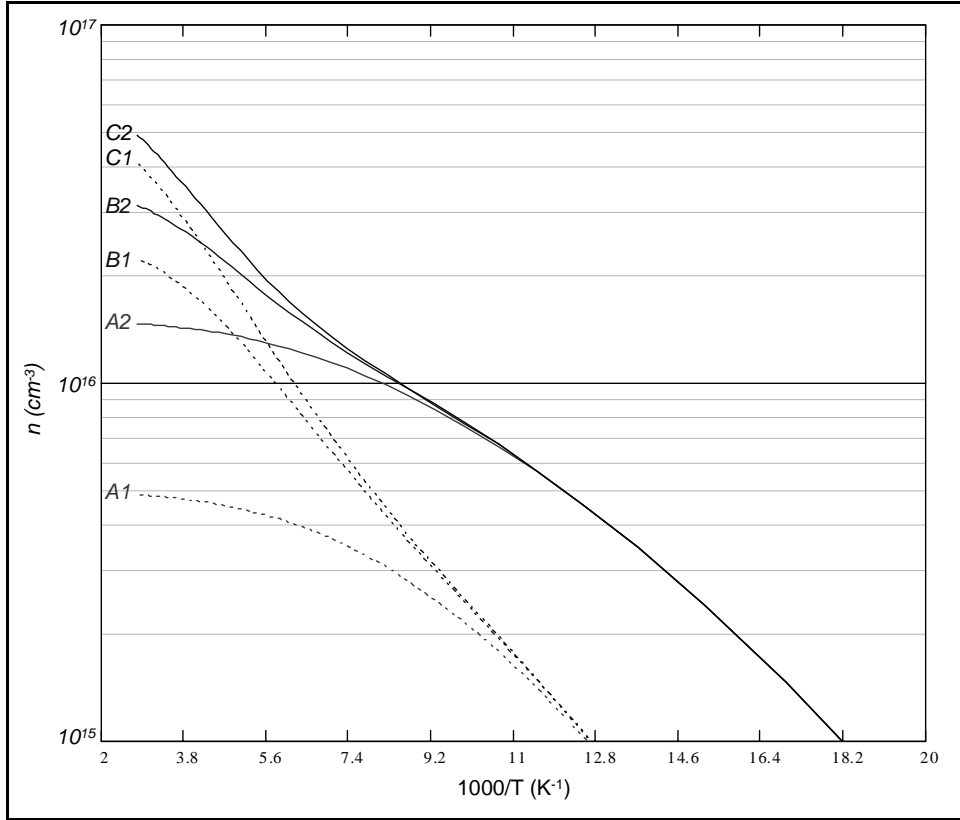


Figure 13. Examples of the donor fitting model, curves labeled *A* are one donor models, *B* are two donor models, and *C* curves are three donor models. Curves labeled *1* are for acceptor densities of  $1.5 \times 10^{16} \text{ cm}^{-3}$  and the curves labeled with *2* are for acceptor concentrations of  $5 \times 10^{15} \text{ cm}^{-3}$ .

Since the EPR measurements in this study are made at measurement temperatures below 10K, virtually all of the donor sites are in their neutral charge states, the conduction band electrons having been “frozen out”. This should hold for even the shallowest donors. Since EPR measures a single site for each spectral component, which is consistent with shallow hydrogenic donor sites [33], the shallow donor measured Hall

state may tentatively be identified with the EPR measured donor state. This correlation can be experimentally verified by comparison of the Hall shallow donor concentrations and the EPR measured concentration. These values should scale linearly if the EPR shallow donor site is truly associated with the shallowest Hall measured state. Under this assumption, changes in deeper state populations should not affect the EPR measurement of the shallow donor state.



## IV. Experimental Procedures

A description of the experimental setup and procedures must include discussion of the irradiation experiments as well as the spectroscopy experiments. Additionally, Hall Effect experiments were conducted in parallel with the spectroscopy experiments, and should be considered part of the overall experimental program. Supporting experimental methodologies include both sample preparation and properties, and dosimetry considerations.

### ***Sample Preparation and Handling***

The samples used in this dissertation were provided by a variety of sources, primary among which are Air Force Research Laboratory (AFRL) Materials and Manufacturing Directorate (ML). AFRL/ML samples were provided by Dr. Joe Van Nostrand (A342, A346, A350, A351, and A363) and Dr. David Look (SB0009B). Samples provided by Dr. Van Nostrand (A####) were grown in the late 1990's through early 2000's at AFRL/ML via MBE, and are silicon doped n-type GaN on sapphire substrates. The sample provided by Dr. Look (SB0009B) was acquired by AFRL/ML from Samsung for use in Hall effect measurements and is a 220  $\mu\text{m}$  free-standing GaN layer grown via HVPE [69]. This HVPE sample is smaller than any of the MBE samples and is the only sample of this type readily available; therefore, experimental procedure for this sample is different from other samples as there is no "control sample" to compare against. Several additional samples were initially provided by Dr. Van Nostrand with

carrier concentrations greater than  $10^{18} \text{ cm}^{-3}$ . These samples were later determined to be inappropriate for EPR measurements and were not used thereafter.

Upon receipt of samples they were sent to the packaging group of Mr. Larry Callaghan (AFRL/ML) to be diced into segments of appropriate size to fit into EPR sample tubes, nominally 3mm x 10mm. Samples were separated and labeled by subsection (A342-1, A342-2, etc). Different subsections were used to provide nearly identical experimental and control samples – typically, one subsection of a sample was irradiated while an accompanying subsection was preserved in a virgin state to compare against the irradiated sample under near identical experimental conditions. An additional subsection (nominally 4mm x 4mm) was sectioned from each sample for use in Hall effect measurements. Sample subsection physical characteristics are listed in Table 5 for samples of interest. These carrier concentration measurements and mobility measurements were taken from documents supplied by Dr. Van Nostrand with the Si doped samples, and were repeated on the subsections designated as Hall measurement samples at a later date. The concentration and mobility data shown in Table 5 are taken from the measurements provided with the samples from AFRL/ML.

**Table 5. Sample Physical Characteristics**

<i>Sample</i>	<i>Mass (gm)</i>	<i>Nominal Epitaxial Thickness (<math>\mu\text{m}</math>)</i>	<i>RT Carrier Concentration (<math>\text{cm}^{-3}</math>)</i>	<i>RT Mobility (<math>\text{cm} / \text{Vs}</math>)</i>
A342-1	0.0182	2.0	2.44E+17	68.5
A342-2	0.0393	2.0	2.44E+17	68.5
A346-1	0.0522	2.0	3.81E+17	276
A346-2	0.0514	2.0	3.81E+17	276
A350-1	0.0379	2.0	2.72E+17	141.9
A350-2	0.0178	2.0	2.72E+17	141.9
A351-1	0.0344	2.0	3.99E+17	207.5
A351-2	0.0348	2.0	3.99E+17	207.5
A363-1	0.0409	2.0	6.78E+16	104.9
A363-2	0.0383	2.0	6.78E+16	104.9
SB0009B-1	0.0192	200.0	<i>Not available</i>	<i>Not available</i>
SB0009B-2	0.0114	200.0	<i>Not available</i>	<i>Not available</i>

Samples were stored out of direct UV exposure (predominantly sunlight) at room temperature in clean sample holders until irradiated. Following irradiation, samples were loaded into EPR sample tubes immediately and thereafter were kept immersed in liquid nitrogen (LN<sub>2</sub>) until EPR or Hall measurements could be performed. This cryogenic storage technique was used in order to ameliorate annealing effects. For both EPR and Hall measurements, low temperatures are required and the samples were exposed to the temperature profiles required of the measurement process – typically very fast reduction from room temperature to approximately 4K in the case of EPR measurements or reduction from room temperature to approximately 20K followed by a slow warm-up to room temperature in the case of Hall measurements. In both cases, the time at room temperature prior to performing the experimental measurements is kept at the lowest practicable level. For EPR measurements, this time is on the order of eight to 15 minutes

total room temperature exposure prior to measurement. For Hall measurements, the time is longer and there is some localized sample heating due to the requirement to apply contacts to the samples after the irradiations are performed.

Following measurement, EPR samples are replaced in LN2 for cold storage prior to additional EPR measurements or are left at room temperature in the case of isochronal annealing studies. Samples that are to be annealed at room temperature are typically annealed in a quartz sample tube under ambient atmosphere.

Sample cleaning is accomplished by swabbing with methanol or acetone (where required) followed immediately by rinsing with de-ionized water. Samples were typically cleaned in this fashion previous to first irradiation, when contaminated by the vacuum grease or rubber cement typically used for sample mounting, or when contamination was visible on the samples.

### ***Irradiation Experiments***

Irradiations were all performed at the Wright State University (WSU) Van de Graff (VDG) facility and were performed by Maj Greene under the guidance of Dr. Gary Farlow, of the WSU faculty. All operators are trained on VDG operations and safety, as well as completing the WSU radiation safety training course.

The VDG at WSU is a low- to mid-energy accelerator, routinely operating in the 500keV to 1.8 MeV range, with beam currents less than 30  $\mu$ A. Beam uniformity is typically good, with a temporal current deviation estimated at approximately  $\pm 3\%$  and a temporal energy deviation estimated at approximately  $\pm 5\%$  (P-V). These values are derived from operator experience and observation. Spatial beam uniformity over a 2 cm

by 2 cm square is estimated by the WSU VDG facility staff at  $\pm 2\text{-}3\%$  from optical measurements of irradiated plastics.

The irradiation chamber consists of an evacuated ( $2 \cdot 10^{-6}$  torr) aluminum cylinder, equipped with a magnetic beam steering system and an aperture for control of secondary emissions. The chamber is capped with a cryogenically cooled vacuum cap which incorporates the sample mounting stage as well as electrical pass-through lines for electrical and temperature measurements. *In-situ* electrical measurements of GaN samples were not performed during any of the experiments; however, temperatures were cryogenically controlled and remotely monitored during irradiations when possible. Irradiations in this study were performed with the beam parameters listed in Table 6. Irradiation flux levels were limited to approximately  $20 \mu\text{A}$  ( $1.2 \times 10^{14}$  electrons/sec) as an attempt to control dose rate dependent effects [70].

**Table 6. VDG Irradiation Parameters**

<b>Irradiation Date / Samples Irradiated</b>	<b>Beam Current/Flux</b>	<b>Particle Energy</b>	<b>Total Fluence</b>
12 May 03 A342-1, A363-1 A350-1 A351-1, SB0009B-1	$20 \mu\text{A} / 1.2 \times 10^{14} \text{ s}^{-1}$	1.0 MeV	$1 \times 10^{18} \text{ e}^- \text{ cm}^{-2}$
17 Jun 03 A350H1, A351H1	$20 \mu\text{A} / 1.2 \times 10^{14} \text{ s}^{-1}$	1.0 MeV	$1 \times 10^{18} \text{ e}^- \text{ cm}^{-2}$
11 Apr 03 A342H1, A342-1, A351-1	$10 \mu\text{A} / 6 \times 10^{13} \text{ s}^{-1}$	1.0 MeV	$1 \times 10^{17} \text{ e}^- \text{ cm}^{-2}$
11 Mar 03 A342-1	$10 \mu\text{A} / 6 \times 10^{13} \text{ s}^{-1}$	1.0 MeV	$1 \times 10^{16} \text{ e}^- \text{ cm}^{-2}$
30 Sep 02 GaN / Sapphire	$20 \mu\text{A} / 1.2 \times 10^{14} \text{ s}^{-1}$	1.5 MeV	$2 \times 10^{17} \text{ e}^- \text{ cm}^{-2}$
30 Jul 02 GaN/Sapphire	$10 \mu\text{A} / 6 \times 10^{13} \text{ s}^{-1}$	0.5 MeV	$1 \times 10^{17} \text{ e}^- \text{ cm}^{-2}$

The cryogenically cooled sample stage and vacuum cap discussed above was machined for this experiment by the AFIT model shop in order to cool the samples during irradiation and permit the temperature and electrical measurements to be made while maintaining the vacuum integrity of the system. This sample stage is shown in Figure 14.

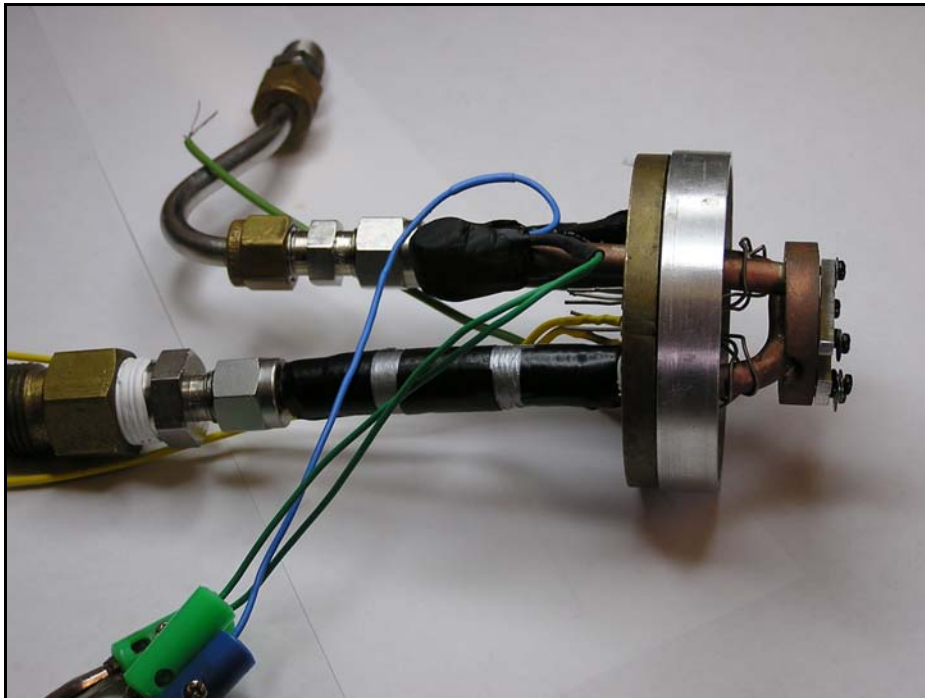


Figure 14. Cold head and sample mount assembly.

The original WSU VDG setup used a sample mount which was water cooled, the mount being cooled primarily to prevent heat build-up in the vacuum chamber itself. Due to reports of defect annealing at room temperatures in GaN [37] and estimates of sample temperatures as high as 200° C, the new system was designed to perform cooling of the sample by liquid nitrogen (LN2). Further modifications of the system were made

to insure coolant flow (prevent vapor lock) and to accurately determine the sample stage temperature during irradiation (inclusion of an embedded resistance thermal device or RTD). In the final configuration, the cold head achieved minimum sample stage temperatures of 84K, and was able to maintain sample stage temperatures below 95K during 20  $\mu\text{A}$  irradiations. Temperature control was demonstrated over periods of 3-6 hours, after which LN2 dewars must be replaced. Temperature profiles using this cold head design, as measured by an embedded Resistive Temperature Device (RTD) are shown in Figure 15.

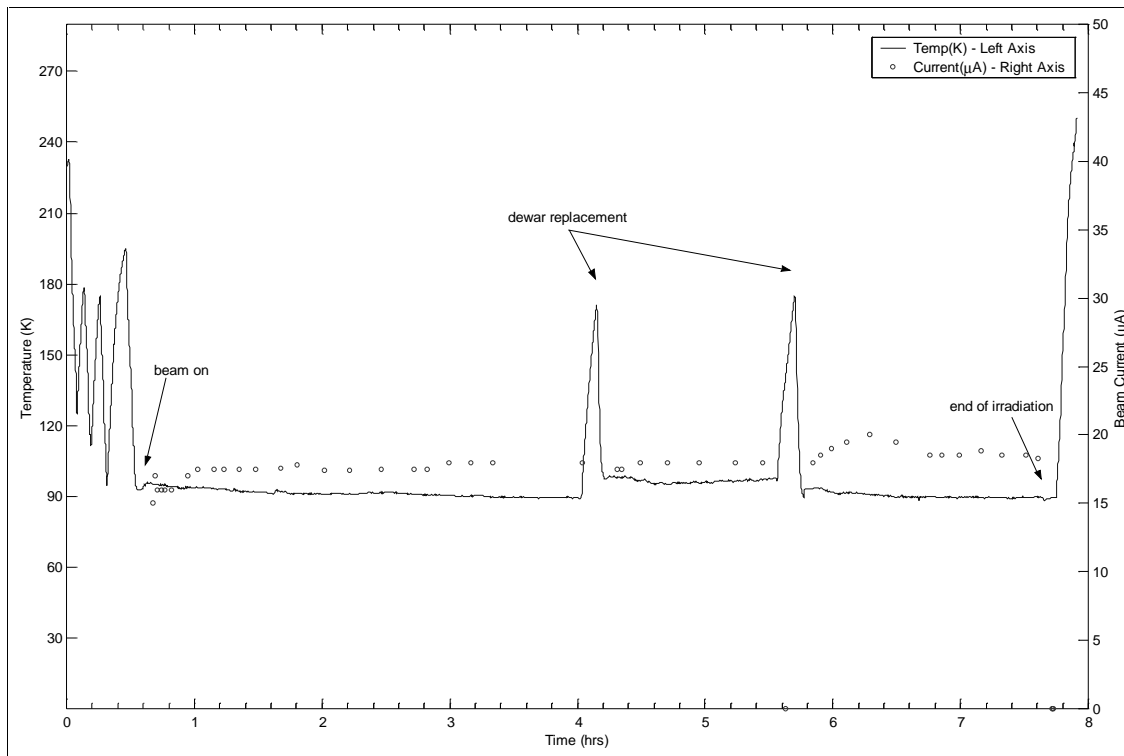


Figure 15. Typical temperature profile for long irradiations. Data is from a  $10^{18} \text{ e}^-/\text{cm}^2$  irradiation at approximately 20  $\mu\text{A}$  beam current performed on 12 May 2003.

In a typical experimental run, the VDG system would be “exercised” on the day prior to the irradiation by setting up and running the system at the desired energy and current for 1-2 hours. This procedure allows the tuning of the energy and current without inclusion of the sample, as this process may take considerable time before stability is achieved. After a stable setup is achieved, the system is allowed to run for 1-2 hours in order to check stability and because the system becomes more stable as it is allowed to run at the desired set point. This procedure allows the sample irradiation to begin at the desired setpoint on the following day, minimizing dose and dose rate excursions.

After the exercise of the system, the vacuum chamber is opened and the samples mounted to the sample stage. Typically, up to three samples (approximately 10mm x 3mm) are mounted on the stage at one time to provide comparison of samples under identical irradiation conditions. Samples were often accompanied by 3.175mm x 3.175mm TLD-400 chips and larger 10mm x 10mm (approximate) material samples for Hall Effect measurements. The mounting was initially accomplished by means of applying a small amount of Apiezon Type N vacuum grease. This vacuum grease is not EPR active in its unirradiated state; however, upon irradiation the vacuum grease takes on a crystalline form and exhibits an EPR absorption peak (see Experimental Results section for details). Due to EPR interference from the irradiated vacuum grease signal, the cold head assembly was modified to mechanically mount samples. The majority of sample irradiations were performed without grease mounting using this physical clamping system. Only very small portions of the samples were shielded by the aluminum mounting bars; no appreciable effect on the EPR measurements is expected due to the small percentage of the total volume being shielded.



After sample mounting, the stage is affixed to the vacuum chamber and the chamber is pumped down to the desired pressure for approximately 12-24 hours. Before irradiation on the following day, the LN2 connections are fitted and the instrumentation cabling run from the control room for experiment monitoring. During irradiation, all personnel are evacuated from the room and the VDG room is alarmed to prevent personnel exposure to the high secondary (x-ray) radiation levels.

Beam current and total fluence are measured by current collection and integration via the conducting end-cap and sample mount. This is performed by an electrical connection which leads to an ammeter and signal integrator in the control room. This charge collection method is the basis of the measurement of electron fluence values.

Irradiations were performed to the specifications of irradiation energy and dose shown in Table 7.

**Table 7. Irradiation Specifications**

<b>Irradiation Batch</b>	<b>Energy</b>	<b>Dose</b>	<b>Samples</b>	<b>Purpose</b>
02/03 – 01	1.0 MeV	0.44 Mrad(GaN) $1 \cdot 10^{16} \text{ e}^-/\text{cm}^2$	A342	EPR NRL/DC
03/03 -01	1.0 MeV	0.44 Mrad(GaN) $1 \cdot 10^{16} \text{ e}^-/\text{cm}^2$	A342, A350	EPR NRL/DC
04/03 -01	1.0 MeV	4.41 Mrad(GaN) $1 \cdot 10^{17} \text{ e}^-/\text{cm}^2$	A342, A350,	EPR NRL/DC
05/03 – 01	1.0 MeV	4.41 Mrad(GaN) $1 \cdot 10^{17} \text{ e}^-/\text{cm}^2$	A342H1, A363H1, A350H1	Hall Measurement
05/03 – 02	1.0 MeV	4.41 Mrad(GaN) add 200 um dose $1 \cdot 10^{18} \text{ e}^-/\text{cm}^2$	A342, A346, A350, A351, SB0009B	EPR NRL/DC

After the conclusion of irradiation, the sample is removed from the vacuum chamber (after appropriate safety checks have been performed) and removed from the sample stage. The samples are immediately placed into quartz holders and submerged in LN2 for transport. Samples are kept at cryogenic temperatures throughout the transport and measurement processes in order to reduce the impact of thermal annealing until annealing measurements are performed.

## ***Dosimetry***

All dosimetry during the irradiations was performed by means of current integration. The sample stage and supporting structure are electrically grounded from the Van de Graff generator structure and beam tube, allowing a measurement of the charge deposition at the sample. The current generated from the electron beam interaction with the stage is monitored, measured, and integrated for a running measurement of the total beam fluence on the target region. TLD-400 thermoluminescent dosimeters were investigated as a possible means of conducting independent dosimetry; however, at the high doses ( $> 10$  Mrad) used in this experiment the TLD response curve was insufficient to provide good dosimetry. A suitable TLD material for the energy and dose values used was not identified, leading to the decision to calculate deposited doses.

Dosimetry calculations were performed to translate the measured charge deposition (which results in a measure of the total fluence,  $\phi$ ) into an estimate of the *deposited* dose in the sample of interest. These calculations were performed using the

TIGER Monte Carlo electron transport codes [71] to determine deposited energy in the material as a function of the total fluence.

Calculation of the electron stopping power of the various materials under study was performed via the XGEN code (part of the TIGER package) from the material parameters shown in Table 8. These material parameters were used to compute the stopping powers shown in Figure 16. Silicon is computed as a reference point for dose calculations.

**Table 8. Material Parameters used for Dose Calculations**

<i>Material</i>	<i>Weight Fractions</i>		<i>Density (g/cm<sup>3</sup>)</i>
Si	Si – 1.0	N/A	2.33
GaN	Ga – 0.8327	N – 0.1673	6.15
Al <sub>2</sub> O <sub>3</sub>	Al – 0.5293	O – 0.4707	3.98

Sample geometries, source characteristics, and monte carlo parameters (histories, batches, etc) were input following the calculation and tabulation of the material stopping powers and the one dimensional simulation, tiger.exe, was used to estimate the energy deposited *in the GaN layer*. This calculated dose value is dependent upon both the total fluence and the energy of the electron beam. Beams were assumed to be oriented perpendicular to the GaN face of the samples, and were assumed to be comprised of monoenergetic electrons. Doses were computed for a variety of beam energies, and since the code output is in energy deposition units of  $(MeV \cdot cm^2)/(g \cdot source\ particle)$  the total dose is easily scaled with the fluence.

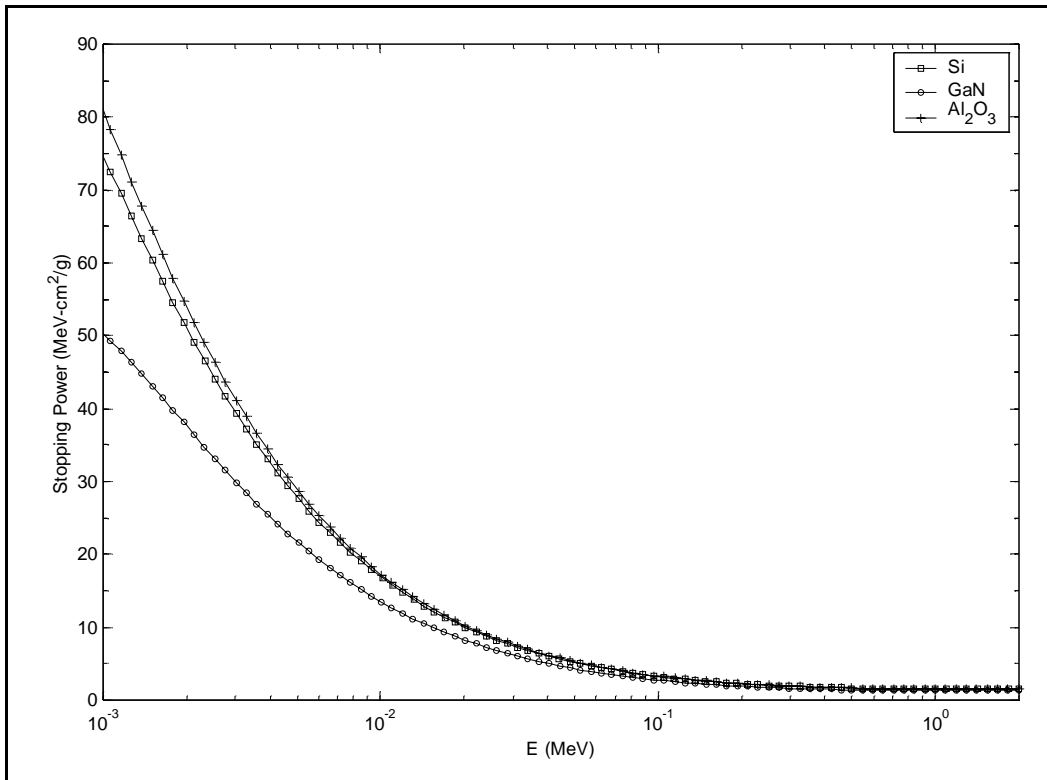


Figure 16. Electron stopping powers as calculated by XGEN for materials of interest.

The dose deposition profile in a typical GaN epilayer of 2.0  $\mu\text{m}$  on a sapphire substrate is shown in Figure 17. The majority of the absorbed dose is clearly in the sapphire substrate (note relative thicknesses). All quoted dose values from this point forward are the GaN absorbed dose, calculated by integration of the deposited dose over the GaN sample thickness unless otherwise noted.

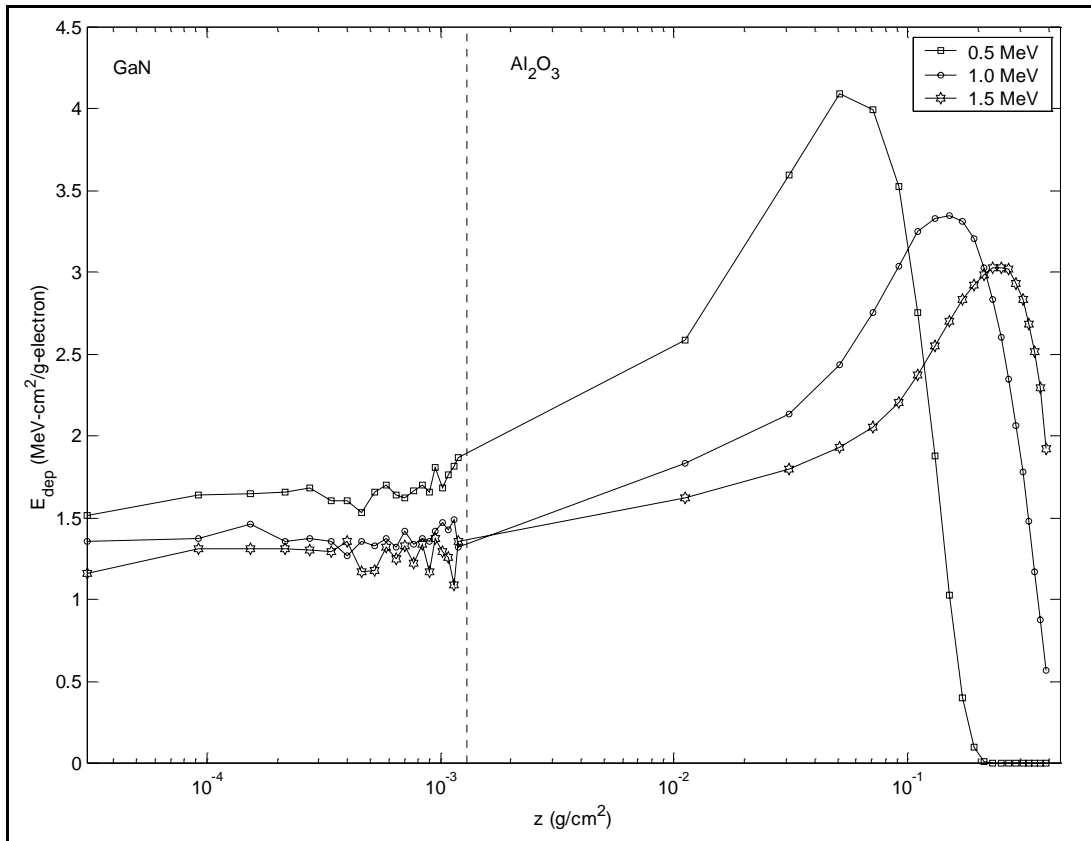


Figure 17. Dose deposition profiles for GaN (2  $\mu\text{m}$ ) on  $\text{Al}_2\text{O}_3$  (1 mm) for particle energies of 0.5, 1.0, and 1.5 MeV. Calculation was performed using 200,000 histories in 20 batches in TIGER.

After scaling by the total fluence, and applying the proper unit conversions, a set of dose curves (dose in MRad(GaN) vs  $\phi$ ) can be calculated. The calculated curves for fluences of  $10^{17}$  to  $10^{18}$   $\text{e}^-/\text{cm}^2$  at energies of 0.5, 1.0, and 1.5 MeV for the 2  $\mu\text{m}$  films discussed above and the 200  $\mu\text{m}$  free standing GaN sample are shown in Figure 18.

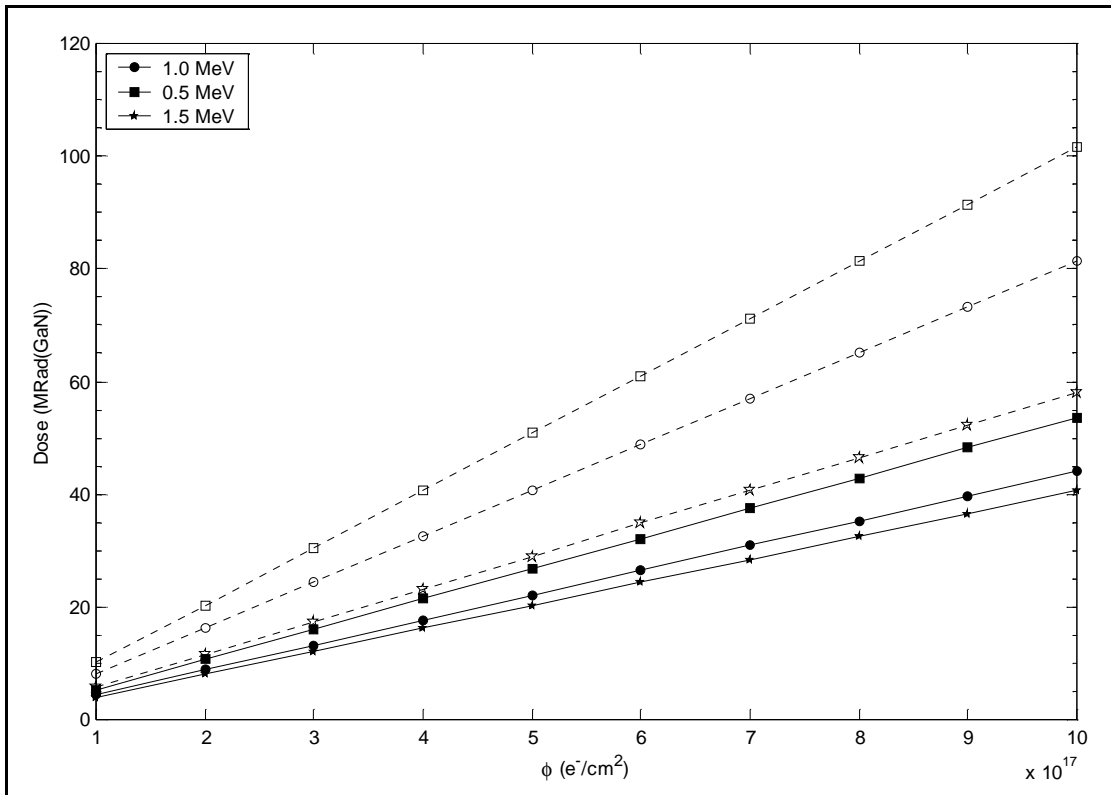


Figure 18. Dose curves (MRad(GaN) vs  $\phi$ ) produced via TIGER. Results for  $2\mu\text{m}$  GaN films on  $\text{Al}_2\text{O}_3$  are shown as solid lines and filled symbols. Results for  $200\mu\text{m}$  free-standing layers are shown with dashed lines and open symbols.

The values displayed in Figure 18 are used as the dose estimates throughout the dissertation. All dose values listed have been calculated using the appropriate beam energies, sample thicknesses and geometries, and fluence levels.

## ***Spectroscopy***

Spectroscopy was performed using an X-band (9.5 GHz) EPR spectrometer manufactured by Bruker Inc. and provided by AFRL/ML. Due to equipment difficulties with the liquid helium (LHe) cooling system, the majority of the EPR spectroscopy was

performed on a similar Bruker EPR-300 system located at Naval Research Laboratory (NRL), DC in Washington DC. This system was provided by Dr. William Carlos.

Prior to use, the various EPR systems were calibrated using standard weak pitch sources to determine the stability and accuracy of the g-value determination. The g-value measured was determined to be accurate within  $\pm 0.002$  for the samples examined.

To provide physical mounting of the samples within the microwave cavity and maintain good thermal contact between the sample and LHe coolant flow standard Wilmad EPR Sample tubes (quartz, 4mm ID) were modified by grinding a coolant hole in the bottom of the sample tube and annealing. Tubes were abraded until the form of Figure 19 was achieved, and then annealed at 1000° C for approximately 1 hour. This arrangement allows a rectangular sample of approximately 3mm-4mm width to rest in the bottom of the tube as shown, while LHe is free to flow through the tube opening and cool the sample directly. Samples mounted in this manner are not only efficiently cooled, but the samples are not required to be mounted using contact cement, vacuum grease, or other substances which could produce an EPR signature of varying magnitude.

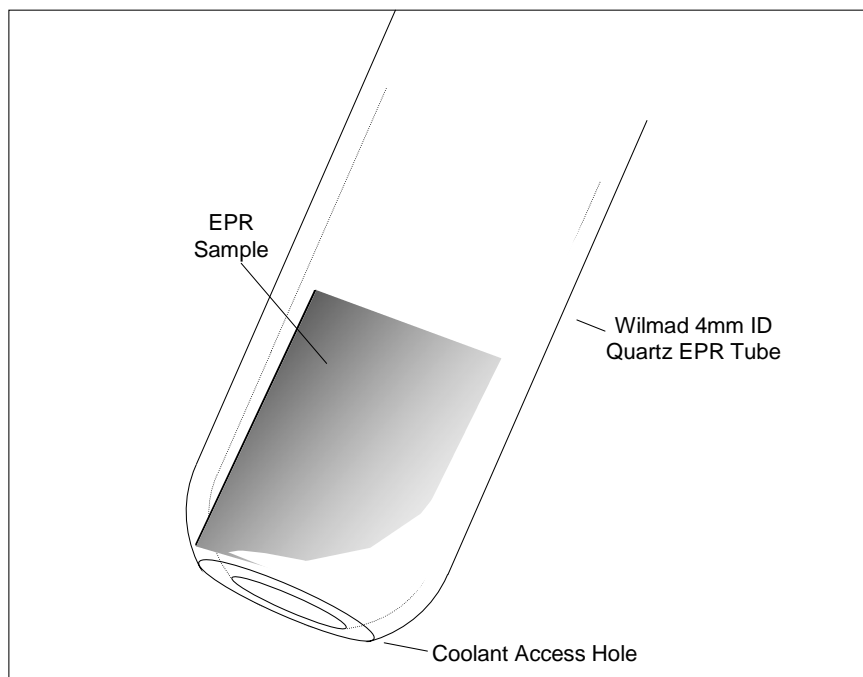


Figure 19. Sample mount and cooling flow arrangement. Open-ended tube arrangement shown is required to cool samples to near 4K.

Relative intensity measurements require a spin standard to provide a reference signal that does not interfere with the signal to be measured and that can be measured simultaneously with the sample of interest. These requirements were met by the quartz sample tubes used with the EPR measurement system. In particular, each sample tube was found to exhibit a characteristic signal at  $g=2.007\pm 0.002$  which could be used to compare the relative signal intensities of samples measured in the same tube. The signals from these tubes are independent of angular orientation and are not easily saturated at low temperatures, thus forming an ideal spin reference for relative magnitude comparisons. Sample tubes were labeled and measurements involving spin comparisons were performed in identical sample tubes at identical locations within the microwave cavity.



Signal peak scaling was performed in the post-measurement analysis phase using this spin standard as a reference.

The spectrometer is equipped with a goniometer to measure the angular displacement of the sample with respect to a fixed (arbitrary) reference point. Alignment of the sample with respect to the magnetic field axis is manually accomplished (which produces an alignment to within  $\pm 15^\circ$  typically). Determination of the sample angle with respect to the magnetic field is accomplished in the data analysis phase by investigating the symmetry points of the signal anisotropy. A goniometer was not available on the NRL/DC Bruker ESR-300; thus, angular measurements were limited to relatively large values of  $\Delta\theta$  and were of lower precision, typically on the order of  $\pm 15^\circ$ .

The sample cavity is cooled to a level between 50K and 100K prior to introducing the sample tube and sample. This is required to minimize the temperature cycling of the sample during the handling and cooldown process. The sample is cooled to the operating temperature of approximately 4K within 30-40 minutes during typical operation. As sample cooling is provided in both the AFRL/ML and NRL/DC spectrometers by a LHe system, the cryostats associated with the spectrometer (as well as accompanying transfer lines) must be maintained at vacuums on the order of  $1 \times 10^{-5}$  torr or below.

Cryostat and transfer line arrangements were similar for both EPR systems used, featuring evacuated cryostat chambers specially configured to mate with the spectrometer's microwave cavity. The cryostat chambers typically house a thermal sensor (thermocouple or RTD sensor), heater units, wiring for heaters and sensors, and transfer tubes for the LHe coolant as well as exhaust gas. Such cavities must be pumped to vacuum prior to each use, due to outgassing and moderate leak-up rates. This was

accomplished by means of a turbo pump with cold trap in the case of the NRL/DC setup, and a dry turbo pump for the AFRL/ML spectrometer.

Typical spectrometer parameters are shown in Table 9 and were optimized for detection of signals due to impurities or defects in solid state materials. Spectrometer parameters were initially based on suggested settings from Bruker and were optimized by experimentation with the samples under consideration.

**Table 9. Spectrometer Parameters**

Bruker EMX (AFRL/ML)		Dr. Carlos Spectrometer NRL/DC	
Parameter	Value	Parameter	Value
Microwave Frequency	9.48 GHz	Microwave Frequency	9.51 GHz
Microwave Power	1.0 – 10.0 mW	Microwave Power	1.0 – 10.0 mW
Modulation Frequency	100 kHz	Modulation Frequency	100 kHz
Modulation Amplitude	3 G	Modulation Amplitude	2.85 GHz
Conversion Time	40-163 msec	Conversion Time	40-163 msec
Time Constant	81 – 326 msec	Time Constant	81 – 326 msec
Receiver Gain	$10^5$	Receiver Gain	$10^5$
Operating Temperature	4.2 K	Operating Temperature	4.2 K

The spectrometer parameters of Table 9 were chosen (or recorded) based upon experimental constraints and experience. Parameters were chosen based upon the rationale and constraints below in the following paragraphs.

Microwave frequency is a characteristic of the microwave cavity, waveguides, and microwave generation system and is thus not amenable to modification; therefore, it is simply measured and recorded.

The microwave power is user selectable and is determined based upon the competing requirements to maximize signal strength (higher power) and to avoid saturation of the absorption signal at high powers. Typically, the signals under observation in this research project were undetectable with power levels of less than 1.0 mW; saturation began appear at powers greater than 10 mW.

The modulation amplitude is set at the maximum level that does not affect the lineshape of the measured signal by producing distortion or excessive non-symmetric linewidths. Higher amplitudes are found to substantially increase the SNR of the measurement up to the point of the onset of signal distortion. In the samples under investigation, 3 Gauss was found to provide good SNR without distorting the lineshape.

Conversion time and the time constant are related, in that the conversion time essentially represents the time the system spends integrating at each measurement step, while the time constant is basically a noise filter on the input signal. The value of the conversion time is based in part on the inherent signal strength of the sample and upon experimental constraints. It was found that a ratio of approximately 2/1 between the time constant and conversion time produces reasonably smooth absorption signatures without noticeable smearing or distortion of the signal.

Receiver gain is typically set as high as is practicable to avoid signal channel overflows. The advent of a signal channel overflow is signaled by a message to the user

on both spectrometers used in this research – allowing the run to be re-performed with a lower receiver gain selected.

## ***Hall Effect Measurements***

Hall measurements were performed by Mr. Tim Cooper of AFRL/ML on samples provided by Maj Greene. Temperature dependant Hall (T-Hall) measurements were performed on a Lakeshore Model 7507 system equipped with a closed cycle He cooling system for temperature stabilization between 15K and 320K. The samples were kept at LN<sub>2</sub> temperature up until the process of applying (or reapplying) contacts was begun. Indium solder contacts were applied by hand by Mr. Cooper, and were not subjected to any additional treatments. Samples used for Hall measurements typically measured approximately 4mm x 4mm square. Measurements were performed at 5K or 10K increments from approximately 20K to 320K.

## V. Experimental Results

### *Sapphire (Al<sub>2</sub>O<sub>3</sub>) Results*

Sapphire is a nearly constant companion to the materials investigated in this experiment due to its presence as a ubiquitous substrate material. The presence of sapphire, or more properly of corundum (impurity free Al<sub>2</sub>O<sub>3</sub>) [72] is of interest to the EPR spectroscopist due to the large number of strong paramagnetic absorption peaks characteristic of this material.

Attempts to find reference materials or published data on the properties of characteristic EPR signals of corundum proved futile, and the lack of reference materials was verified by discussions with experienced researchers in this field [73]. Accordingly, pre-irradiation and post-irradiation baseline measurements of simple corundum substrates were conducted to determine their EPR spectra and behaviors.

When samples were appropriately cooled (requiring modification of quartz sample tubes to prevent insulation of the samples) it was found that the sapphire signals were typically strongly saturated at the 1.0-10.0 mW microwave powers typically used in this experimental effort. Under these conditions, sapphire lines were not evident in the sample spectra at temperatures less than 30K. As sample temperatures approach 25-30K and above, the presence of spectral lines attributed to sapphire is again noticed, and sapphire signals may be present in a highly saturated form (low magnitude) at even lower temperatures when long integration times are used.

Sapphire substrate spectra measured over a range of magnetic field angles ( $-80^{\circ}$ - $80^{\circ}$ ) are shown in Figure 20. These spectra were obtained at operating temperatures of 20K-30K, near the level at which saturation would begin to occur. The most noticeable feature of these spectral lines are the pronounced anisotropies with field angle rotation. This strong anisotropy provides a means of differentiating these signals from the GaN signals of interest. The signals observed in the sapphire substrates are also very narrow, allowing differentiation from GaN spectral lines which are typically wider.

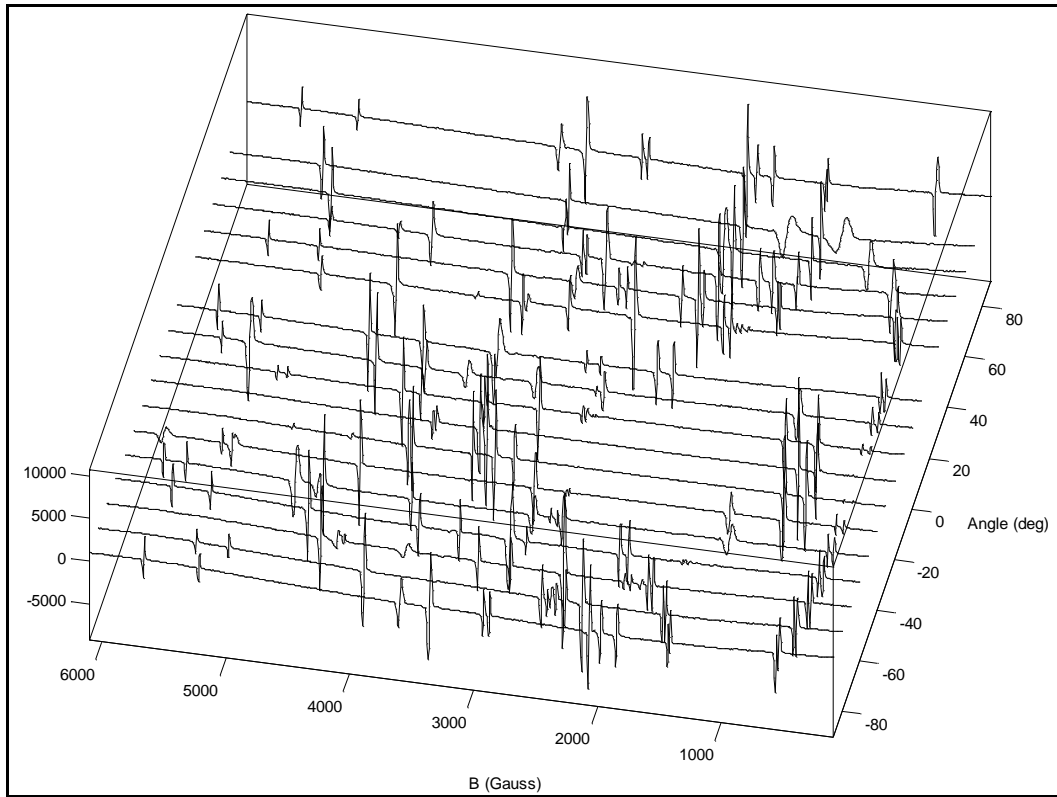


Figure 20. Wide field scans of sapphire substrate materials at approximately 30K. Marked angular anisotropy is evident in this series of scans.

Post-irradiation sapphire samples showed no additional signals at electron fluences up to  $10^{17} \text{e}^-/\text{cm}^2$ . Sapphire spectra ceased to be an experimental interferent after initial cooling problems were addressed by the tube modifications discussed earlier. Sapphire spectra are recorded here as a reference for future investigations.

## ***MBE GaN on Sapphire Substrate Results***

### **Pre-Irradiation EPR Spectroscopy**

Pre-irradiation characterization of the initial high carrier density samples conducted at AFRL/ML yielded signals that were attributable only to the sapphire substrate materials. Carrier concentrations in the samples initially procured and evaluated from May 2002 through October 2002 were greater than  $1 \times 10^{18} \text{cm}^{-3}$ , which was determined later [74] to be too high for measurement of the shallow donor signal. At carrier concentrations above  $1 \times 10^{18} \text{cm}^{-3}$ , the shallow donor signal is degraded, presumably due to screening of the donor sites by the onset of degeneracy [75] and the resultant temperature independent carrier concentrations. Samples A342, A363, A346, A350 and A351 were obtained to address this issue, all of which have room temperature carrier concentrations at or below  $1 \times 10^{18} \text{cm}^{-3}$ .

Pre-irradiation EPR characterization of samples A342-1, SB0009B-1, KD40296, and A350-1 was performed in February 2003 at the NRL/DC EPR spectrometer laboratory. Prior to irradiation, EPR signals were determined to occur at approximately  $g=1.95$  (anisotropic) and  $g=2.007$  (isotropic) in both GaN/sapphire samples and in free-standing GaN in quartz sample tubes. Signal magnitude and width were variable for the  $g=1.95$  signal (hereafter referred to as  $SD_1$ ), varying between different samples and

experimental runs. Additionally, this signal is slightly anisotropic so that the signal location and width shifted very slightly depending upon the sample's angular orientation with respect to the magnetic field vector. As discussed above, the shallow donor signal in sample A342 was very weak due to its high carrier density ( $\approx 1.2 \times 10^{18} \text{ cm}^{-3}$ ). Signal magnitude for the  $g=2.007$  (hereafter referred to as tube signal or  $\text{TO}_1$  signal) varied with experimental runs and was generally more uniform in width than the  $\text{SD}_1$  signal, in addition to being narrower. No anisotropy was noted for the  $\text{TO}_1$  signal in any of the cases examined. Representative baseline measurements for all samples examined are presented in figures Figure 30 through Figure 35, along with the corresponding post-irradiation measurements.

The constant  $g$ -value of the  $\text{TO}_1$  signal (within the limitations of microwave frequency uncertainties and errors) and the relatively consistent signal peak width were, when considered along with the almost universal presence of this signal, strong indicators that this signal was due to a background source rather than a component of the samples under examination. The assumption that this signal originated in the sample tubes used to mount the samples was easily verified by measurement of the signal in a "tube-only" spectrum. The consistency of the  $\text{TO}_1$  signal and its parameters make it ideal for use in normalizing various spectral signals for comparative analysis. A representative spectrum of this tube signal is shown in Figure 21.

The signal occurring at  $g=1.95$  is identified in the literature as a signal arising from shallow (effective mass-like) donors in GaN [33] due to band-structure considerations. The  $\text{SD}_1$  signal was found to exist in Si doped samples of GaN on sapphire substrates as well as in nominally undoped freestanding GaN layers. The signal



resonance locations were not appreciably different in the intentionally Si doped and nominally undoped samples.

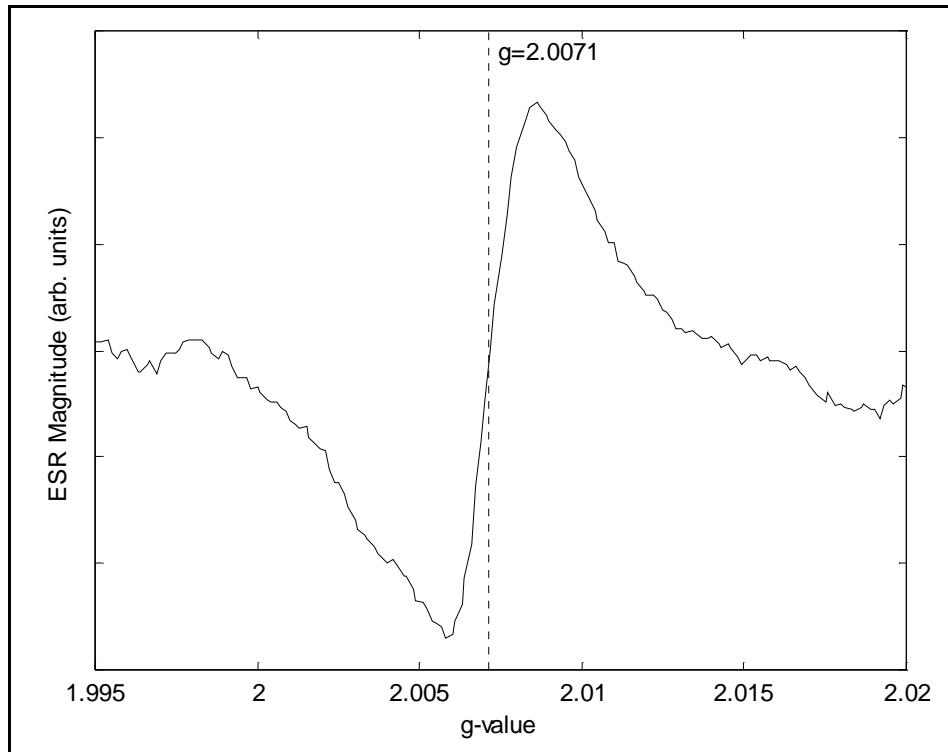


Figure 21. Representative EPR scan of the signal originating in quartz sample tube (tube #2). The resultant signal is isotropic and not easily saturated. This spectrum was obtained at approximately 4K.

Baseline (virgin) EPR measurements were performed on the remainder of the samples (A346, A363, A350, A351, and A342) during March and April 2003 at NRL/DC. These measurements were consistent with the previous set, showing the  $SD_1$  signal and  $TO_1$  signal in all samples examined. The magnitude of the  $SD_1$  signal was variable across samples in all of these measurements after scaling to the  $TO_1$  signal magnitude. The majority of these measurements were performed using the same sample tube (referred to as tube #2), which allows consistent scaling. Samples measured using

different sample tubes are found to not scale consistently, but scale factors were not recorded for other sample tubes. Control subsections of most samples were EPR baselined in this timeframe for comparison with the irradiated sample subsections.

### **Post-Irradiation EPR Spectroscopy**

After irradiation (initially at 1.6 MeV,  $10^{17}$  electrons/cm<sup>2</sup>), EPR spectrometry was again performed on the initial samples to determine if any new EPR spectral lines had been induced in the material by the irradiation. Irradiations of the initial batch of GaN samples ( $n \geq 10^{18} e^- / cm^2$ ) were conducted during the last week of September 2002. The appearance of several large sapphire signals is indicative of thermal insulation of the samples in these early measurements. Results from these irradiations showed a strong signal imparted at approximately  $g=2.0025$  that was not present in any of the pre-irradiation spectra. These signals are shown in Figure 22 as a function of the angle from the instrument's magnetic field vector to the sample substrate plane. The stability of the signal under rotation with respect to (WRT) the magnetic field immediately distinguishes it from the native sapphire signals, which display an extreme anisotropy under rotation.

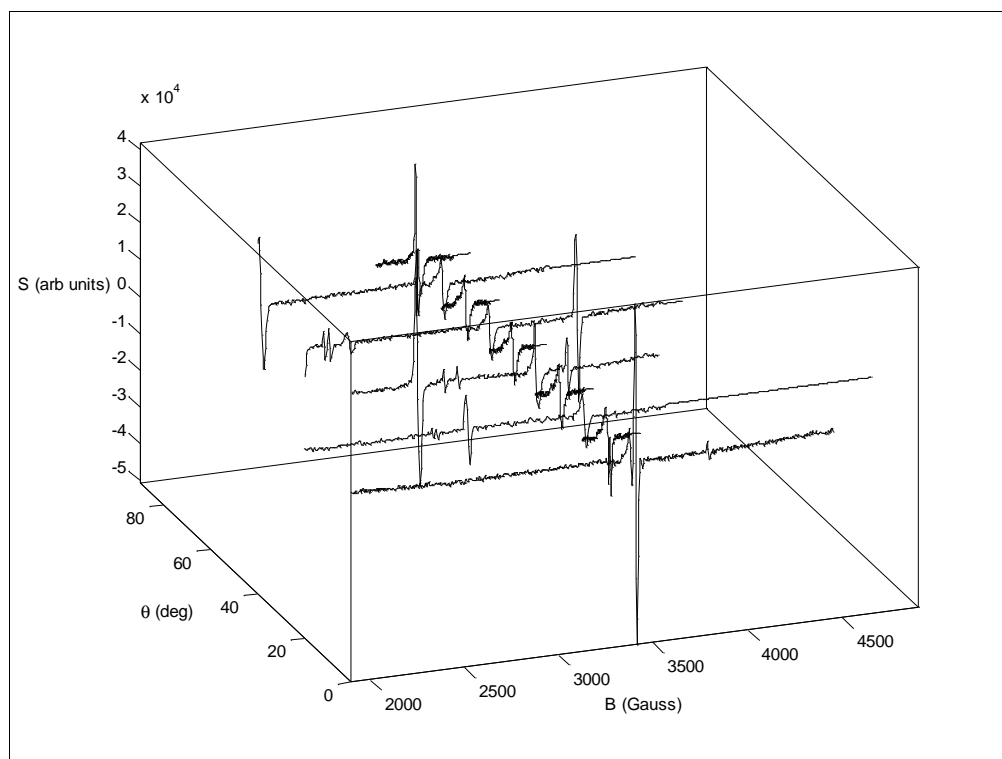


Figure 22. Spectra from irradiated GaN on sapphire (9-30-02). Spectra are shown for various angles ( $\theta$ ) with respect to the instrument magnetic field.

Initially, these signals were thought to be defects induced in the GaN layer from irradiation, an assignment bolstered by their resemblance to the native  $SD_1$  signal and the absence of any corresponding signals in both the baseline (pre-irradiation) measurements and measurement of sapphire substrates irradiated simultaneously with the GaN samples. The signal (shown in Figure 23) persisted after a thorough cleansing of the sample with acetone to remove external traces of the vacuum grease used to mount the sample during irradiation.

Measurement of the temperature dependence of the signal showed that the signal persisted even up to near room temperature with only minor changes in the signal magnitude. This finding is incompatible with a signal resulting from radiation induced

defect sites in the GaN layer, due to the absence of phonon mediated lattice interactions which reduce the state lifetimes and lead to signal saturation as temperature is increased [76]. The signal was found to be isotropic with respect to rotation in the magnetic field to within the experimental uncertainty. This was also inconsistent with the expected spectrum of a defect associated with the GaN lattice, where some anisotropy should be noted due to interactions with the Wurtzite structure lattice [77].

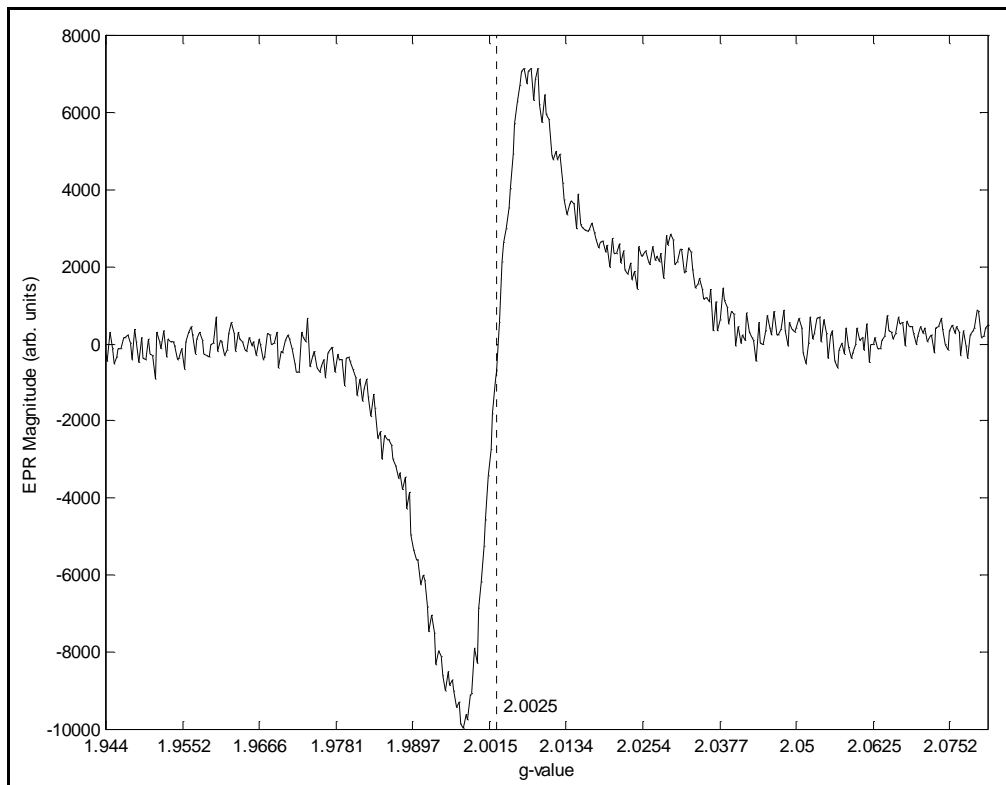


Figure 23. EPR absorption signal imparted to GaN/sapphire signals after irradiation (9-30-02). This figure shows the non-symmetric form of the signal, with a slight hump on the high-g side of the signal, and a deeper low-g side, characteristic of multiple overlapping absorption signals.

In light of these discrepancies, further investigations were conducted, including the irradiation of sapphire substrates and the vacuum grease used to mount the samples

during irradiation. These irradiations were performed during the first week of October, 2002.

Investigation of the irradiated vacuum grease and sapphire substrates indicated that vacuum grease irradiated without the benefit of shielding by the substrate material tends to crystallize. This crystallization was found to be present on all of the GaN and sapphire samples irradiated during the study; however, the crystallization was slightly more prevalent on the GaN sample examined than on the sapphire samples. After cleansing with acetone to remove the crystallization, a discoloration of the GaN sample underneath the location of the crystallized grease was noted; this was not found on the sapphire samples. Spectra from samples of vacuum grease that had been irradiated to the same levels as the targets of interest were obtained and compared to the data of Figure 23.

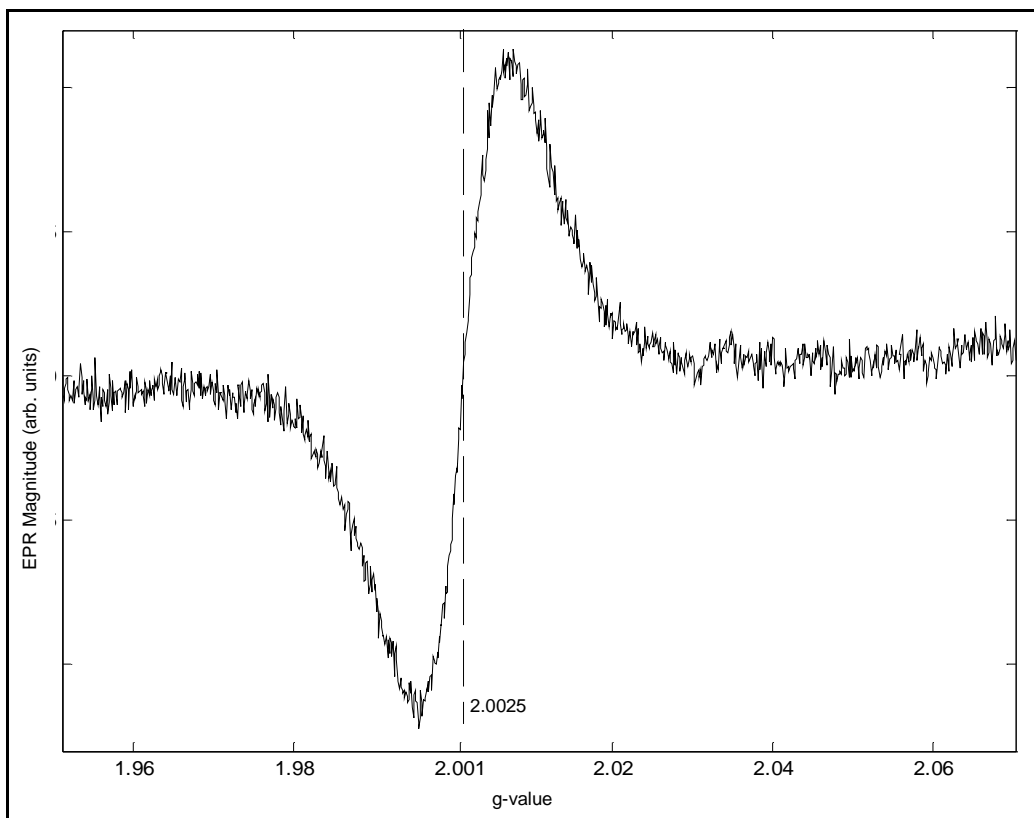


Figure 24. EPR spectrum of crystallized vacuum grease after irradiation. The signal shown here is identical to that identified in earlier GaN samples (see Figure 23)

It is clear from the data of Figure 24 that the signal of interest in Figure 23 is due to the irradiated vacuum grease. Apiezon Type N vacuum grease was chosen for its lack of paramagnetic signals, and is well known as an EPR-suitable mounting and sealing choice in the EPR spectroscopy community. There is no previous record or publication of the signals that arise from this material subsequent to electron irradiation.

Upon recognition of the nature of the irradiated vacuum grease signal, experimental methods were adjusted to obviate the requirement for grease-based

mounting and mechanical methods were developed, as discussed previously in the Experimental Procedures section.

After subtraction of the vacuum grease absorption spectra, no signals were noted in the initially irradiated samples. In these initial measurements, neither the shallow donor signal nor any signals originating from the irradiation were noted. Changes in samples and experimental procedures were prompted due to the lack of spectral features, including:

- low temperature (77K – 100K) irradiation and storage,
- acquisition of samples with lower carrier concentration [78], and
- modification of sample tubes to allow better coolant flow.

None of the new, lower dopant density, samples had measured carrier concentrations above  $5 \times 10^{17} \text{ e}^-/\text{cm}^2$ , with the exception of A342. Measurements of the new samples were conducted starting in February 2003 at NRL/DC due to the failure of the LHe transfer line on the AFRL/ML spectrometer's cryostat and resultant loss of cooling capability. Measurement of the EPR spectra of these new samples yielded the expected results discussed in the previous section, Pre-Irradiation EPR Spectroscopy.

Following preparation of the lower carrier concentration samples, irradiations were performed to approximately  $1 \times 10^{16} \text{ e}^-/\text{cm}^2$  at 1.0 MeV on the previously EPR characterized sample A342-1 on 10-11 March 2003 at the WSU VDG Facility. The sample was kept cooled during irradiation (however, no sample temperature measurements are available) and were stored in an LN2 bath until EPR measurements were performed on 13-14 March 2003. The coolant flow rate for this irradiation is questionable, and it is possible that the sample was not maintained at cryogenic

temperatures for the duration of the irradiation run. No temperature profiles for these irradiations are available. These March 2003 post-irradiation EPR measurements were performed at NRL/DC.

EPR measurements on the irradiated material, when compared to previous measurements on the identical sample subsections, were inconclusive regarding a change in the magnitude of the shallow donor signal. Comparison to un-irradiated control sample subsections of the same sample showed no discernable change in the magnitude of the shallow donor signal, nor was any change in the pre- and post-irradiation EPR spectra of single sample subsections noted.

Comparisons between irradiated sample subsections and the corresponding virgin control sample subsections are shown in Figure 25. The data shown in Figure 25 display several unusual characteristics: spurious out of phase signals, large baseline shifts, and widely varying linewidths and lineshapes in the  $SD_1$  and  $TO_1$  spectral lines. Problems with phase-locking in the lock-in amplifier are suspected for these features. After scaling by the appropriate  $TO_1$  signal magnitudes the  $SD_1$  signal magnitudes of the scans in the irradiated sample are found to vary by up to 86%. A similar analysis in the virgin sample exhibits a 93% change in the  $SD_1$  measurements. These results indicate that the spectra recorded are inconsistent and should not be used for comparative analyses.



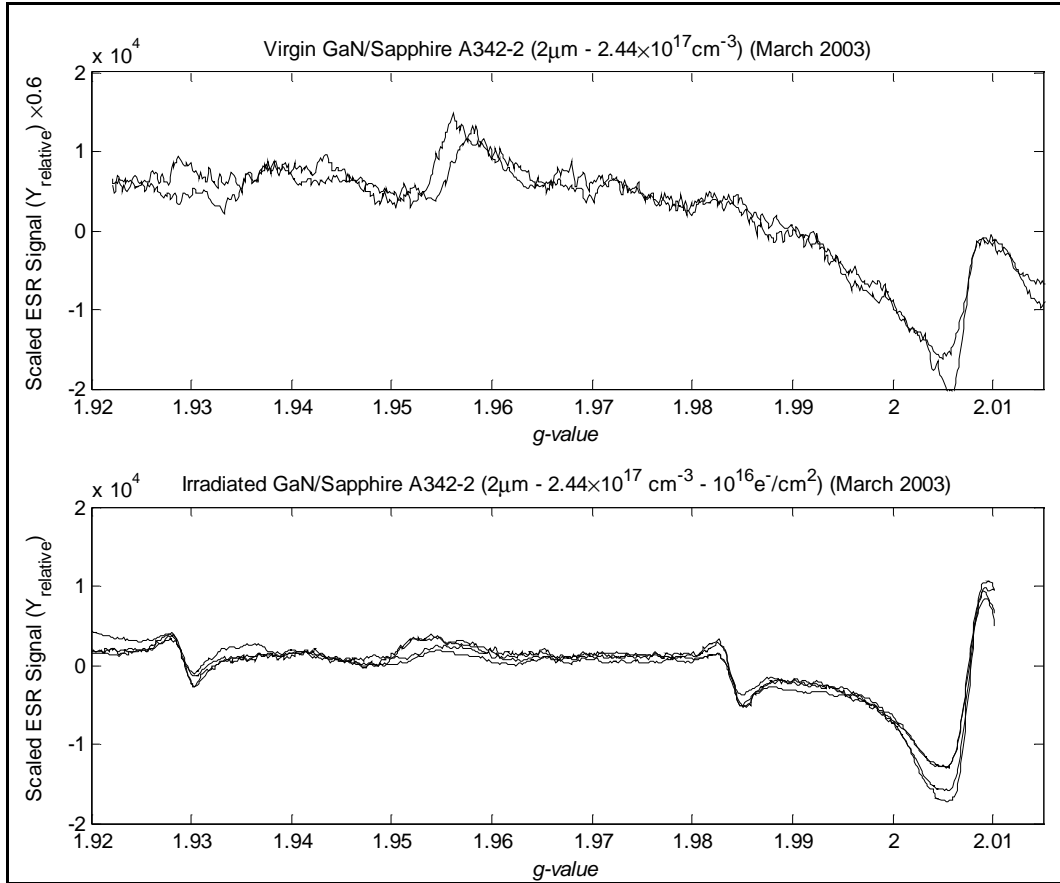


Figure 25. Comparison of virgin and irradiated ( $\phi = 10^{16} e^- / cm^2$ ) GaN on sapphire (Sample Aa342-1/2). Measurements were conducted on the same day. Note that the data of the lower plot display spurious signals (at  $g=1.93$  and  $g=1.985$ ) as well as differences in TO<sub>1</sub> linewidths and lineshapes. Magnetic field angles of 0° to 90° are shown in each plot.

Irradiations of samples A342, A350 and A351 were performed on April 11<sup>th</sup>, 2003 at a fluence level of approximately  $1 \times 10^{17} e^- / cm^2$  and an electron energy of 1.0 MeV. The irradiations were conducted with an improved stage design to allow better coolant flow; additionally, the sample stage temperature was monitored. Temperature excursions from the desired cryogenic levels were limited to disassembly and handling times. Temperature and beam current profiles for this irradiation are shown in Figure 26.

Samples were maintained at LN2 temperatures during storage and transit, while EPR measurements were conducted at NRL/DC on 14 and 15 April 2003.

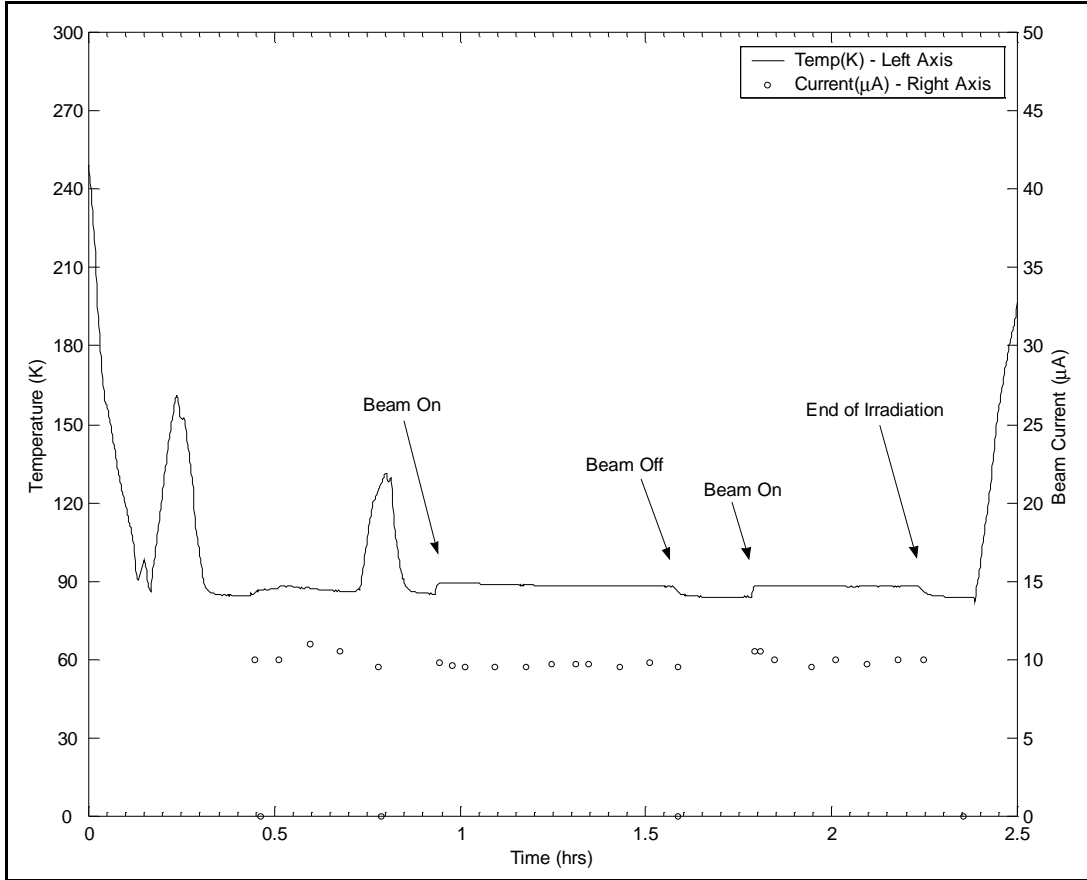


Figure 26. Temperature and beam current profile for 11 April 2003 Irradiation ( $\phi \approx 1 \times 10^{17} e^- / cm^2$ ). Temperature scale is on the left axis, beam current scale is on the right axis. Temperature spike at 0.75 hours is due to loss of chamber vacuum.

The pre- and post-irradiation measurements, as well as the irradiated sample comparisons to virgin control samples were inconclusive in that no change in the signal magnitude could be supported by the data provided. The single sample exhibiting variation in the  $SD_1$  magnitude was A351-1, in which case the  $SD_1$  may have decreased by

approximately 5-10%; however, the uncertainty in these measurements is such that no *conclusive* results could be determined. Comparisons of the pre- and post-irradiation EPR measurements for these samples are shown in Figure 27 and Figure 28. The data from sample A342 are once again plagued with large baseline fluctuations and noise; the percentage change from the lowest to highest magnitude  $SD_1$  peaks in the irradiated sample is 91%. When the  $SD_1$  signal in the irradiated material is averaged over available scans the magnitude is  $1.97 \pm 1.41$ , demonstrating extreme measurement fluctuation.

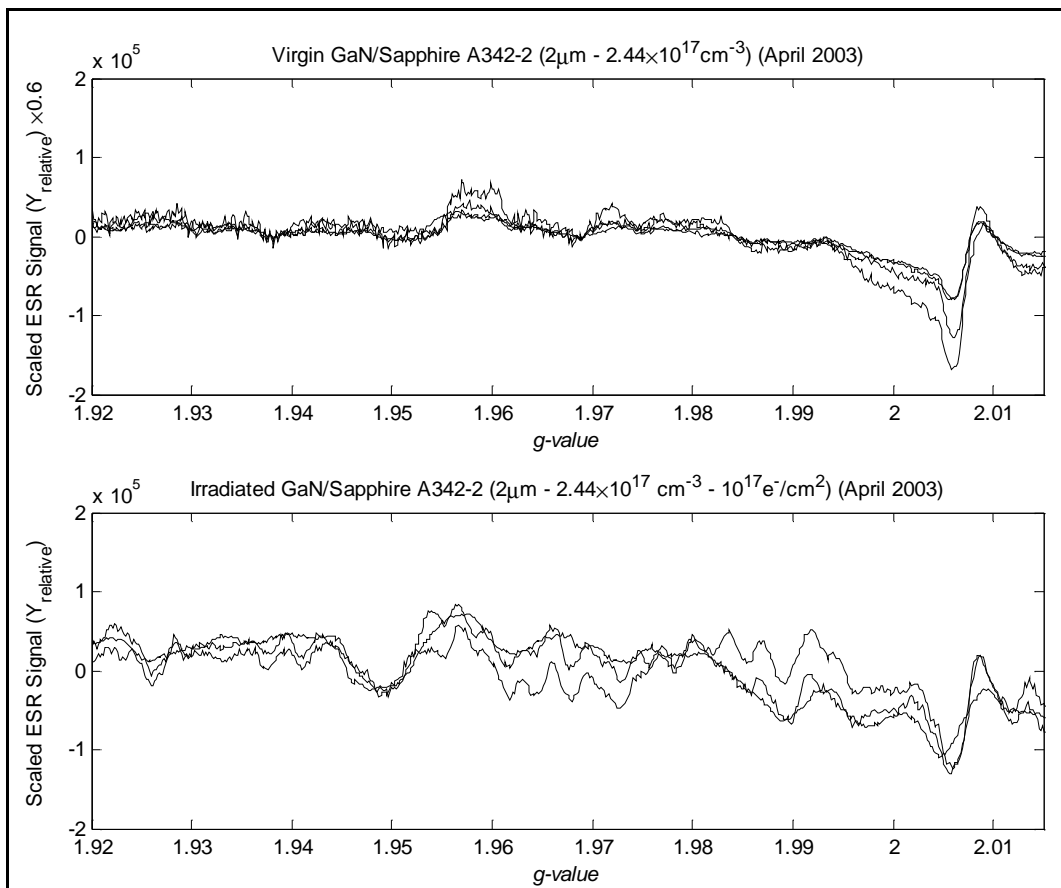


Figure 27. Comparison of virgin and irradiated ( $\phi \approx 10^{17} e^- / cm^2$ ) GaN on Sapphire (Sample A342). Measurements conducted under identical conditions, same day. Magnetic field angles of  $0^\circ$  to  $90^\circ$  are shown in each plot.

The A342 virgin data average to  $1.10 \pm 0.20$  over the displayed scans. These data are considered too unreliable to use in comparative analyses. Sample A351, shown in Figure 28, is considered a better estimate of the relative changes due to irradiation at these fluences.

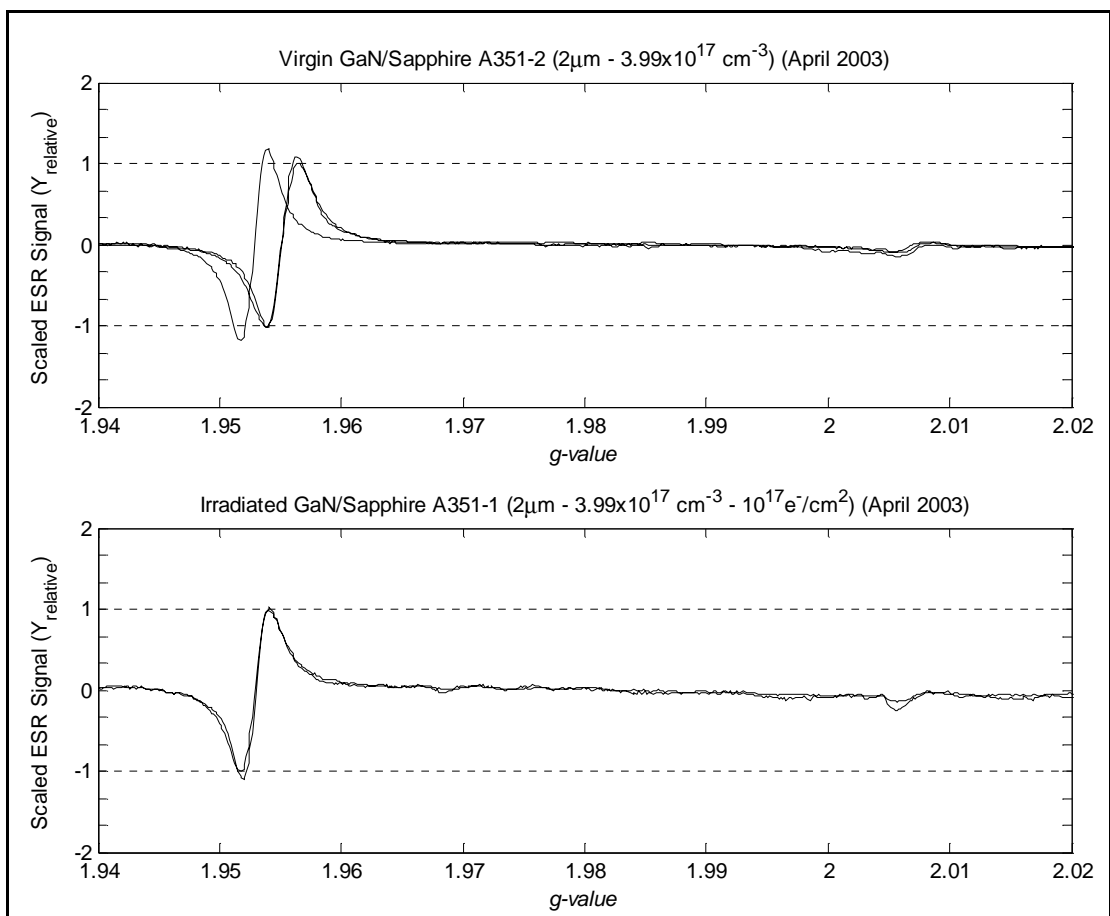


Figure 28. Comparison of virgin and irradiated ( $\phi \approx 10^{17} e^- / cm^2$ ) GaN on Sapphire (Sample A351). Measurements conducted under identical conditions, same day. Variation in the  $g=1.95$  signal location is due to rotational anisotropy. Experimental difficulties resulted in collection of only two good spectra in the irradiated sample. Magnetic field angles of  $0^\circ$  to  $90^\circ$  are shown in each plot. Angular measurements in this sample were only available at  $0^\circ$  and  $90^\circ$ .

The data of Figure 28 are less comprehensive than in later experiments due to experimental difficulties in acquiring good sample data with a well resolved  $TO_1$  signal for comparison. As a result only two high-quality spectra were obtained for the irradiated A351-1 sample, both in the  $\vec{B} \perp \vec{c}$  ( $0^\circ$ ) orientation. Similar difficulties were encountered in obtaining spectra for the virgin material, where two good spectra were measured at  $90^\circ$  and one good spectrum at  $0^\circ$ .

The irradiation fluence that the samples were exposed to ( $1 \times 10^{17} \text{ e}^-/\text{cm}^2$ ) is expected to be at the lower threshold of detectability from previous work and theoretical determinations, given an assumed defect introduction rate of  $0.1\text{-}0.3 \text{ cm}^{-1}$  [79]. The null result prompted the decision to perform another irradiation at a higher fluence level (approximately  $1 \times 10^{18} \text{ e}^-/\text{cm}^2$  at 1.0 MeV) which occurred on 12 May 2003. This irradiation run was monitored for sample stage temperature throughout the course of the run, and the samples were held in an LN2 bath during storage and transit, as well as holding all irradiated and control samples in dark containers. Temperature and beam current profiles for the irradiation of 12 May 2003 are shown in Figure 29.

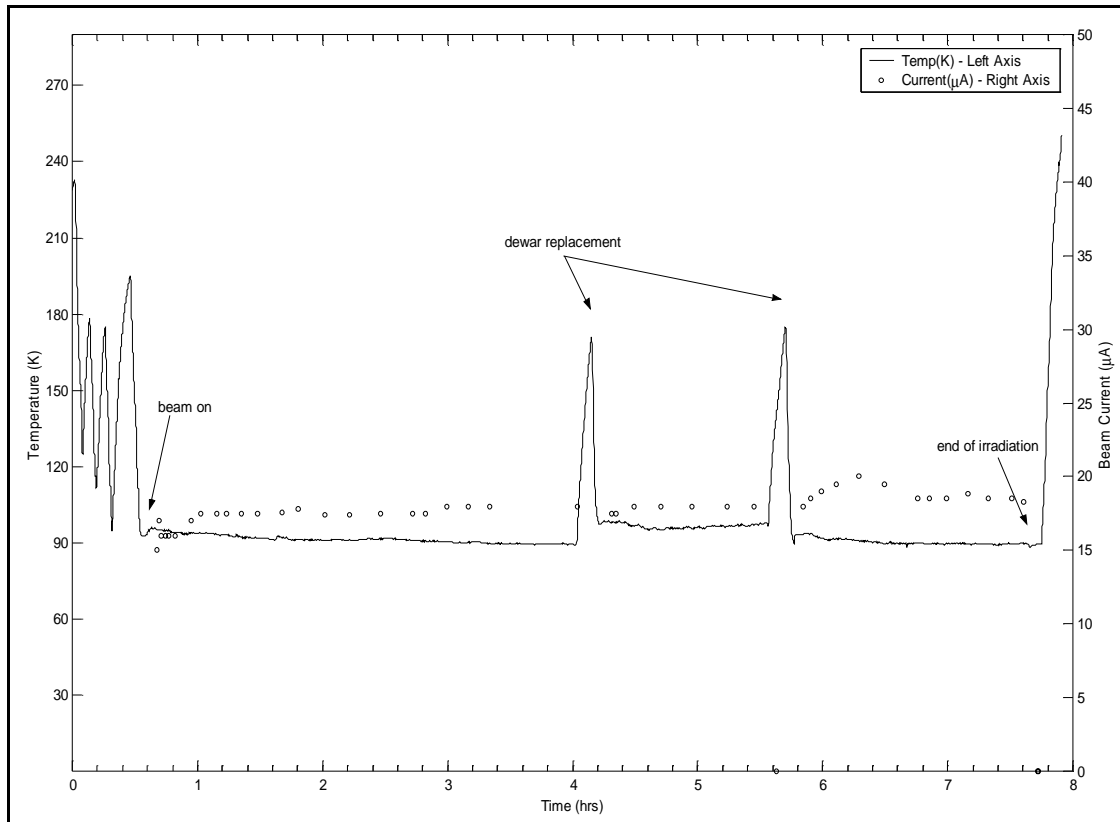


Figure 29. Temperature and beam current profile for 12 May 2003 Irradiation ( $\phi \approx 1 \times 10^{18} e^- / cm^2$ ). Temperature scale is the left axis, beam current scale is on the right axis.

Comparison of irradiated samples with virgin control samples for A342-1, A350-1, A351-1, and A363-1 was performed on 15 and 16 May 2003 at NRL/DC. Comparisons of the shallow donor signal magnitude (post-correction) in the irradiated and virgin samples following this irradiation showed remarkable differences. The magnitude of the shallow donor signal in every irradiated sample (for which a consistent dose had been administered) *decreased* with respect to the pre-irradiation runs or the virgin control sample magnitude. The decrease in the shallow donor signal magnitudes are demonstrated in Figure 30 through Figure 35 for GaN epilayers on sapphire substrates. Post-irradiation data for sample A342-1 is compared to its pre-irradiation

state (A342-1 virgin) as well as to a control subsection (A342-2) due to difficulties in obtaining high-quality spectra from subsection A342-2. Other samples are compared to the corresponding control subsection.

Most measurements made on irradiated or virgin samples showed reasonable uniformity after system response corrections were made. Sample measurements made at various angles to the magnetic field showed variations of 25% to 30% in the integrated signal intensity (see following figures). This variation was consistent across samples, with the larger magnitude peaks always occurring in the  $\vec{B} \perp \vec{c}$  orientation.

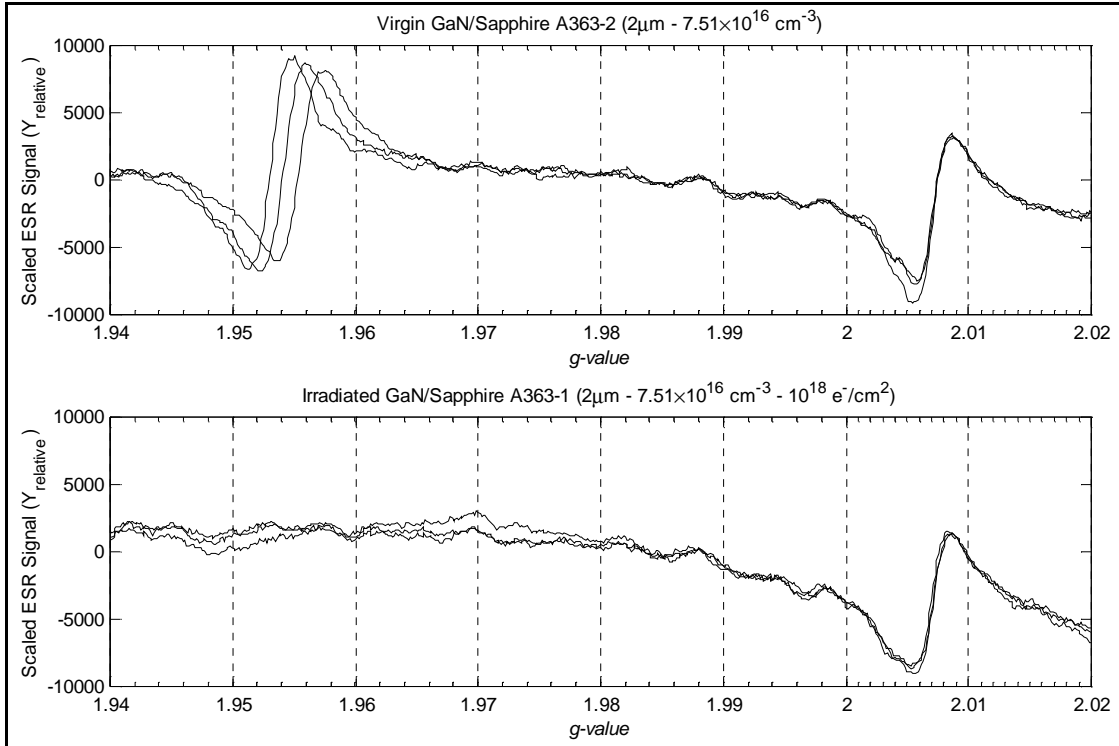


Figure 30. Comparison of virgin and irradiated ( $\phi \approx 10^{18} \text{e}^-/\text{cm}^2$ ) GaN on Sapphire (Sample A363). Measurements conducted under identical conditions, same day. Variation in the  $g=1.95$  signal location is due to rotational anisotropy. Magnetic field angles of  $0^\circ$  to  $90^\circ$  are shown in each plot.



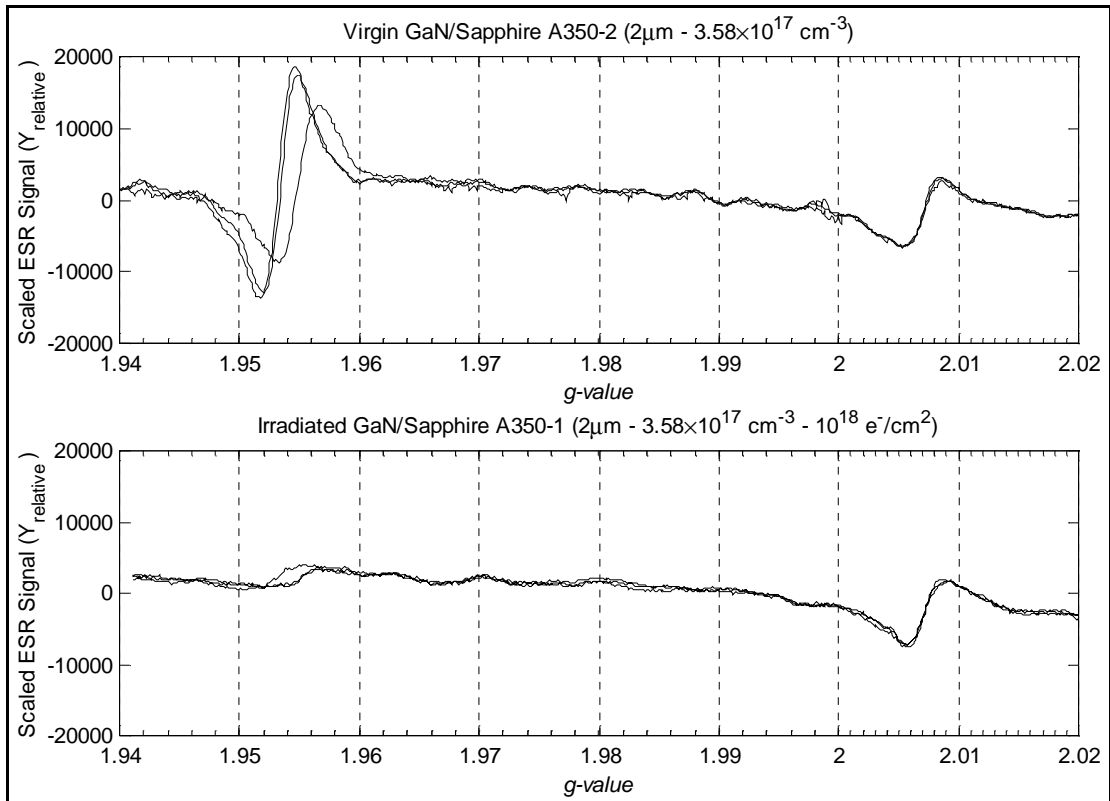


Figure 31. Comparison of virgin and irradiated ( $\phi \approx 10^{18} e^- / cm^2$ ) GaN on Sapphire (Sample A350). Measurements conducted under identical conditions, same day. Variation in the  $g=1.95$  signal location is due to rotational anisotropy. Magnetic field angles of  $0^\circ$  to  $90^\circ$  are shown in each plot.

After the initial post-irradiation measurements were made on sample A350, showing nearly complete removal of the shallow donor signal, a simple annealing experiment was conducted. The sample was allowed to sit unperturbed at room temperature (293K) for 17 hours (overnight) and was then re-measured by the spectrometer under the same conditions as for the previous day's runs. The sample showed recovery of the shallow donor signal, with a recovery of approximately 25% of the original signal magnitude, from about 12% following irradiation. This annealing is shown in Figure 32.

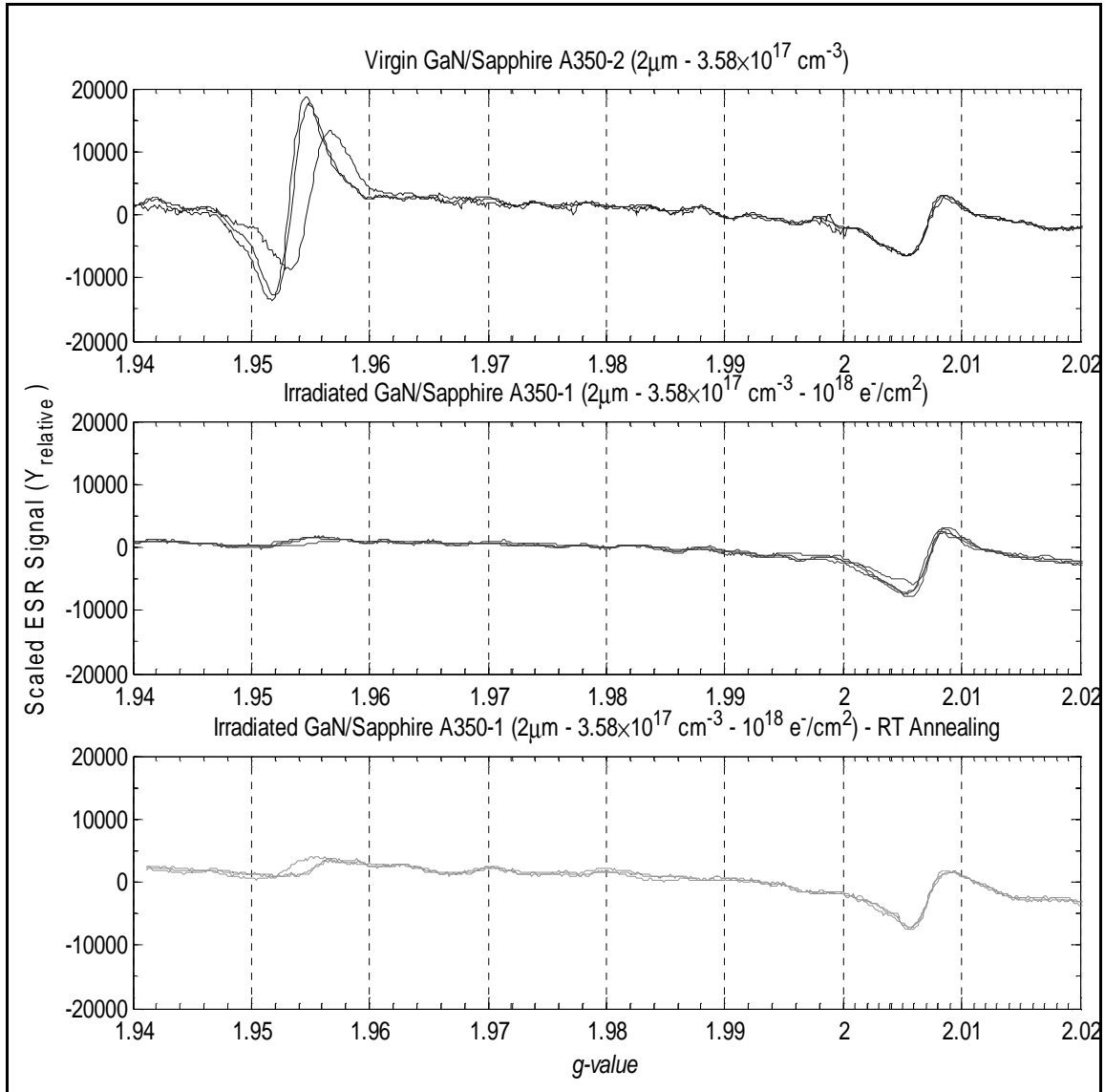


Figure 32. Comparison of A350 after 17 hours room temperature annealing with virgin and irradiated ( $\phi \approx 10^{18} \text{ e}^-/\text{cm}^2$ ) GaN on Sapphire. Variation in the  $g=1.95$  signal location is due to rotational anisotropy. The lower curve is after annealing. Magnetic field angles of  $0^\circ$  to  $90^\circ$  are shown in each plot.

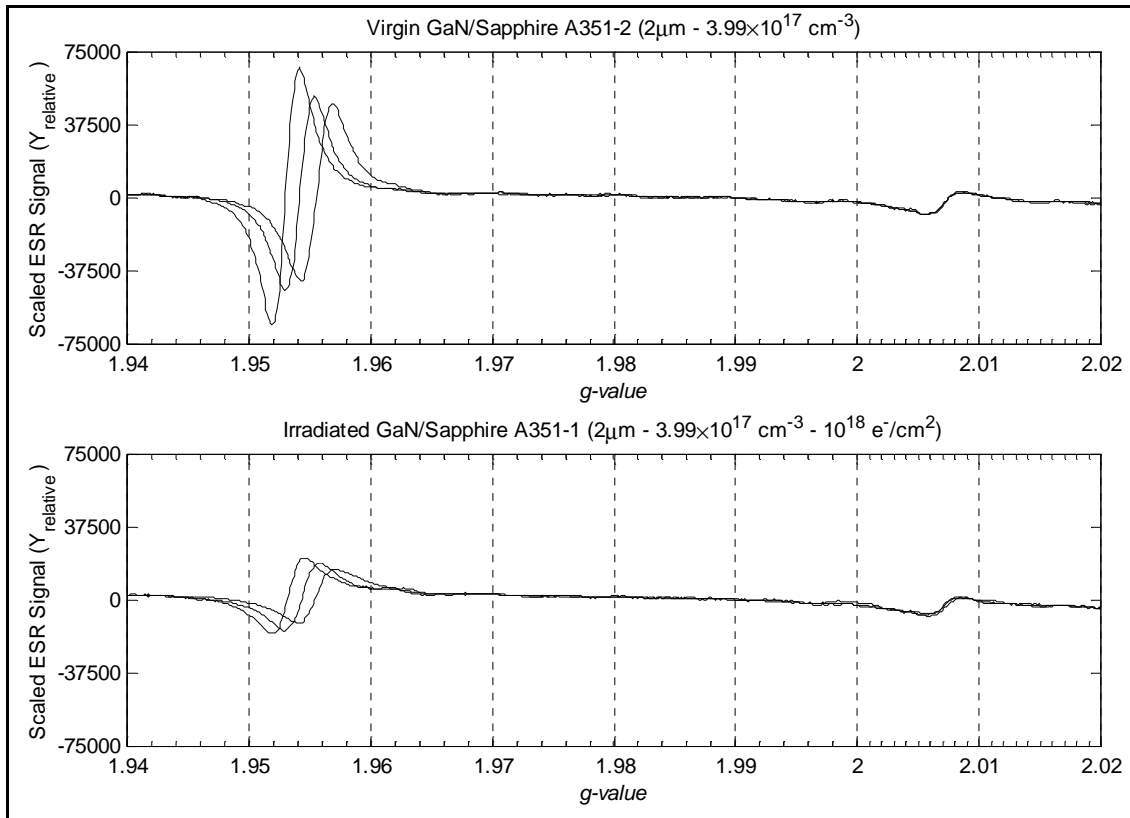


Figure 33. Comparison of virgin and irradiated ( $\phi \approx 10^{18} \text{ e}^- / \text{cm}^2$ ) GaN on Sapphire (Sample A351). Measurements conducted under identical conditions, same day. Variation in the  $g=1.95$  signal location is due to rotational anisotropy. Magnetic field angles of  $0^\circ$  to  $90^\circ$  are shown in each plot.

The number of sample subsections on the sample stage for the 12 May 2003 irradiation run was larger than for previous irradiations, due to the lengthy duration of the irradiation. While samples were placed in positions initially expected to be within the diameter of the electron beam, sample A342 was placed at the extreme outside edge of the 2 cm beam aperture. Upon examination of the EPR spectra for this sample, it was noted that sample A342 represented a deviation from the EPR signal reductions noted in the other exposed samples. This result can be explained by the partial shielding of the

sample by the beam aperture during the course of irradiation, significantly reducing the fluence on this sample from that of the more centrally located samples.

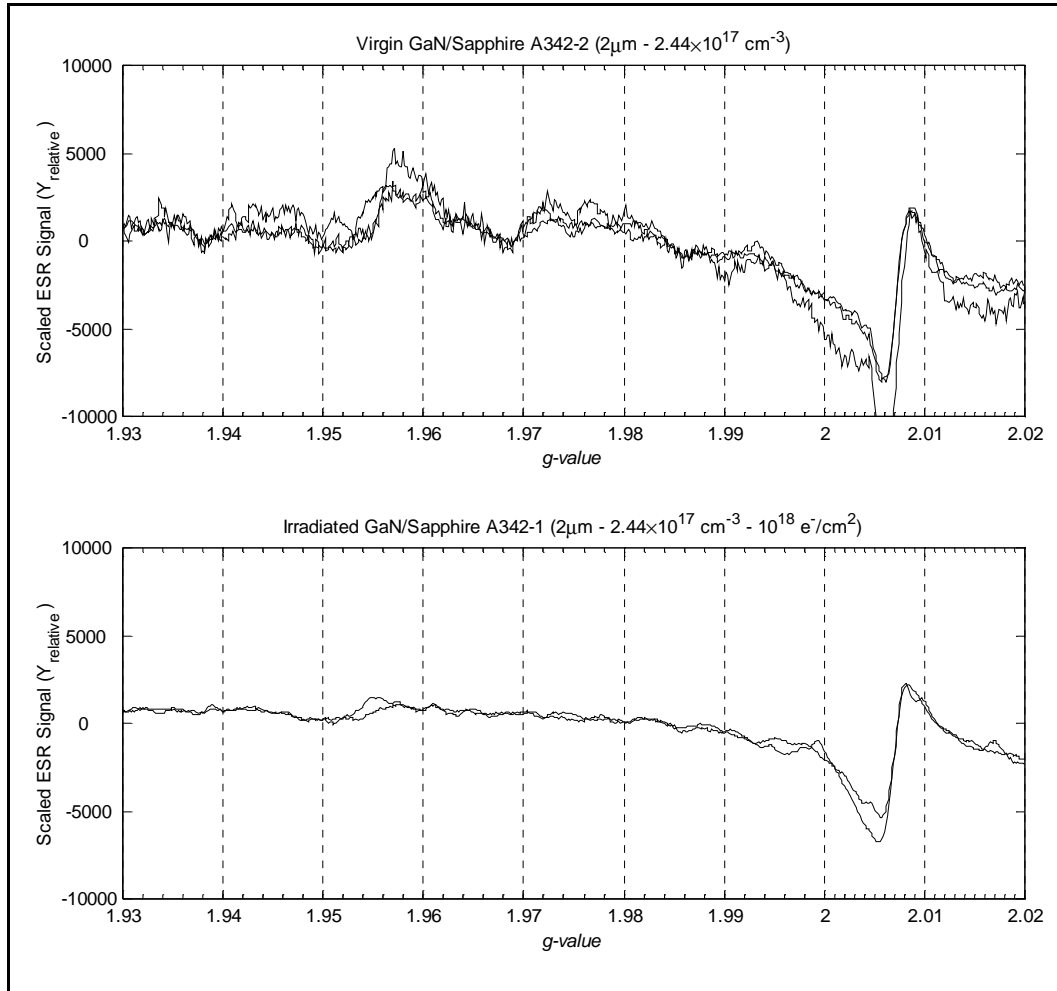


Figure 34. Comparison of virgin and irradiated ( $\phi \approx 10^{18} e^- / cm^2$ ) GaN on Sapphire (Sample A342-1/2). Measurements conducted under identical conditions, same day. Variation in the  $g=1.95$  signal location is due to rotational anisotropy. Magnetic field angles of  $0^\circ$  to  $90^\circ$  are shown in each plot.

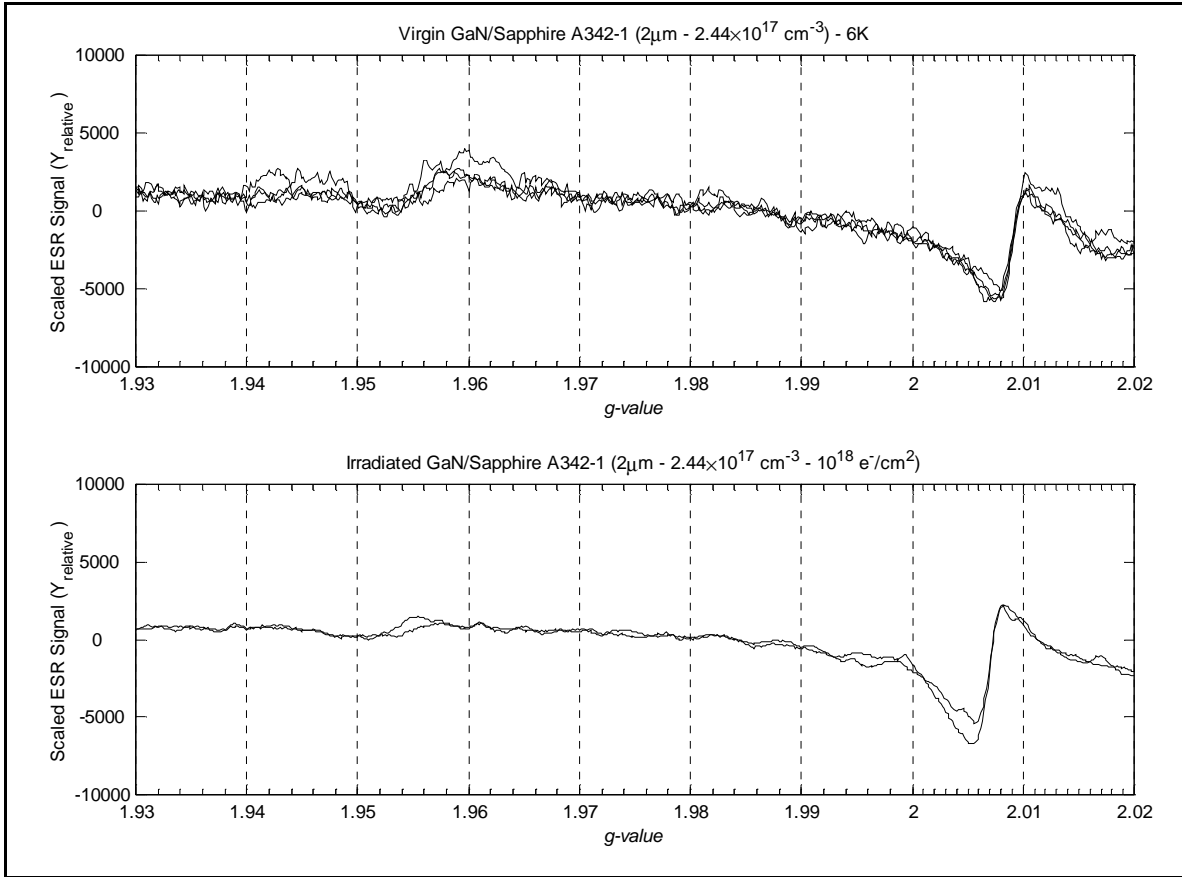


Figure 35. Comparison of virgin and irradiated ( $\phi \approx 10^{18} \text{ e}^- / \text{cm}^2$ ) GaN on Sapphire (Sample A342-1). Measurements conducted under similar experimental conditions, on identical sample subsections. Variation in the  $g=1.95$  signal location is due to rotational anisotropy. Magnetic field angles of  $0^\circ$  to  $90^\circ$  are shown in each plot.

The shallow donor signal magnitude in the post-irradiation samples was found to be a function of the signal magnitude (and thus donor/dopant density) in the virgin material. The maximum signal decrease was noted in samples A363 and SB0009B where the signal was completely removed, a decrease of approximately 88% was observed for sample A350 after scaling for differing sample volumes, and the minimum signal decrease was noted in sample A351, where the signal decreased by approximately a factor of 2. The relationship between carrier concentration (or donor density) and EPR

signal magnitude for virgin and irradiated samples is shown in Figure 36. The data of Figure 36 have not been scaled by sample volume.

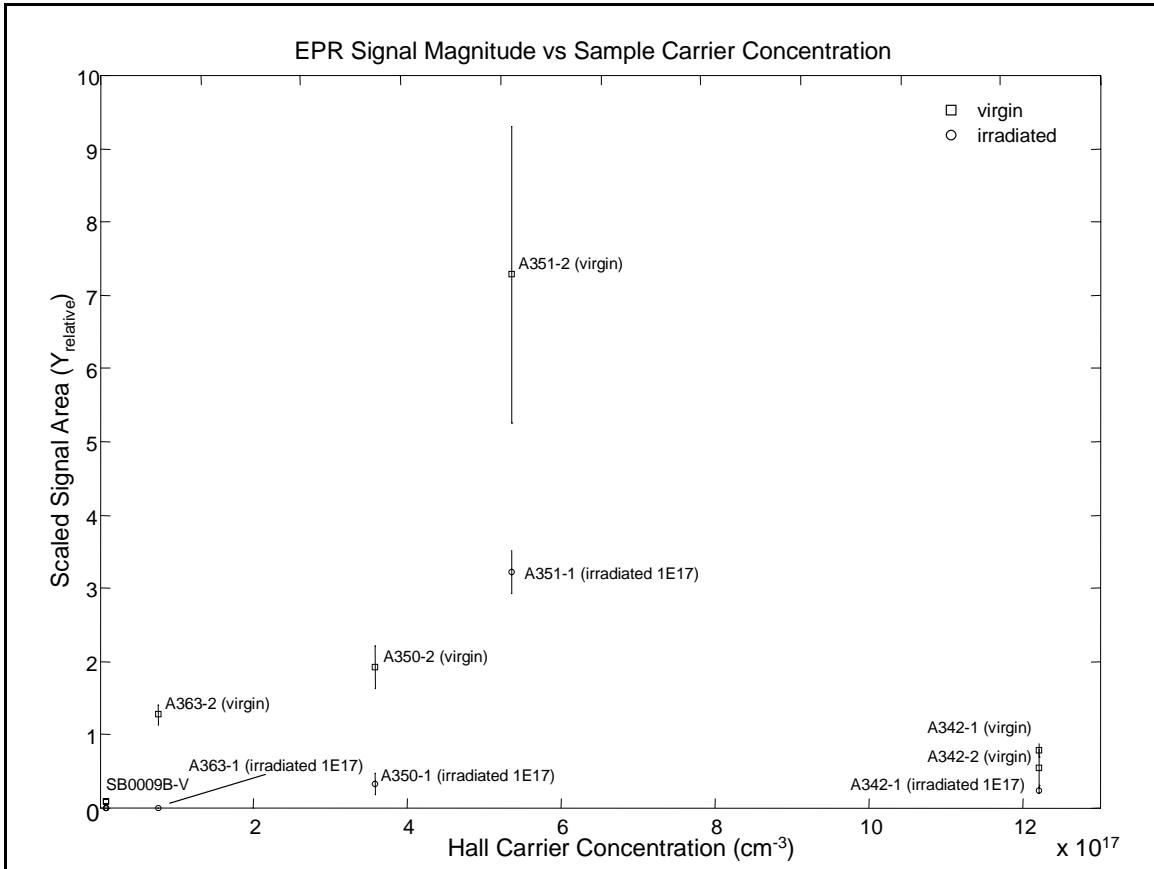


Figure 36. Comparison of scaled, integrated EPR signals (pre- and post-irradiation) versus post-growth room temperature carrier concentration as determined by Hall measurements. Note that sample A342 was probably under-dosed in this exposure. Sample SB0009B has been adjusted for the increased volume of the sample.

One wide magnetic field scan (approx 1450G-5500G) was performed on sample A363-1 after irradiation to detect any new signals that may have resulted from the irradiation. This scan is shown in Figure 37. The new signal imparted just above 4000G

was scanned repeatedly, and although it showed up in several experimental runs, was found to be relatively unstable, making measurement and analysis difficult.

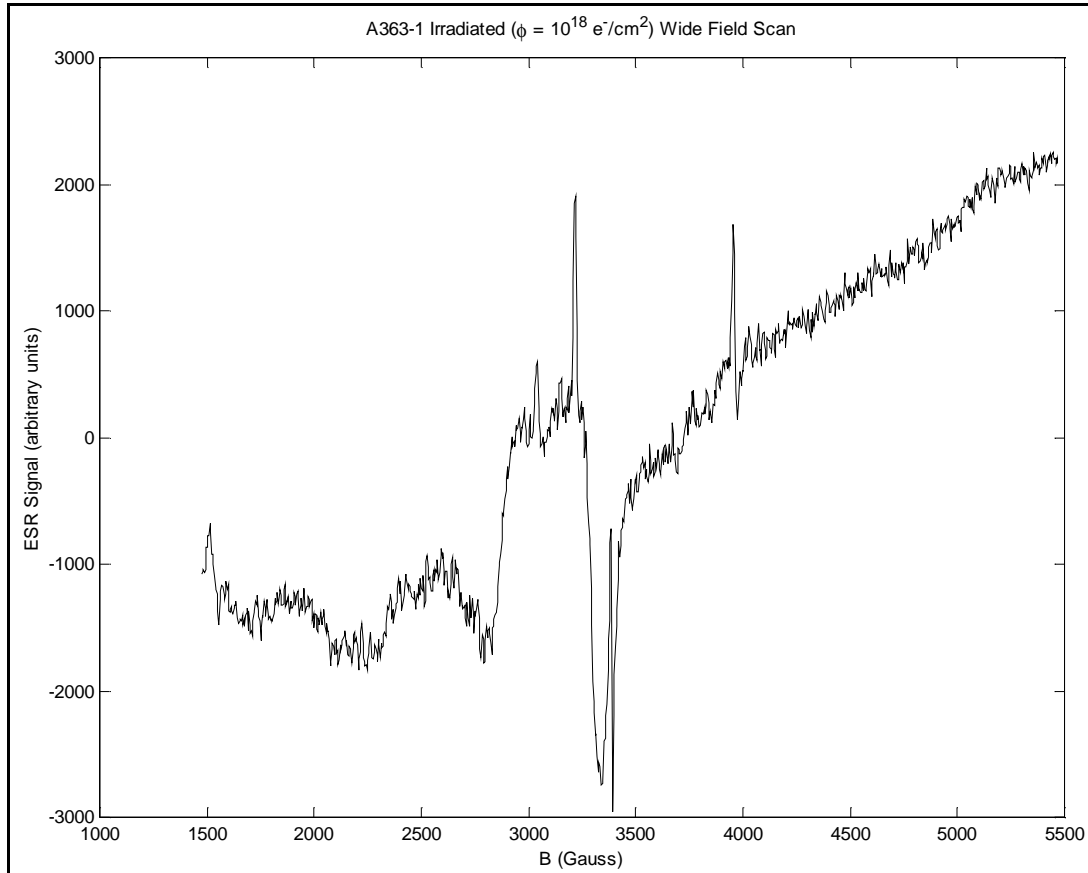


Figure 37. Wide magnetic field scan ( $\vec{B} \perp \vec{c}$ ) of sample A363-1 after irradiation ( $\phi = 10^{18} e^-/cm^2$ ). The sharp signal appearing at approximately 3400 G is the ubiquitous tube signal. Magnetic field units are used as the dependent variable due to the width of the scan.

The data of Figure 37 at first glance seems to exhibit a periodic structure, which was determined in post-measurement analysis to correspond to a hyperfine interaction with a single Ga atom, with atomic abundances of approximately 39% for  $^{69}\text{Ga}$  and 61%

for  $^{71}\text{Ga}$ . The broad spectrum of the Ga hyperfine interaction seems to be superimposed upon a second signal near 3100G that shows no resolved hyperfine structure. A sharp peak at approximately 3380G is still in apparent, and is once again attributed to the sample tube. A more complete analysis of the hyperfine structure can be found in the Analysis and Discussion section of this dissertation. This same hyperfine structure was also determined to be present in sample SB0009B (free-standing HVPE GaN) after an identical irradiation (see following section for details).

## ***Free-Standing GaN Sample Results***

### **Pre-Irradiation EPR Spectroscopy**

Sample SB0009B is a single sample (no subsectioning was possible) of relatively small size. This fact has driven much of the experimental procedure as it pertains to this particular sample. More virgin baseline spectra were taken on SB0009B than on the other samples and multiple irradiations were not performed.

Sample SB0009B-1 was characterized by EPR spectroscopy on 6 February 2003 and 14 March 2003 in its un-irradiated state. These “baseline” EPR measurements were performed in duplicate on this sample in particular due to the lack of sufficient material for a control sample. Therefore the data presented are pre-irradiation and post-irradiation comparisons on the same sample, SB0009B-1.

This sample varied in several aspects from the GaN epilayers discussed previously, it is HVPE grown rather than MBE grown and the substrate and interfacial region have been removed. The EPR spectra from this sample differed in several respects from the MBE grown epilayer samples. The  $\text{SD}_1$  signal in this material, while



retaining the same g-value and anisotropic behavior as in the MBE samples, is markedly wider in the HVPE samples. The  $SD_1$  signal here is also present at slightly higher temperatures, with the signal actually being easier to obtain at near 20K than at the 4K temperature where the MBE sample data was taken. The overall integrated intensity of the  $SD_1$  signal is found to be much greater for the HVPE samples than for the MBE; however, the greater width of the absorption signal in the HVPE material reduces the apparent magnitude of a first-derivative plot. Increased signal integrated intensity in this sample is attributed to the greater thickness of the sample, approximately 100 times that of the MBE grown epilayers.

### **Post-Irradiation EPR Spectroscopy**

The results of post-irradiation EPR measurements on SB0009B mirror those of the previously discussed MBE grown samples. The complete disappearance of the  $SD_1$  signal is noted following irradiation of  $10^{18} \text{ e}^-/\text{cm}^2$  at 1.0 MeV, with measurements performed at both 4K and 22K. This is the sole irradiation for this sample; a comparison of the pre- and post-irradiation EPR spectra appear in Figure 38 and Figure 39 for measurement temperatures of 4K and 22K respectively.

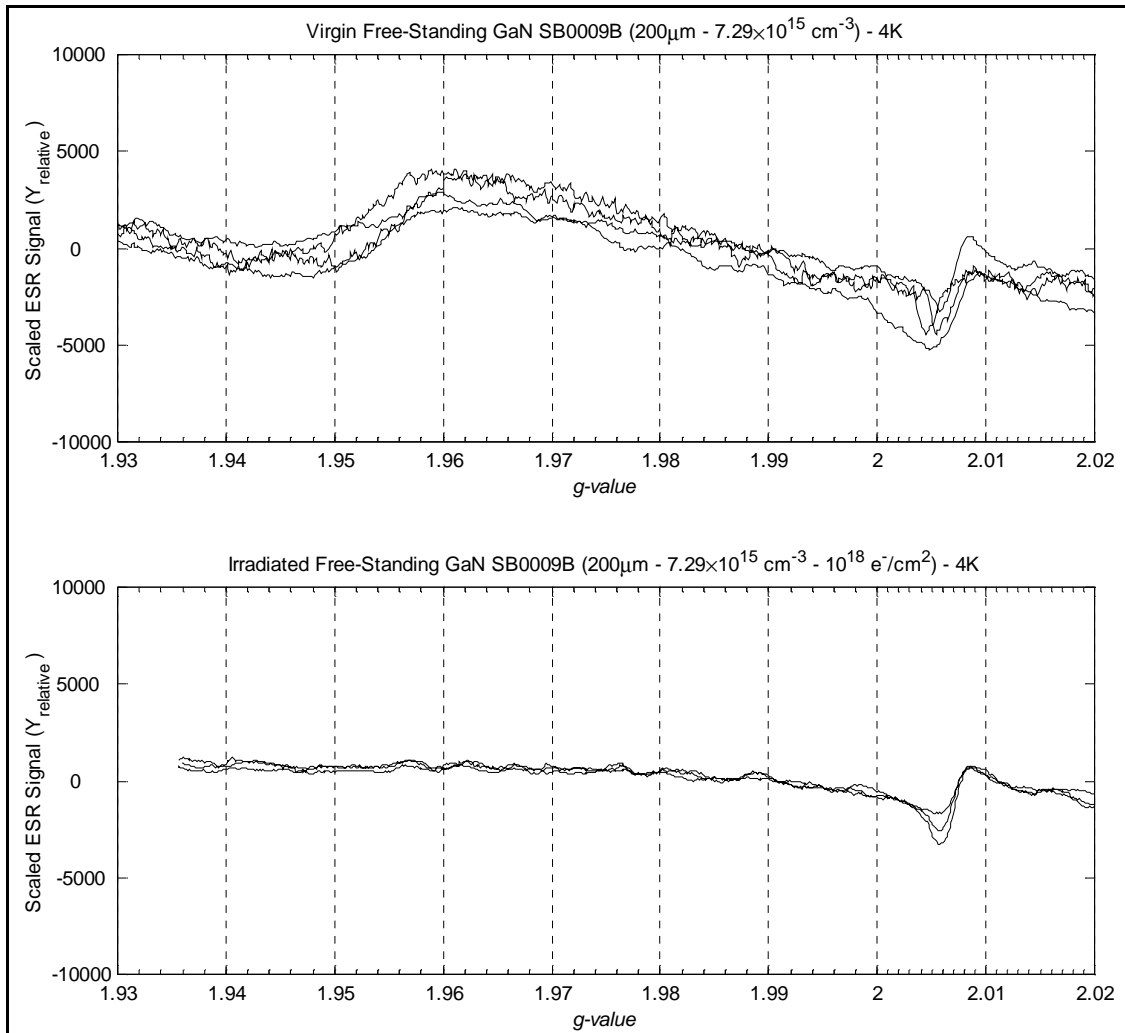


Figure 38. Comparison of virgin and irradiated ( $\phi \approx 10^{18} e^- / cm^2$ ) free-standing GaN (Sample SB0009B-1). Measurements conducted under similar experimental conditions, same sample subsection. Variation in the  $g=1.95$  signal location is due to rotational anisotropy. Measurements were conducted at 4K sample temperature.

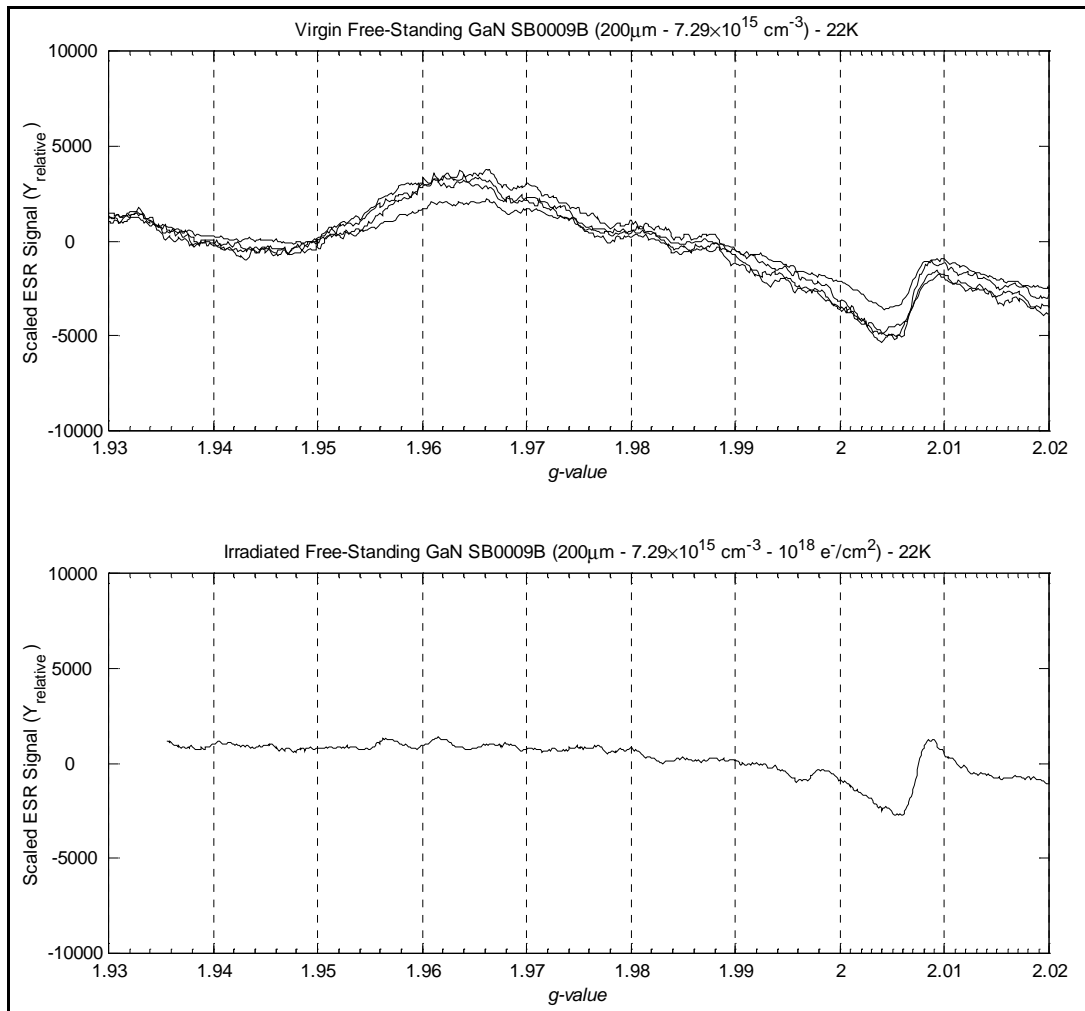


Figure 39. Comparison of virgin and irradiated ( $\phi \approx 10^{18} \text{ e}^- / \text{cm}^2$ ) free-standing GaN (Sample SB0009B-1). Measurements conducted under similar experimental conditions, same sample subsection. Variation in the  $g=1.95$  signal location is due to rotational anisotropy. Measurements were conducted at 22K sample temperature.

A wide magnetic field scan was performed on sample SB0009B-1 after irradiation to search for the appearance of signals due to the irradiation; however, baseline measurements were not performed over the entire magnetic field range scanned. The

data from this wide field scan is shown in Figure 40. A strong resemblance to the wide-field scan of sample A363-1 after irradiation (Figure 37) is immediately obvious in the data of SB009B-1. This wide-scan data and the structure displayed therein will be analyzed more fully in the Analysis and Discussion section.

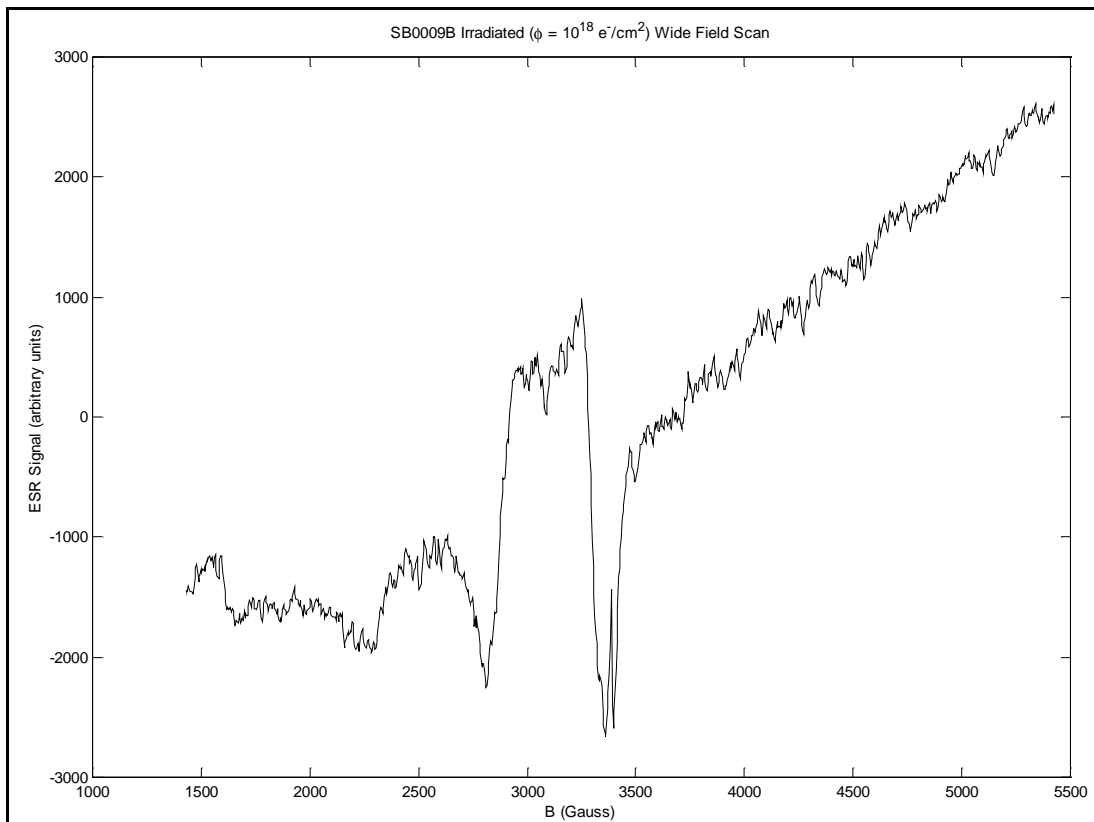


Figure 40. Wide magnetic field scan ( $\vec{B} \perp \vec{c}$ ) of sample SB0009B-11 after irradiation ( $\phi = 10^{18} e^-/cm^2$ ). The sharp signal appearing at approximately 3400 G is the ubiquitous tube signal. Magnetic field units are used as the dependent variable due to the width of the scan.

## Supporting Experimental Results

### Pre-Irradiation Hall Effect Measurements

Samples were subjected to Hall measurements previous to irradiation to determine the baseline values of carrier concentration and carrier mobility in their as-grown state. Most sample data showed some impact from the presence of a conductive interface channel which was corrected during analysis following the method of Look, et al [67]. Details of the conductive channel correction are outlined in the Theoretical Considerations section, and Hall measurement results are shown in Figure 41 and Figure 42 for virgin materials.

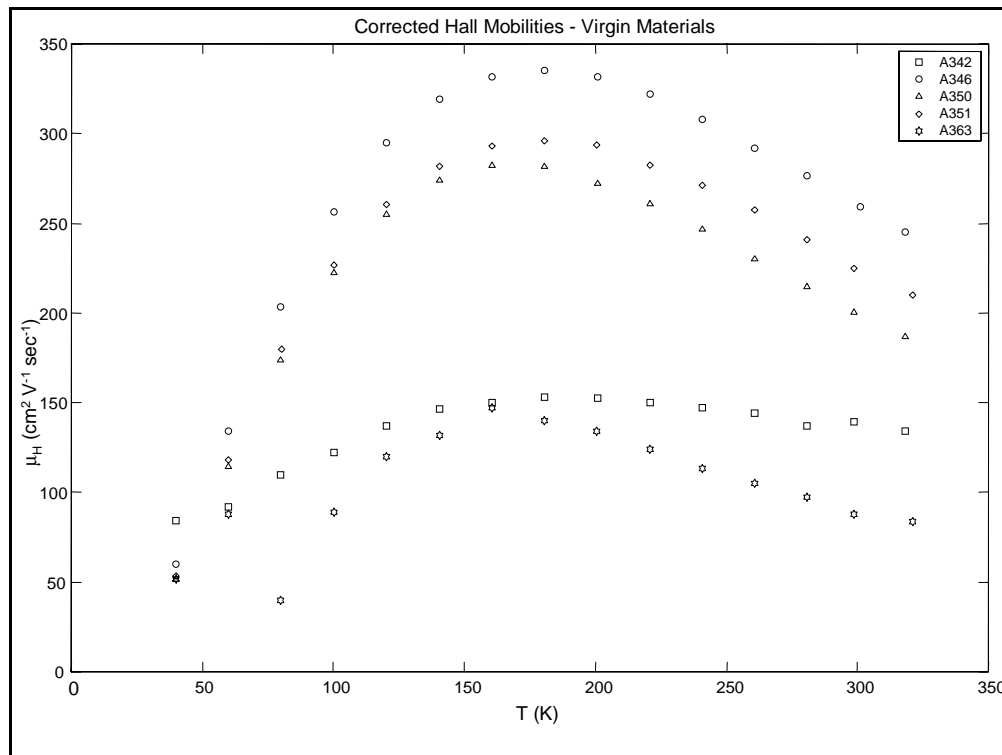


Figure 41. Corrected Hall mobilities of virgin materials used in the current study. Good Hall data was not available on SB0009B. Measurements are limited to the 30K-320K regime due to the use of 20K measurements to perform multiple-layer corrections.

The Hall mobilities of Figure 41 indicate that the MBE samples are all of intermediate quality as judged by the peak mobilities of less than  $350 \text{ cm}^2 \text{ V}^{-1} \text{ sec}^{-1}$  for all samples. All samples shown have a typical  $\mu_H(T)$  profile, peaking near 160K.

Corrected carrier concentrations of the MBE grown samples show that the range of room temperature concentrations is approximately  $8 \times 10^{16} \text{ cm}^{-3}$  up to  $7.2 \times 10^{17} \text{ cm}^{-3}$ , as is shown in Figure 42. Two donor models fitted to the measured Hall concentrations were used to determine the shallow donor densities of interest in all samples [20]. These fitted data are shown in Figure 43 through Figure 47 for virgin samples; shallow donor concentrations and activation energies determined from fitting of this data are summarized in Table 10, appearing on page 124.

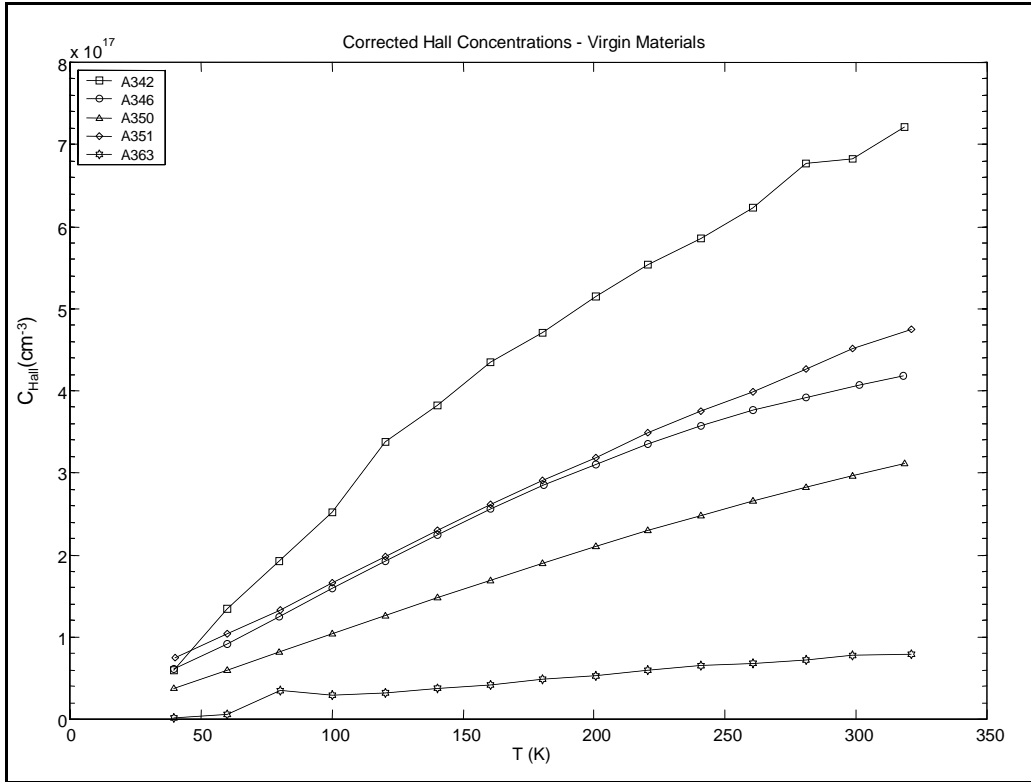


Figure 42. Multi-layer corrected Hall carrier concentrations of virgin materials used in the current study. Good Hall data was not available on SB0009B. Hall data is limited to the 30K-320K regime due to the need to use the lowest T points in the multi-layer analysis.

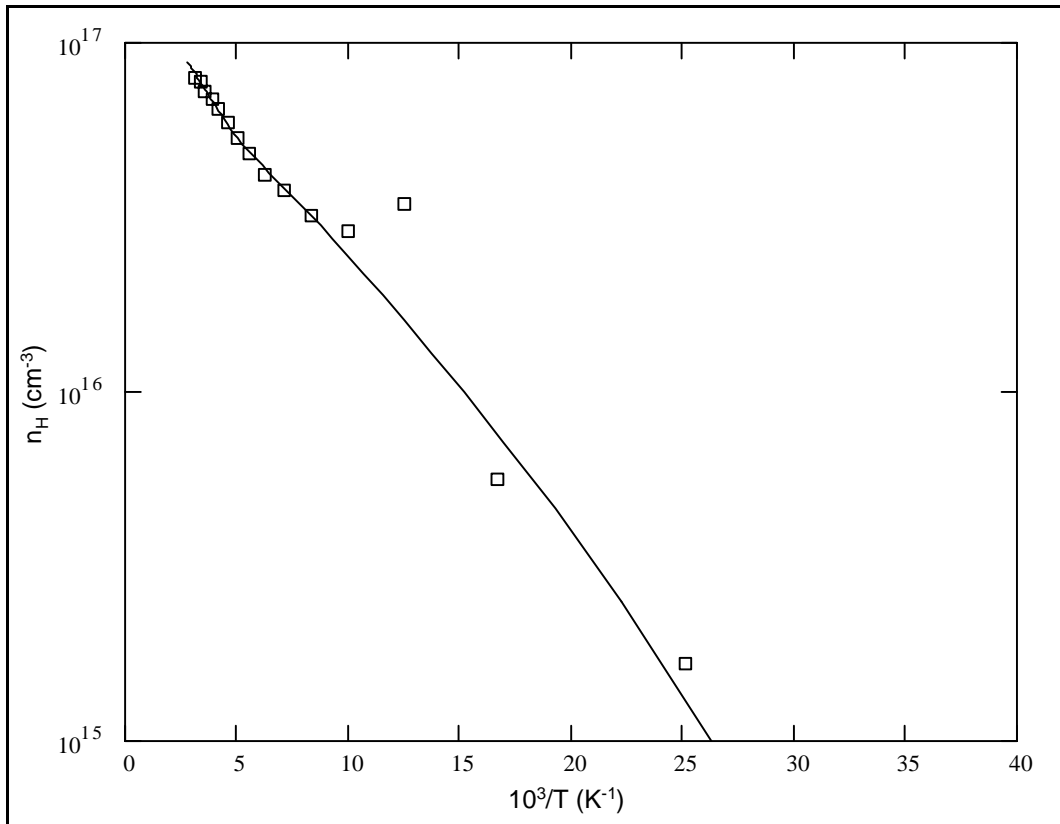


Figure 43. Pre-irradiation temperature dependent Hall data for sample A363. Model (line) is for a two donor fit with ( $N_{D1}=6.3E16$ ,  $E_{D1}=22.9$  meV,  $N_{D2}=5.5E16$ ,  $E_{D2}=79.2$ meV,  $N_A=2.3E15$ ).



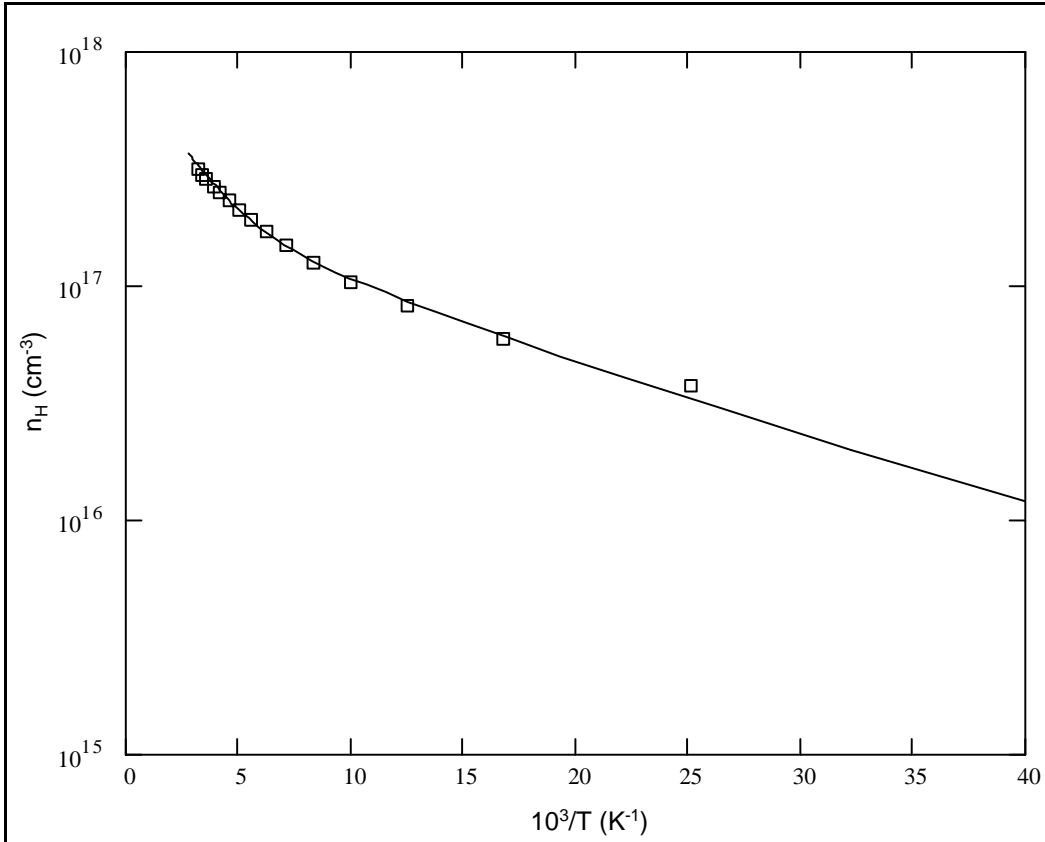


Figure 44. Pre-irradiation temperature dependent Hall data for sample A350. Model (line) is for a two donor fit with ( $N_{D1}=2.18\text{E}17$ ,  $E_{D1}=8.2$  meV,  $N_{D2}=4\text{E}17$ ,  $E_{D2}=50.2\text{meV}$ ,  $N_A=1\text{E}15$ ).

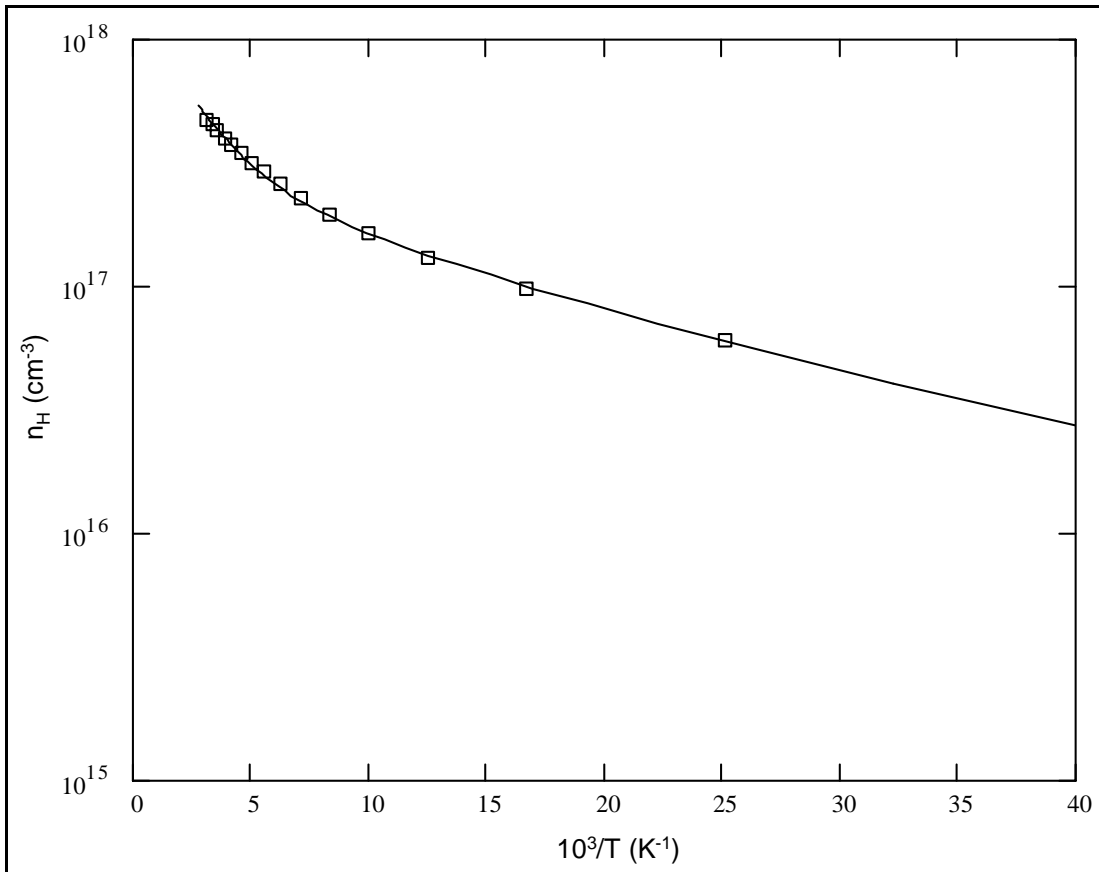


Figure 45. Pre-irradiation temperature dependent Hall data for sample A351. Model (line) is for a two donor fit with ( $N_{D1}=3.58E17$ ,  $E_{D1}=5.7$  meV,  $N_{D2}=6.6E17$ ,  $E_{D2}=47.2$ meV,  $N_A=1.0E15$ ).

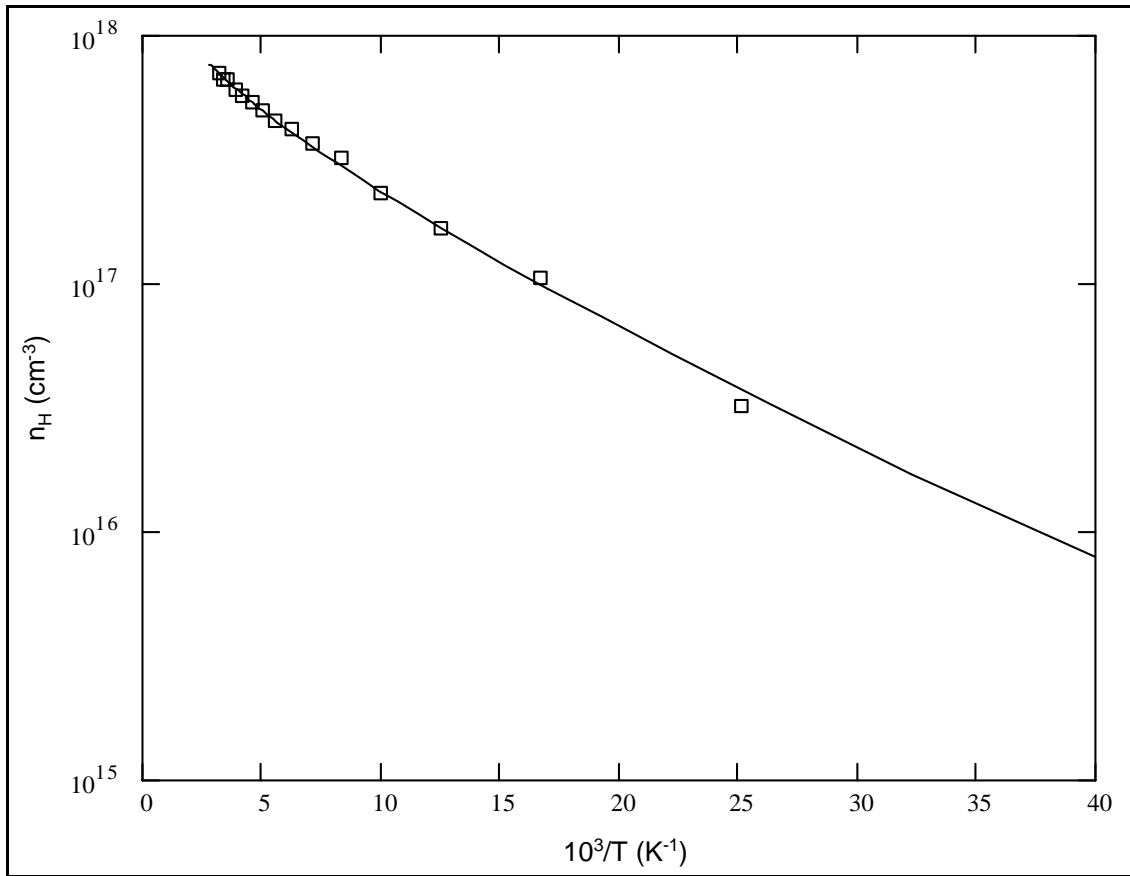


Figure 46. Pre-irradiation temperature dependent Hall data for sample A342. Model (line) is for a two donor fit with ( $N_{D1}=1.28E18$ ,  $E_{D1}=14.2$  meV,  $N_{D2}=5.0E16$ ,  $E_{D2}=79.2$ meV,  $N_A=1.0E16$ ).

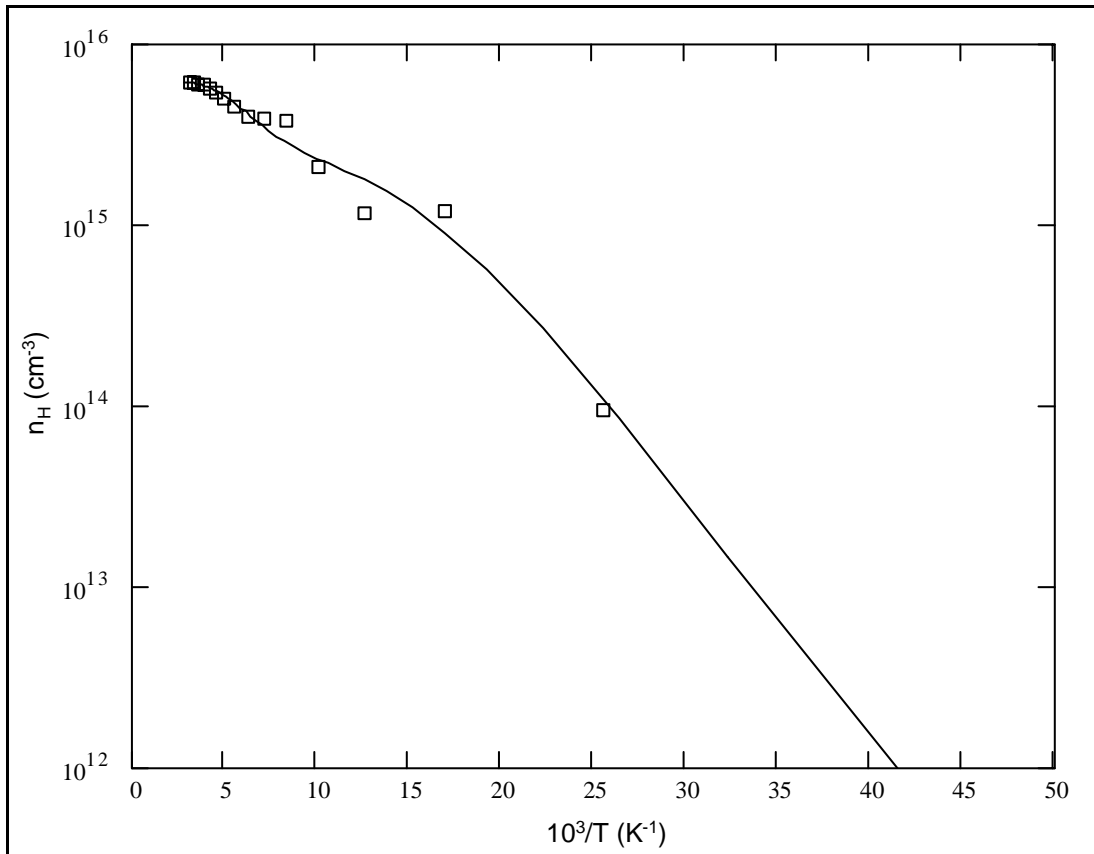


Figure 47. Pre-irradiation temperature dependent Hall data for sample SB0009B. Model (line) is for a two donor fit with ( $N_{D1}=4.8E15$ ,  $E_{D1}=22.0$  meV,  $N_{D2}=3.6E15$ ,  $E_{D2}=70.2$ meV,  $N_A=2.1E15$ ).

Calculated shallow donor concentrations and activation energies derived from the data of Figure 43 through Figure 47 are summarized in Table 10 below.

**Table 10. Calculated donor densities and energies derived from two-donor fit**

Sample	Calculated SD Concentration (cm <sup>-3</sup> )	Calculated SD Activation Energy (meV)
SB0009B	4.8E15	22.0
A363	6.3E16	22.9
A350	2.18E17	8.2
A351	3.58E17	5.7
A342	1.28E18	4.5

## Post-Irradiation Hall Effect Measurements

Samples A342, A350 and A351 were subjected to Hall effect measurements following irradiation at  $10^{17} \text{ e}^-/\text{cm}^2$  and  $10^{18} \text{ e}^-/\text{cm}^2$ . These data were fit using the procedure described above. In general, Hall carrier concentrations fell dramatically after irradiation, as in Figure 48 and Figure 49.

In the higher dose ( $\phi = 10^{18} \text{ e}^- / \text{cm}^2$ ) measurements, the Hall carrier concentration data in each sample show three different slope regimes, indicating the introduction of an intermediate energy donor. Donor fits for both samples were performed using three donors, providing a good match to the experimental data. We will be primarily concerned with the shallowest donors for comparison with EPR data, which would not include this intermediary energy donor given the unshielded activation energy of  $E_{D2} \approx 30 - 50 \text{ meV}$ .

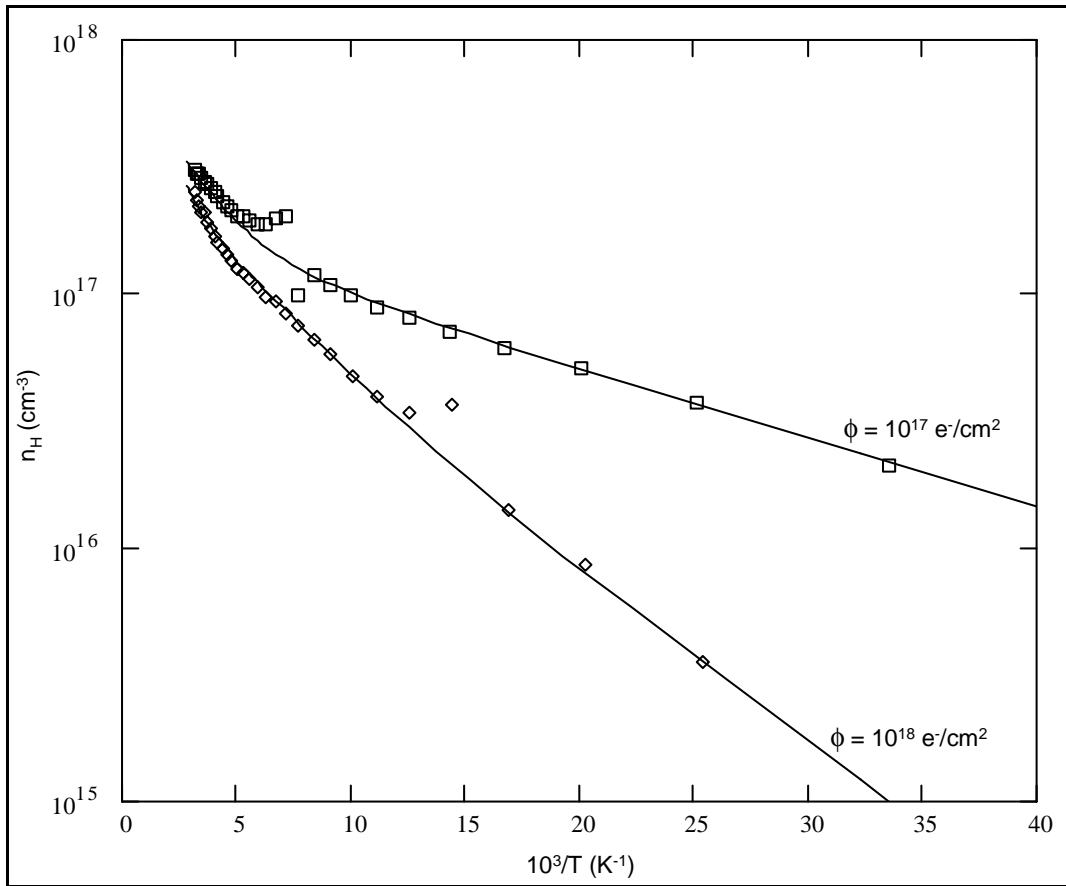


Figure 48. Post-irradiation temperature dependent Hall data for sample A350. For the  $\phi = 10^{17} e^- / cm^2$  case the donor fit yields ( $N_{D1}=1.9E17$ ,  $E_{D1}=6.0$  meV,  $N_{D2}=3.60E17$ ,  $E_{D2}=50$ meV,  $N_A=1.0E16$ ). For the  $\phi = 10^{18} e^- / cm^2$  case, fit parameters are ( $N_{D1}=2.8E16$ ,  $E_{D1}=10.8$  meV,  $N_{D2}=2.10E17$ ,  $E_{D2}=27.5$ meV,  $N_A=1.0E16$ ).

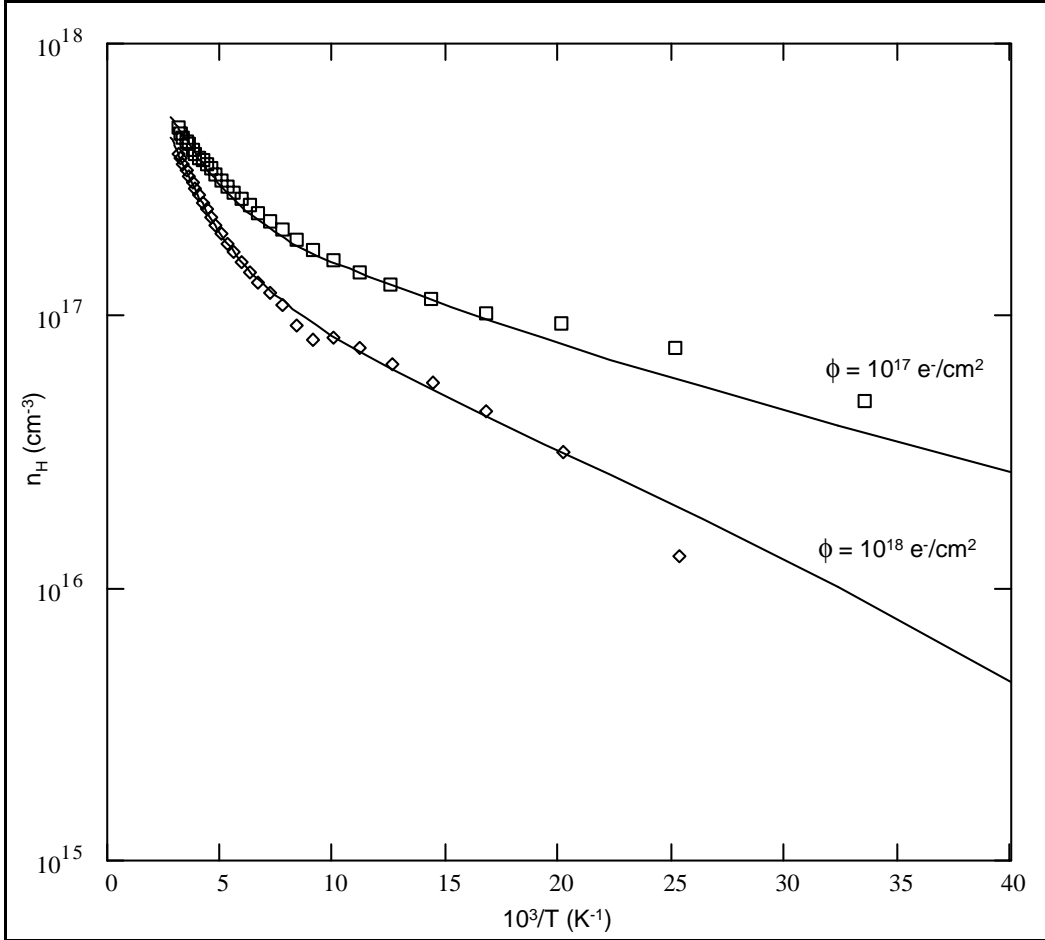


Figure 49. Post-irradiation temperature dependent Hall data for sample A350. For the  $\phi = 10^{17} e^- / cm^2$  case the donor fit yields ( $N_{D1}=3.38e17$ ,  $E_{D1}=5.3$  meV,  $N_{D2}=7.60E17$ ,  $E_{D2}=50.2$ meV,  $N_A=1.0E15$ ). For the  $\phi = 10^{18} e^- / cm^2$  case, fit parameters are ( $N_{D1}=1.65E17$ ,  $E_{D1}=8.5$  meV,  $N_{D2}=1.5E17$ ,  $E_{D2}=31.7$ meV,  $N_A=1.5E16$ ). Low temperature data ( $10^3/T > 25$ ) in this case exhibited instabilities and may not be reliable.

Post irradiation peak carrier mobilities are decreased in all of the samples examined. Mobility reduction is obvious in the high dose sample runs, with the mobilities reduced by a factor of approximately three in sample A350 and a factor of two in sample A351. As shown in figures 50 and 51, the low temperature mobilities are greatly reduced, indicating that defect scattering is the dominant feature as expected.

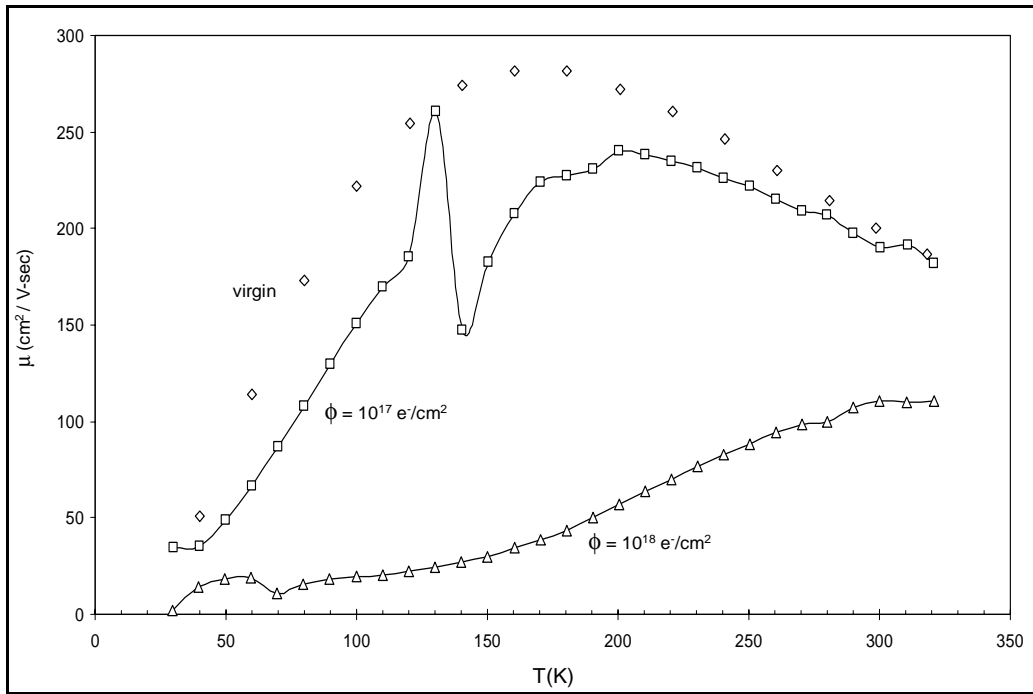


Figure 50. Measured Hall mobility for sample A350, at three different radiation doses.

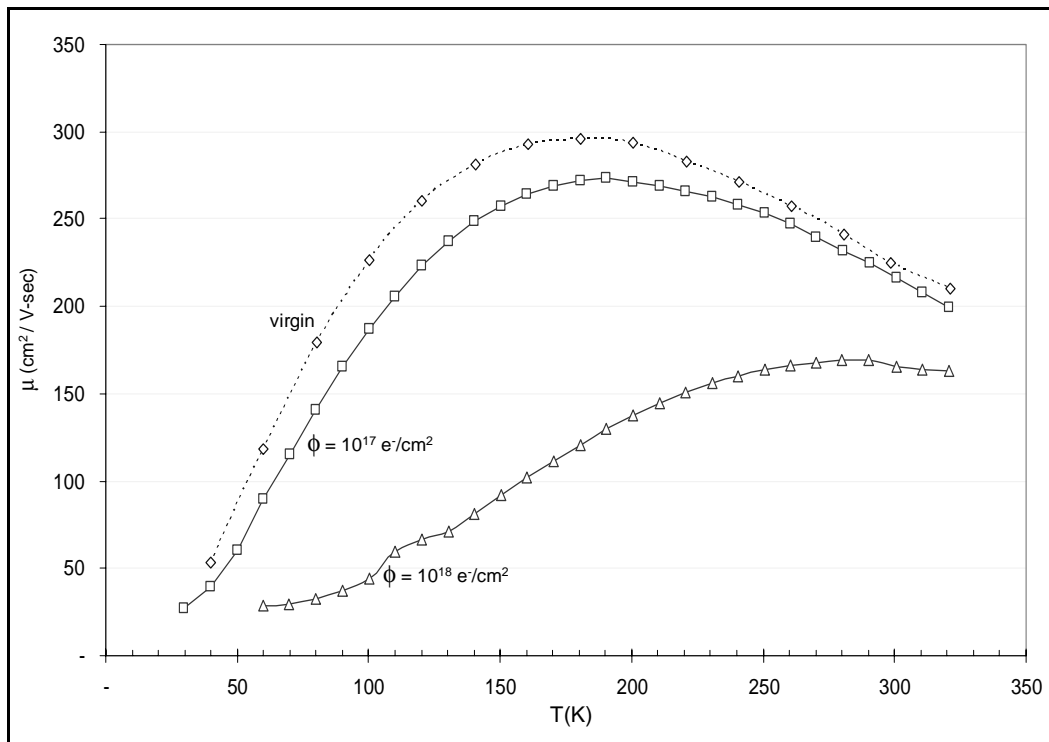


Figure 51. Measured Hall mobility for sample A351, at three different radiation doses.



Unfortunately, with such low mobility samples ( $\mu \leq 400 \text{ cm}^2/\text{V}\cdot\text{sec}$ ) the primary scattering function is presumably the crystal structure quality rather than ionized impurity scattering. This fact limits the use of mobility modeling via numerical solutions of the Boltzmann transport equation [79]. However, it is apparent from the data of Figure 50 and Figure 51 that the greatest impact on the mobility is in the low-temperature regime ( $T < 150\text{K}$ ) which is the region in which ionized impurity scattering dominates, indicating that the introduction of charged scattering sites has resulted from the irradiation.

## VI. Analysis and Discussion

Discussion of the experimental data and analyses leading to the application of the data to understanding radiation interactions with GaN is presented in the following section. This discussion and supporting analyses are presented in three phases: Analysis of Hall effect measurements, discussion and analysis of the EPR data with regards to the shallow donor signal, and analysis of the resolved hyperfine structure noted previously.

### ***Hall Effect Measurements***

Analysis of the donor and carrier concentration data provided via Hall measurements is critical to the proper analysis of the EPR measurements and so will be presented first. While the Hall measurement data is important to the EPR analysis, it is not the primary focus of this research program. In view of the supporting nature of the Hall measurements, precedence is given to analyses which directly support the interpretation of the EPR data. Hall data analyses which bear most directly upon the interpretation of EPR results are determination of the donor activation energies and of the shallow donor concentration. These data will be used to properly quantify the EPR observations of the shallow donor sites and derive the underlying relationships governing radiation interactions with these sites.

The donor concentrations determined by the donor fitting model, outlined in the Theoretical Considerations section, varied by roughly two orders of magnitude across the five primary samples used in this experiment. Over this range, activation energies of the shallow donors were determined to change with the calculated donor concentration in a roughly linear fashion (from about 5meV up to 22 meV) due to ionized donor screening.

The magnitude of this screening effect is parameterized by the value of the *empirical screening parameter* ( $\alpha_D$ ), which is constant for a particular semiconductor material [66]. The variation in the activation energy with donor concentration is given by

$$E_D = E_{D0} - \alpha_D N_D^{1/3} \quad (54)$$

where  $E_{D0}$  is the activation energy in the dilute concentration limit. The value of  $\alpha_D$  reported in the literature via calculation is  $2.1 \times 10^{-5} \text{ meV} - \text{cm}$  [80]; however, measured values of the screening parameter taken from multiple samples reported in the literature yield values ranging from approximately  $2.8 \times 10^{-5} \text{ meV} - \text{cm}$  to  $3.1 \times 10^{-5} \text{ meV} - \text{cm}$  [81]. A linear regression fit of the activation energies versus donor concentrations measured in the current study gives a measured value of the screening parameter of  $3.071 \times 10^{-5} \text{ meV} - \text{cm}$  and a dilute activation energy of  $29.6 \text{ meV}$ .

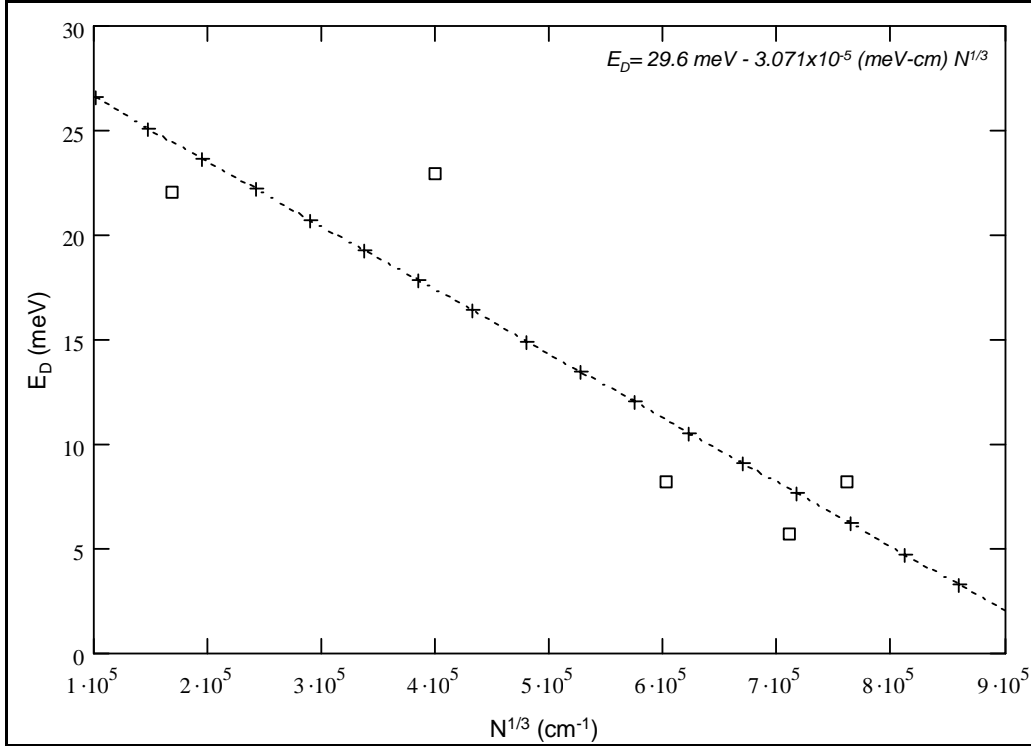


Figure 52. Fit of the empirical screening equation with data from samples SB0009B, A342, A363, A350, and A351. The fit yields values of  $\alpha_D = 3.071 \times 10^{-5} \text{ meV} \cdot \text{cm}$  and  $E_{D0} = 29.6 \text{ meV}$ .

This calculated shallow donor activation energy agrees well with the values of the unscreened activation energy in several studies [67],[34],[80],[81] where reported values vary from 25meV to 30.7meV. The demonstrated agreement with previously measured values of GaN shallow donor activation energy and screening parameter validate the results of the donor fit employed in this study, in which the results are clearly dependent upon the quality of the multilayer correction applied to the Hall data prior to the use of the donor fitting model. Both of these analysis methods are therefore validated by the agreement of these calculated parameters with established values. With the shallow donor fitting and multilayer correction technique validated by measurement of the

accepted  $E_{D0}$  and  $\alpha_D$ , the results of these analyses can be used with some confidence that the underlying analysis is sound.

The pre-irradiation and post-irradiation Hall mobility data discussed previously (samples A350 and A351, figures 50 and 51) were suggestive of the implantation of scattering sites in the material as a result of electron irradiation, although the initial data indicate the actual mobilities are limited by crystalline faults produced during the growth process. Peak low temperature mobilities decrease by approximately 10% and 70% of the pre-irradiation values for fluences of  $10^{17}$  e<sup>-</sup>/cm<sup>2</sup> and  $10^{18}$  e<sup>-</sup>/cm<sup>2</sup> respectively. Since the bulk of the decrease occurs in the lower temperature regime ( $T < 150\text{K}$ ) where ionized impurity scattering is the dominant scattering mechanism in virgin materials [82], it is reasonable to conclude that this mobility reduction is due to an increase in the population of charged defect centers. Without high mobility samples, quantitative data regarding this charged defect concentration is unavailable; even with better samples, modeling of Hall effect measurement data is insufficient to determine the identities of these centers. EPR measurements may be able to identify some of the acceptor states so that a quantitative study may be undertaken.

Post-irradiation Hall effect measurements made on samples A350 and A351 show the same activation energies for the shallow donors ( $< 20$  meV) and generally show donor concentrations that drop as a function of the irradiation dose. Available sample points (A350 and A351) show that the shallow donor concentration drops by approximately 5.5% of the original concentration at  $10^{17}$  e<sup>-</sup>/cm<sup>2</sup> incident fluence and 51.8% of the pre-irradiation concentration at  $10^{18}$  e<sup>-</sup>/cm<sup>2</sup> in sample A351; in sample A350, the corresponding shallow donor concentration reductions are 12.8% and 85.5%,

respectively. In sample A351 the reduction corresponds to a linear function, approximately 1:1 with the incident fluence, and in sample A350 the dose dependence appears to be approximately a ratio of 1:1.5. These linear functions are shown in Figure 53.

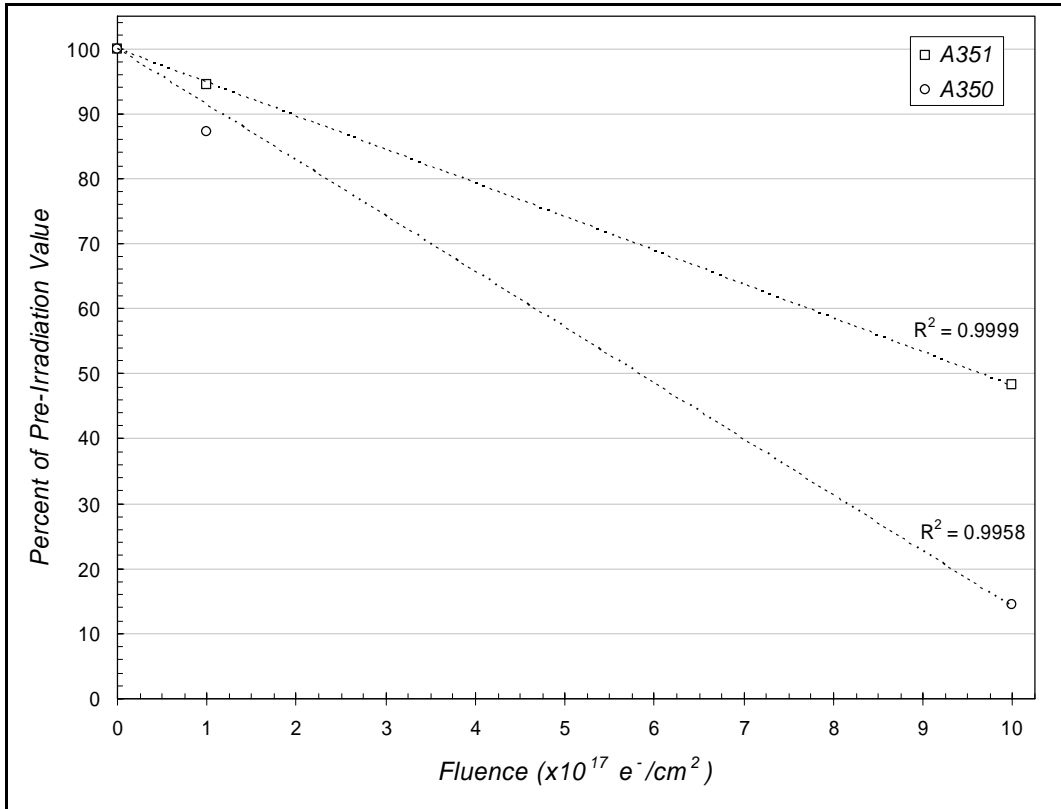


Figure 53. Shallow donor concentrations as a function of the radiation fluence.

### ***EPR Spectroscopy***

EPR spectra of the samples investigated show a linear response in the magnitude of the  $\text{SD}_1$  signal with the calculated shallow donor density. This relationship is noted

only after the  $SD_1$  spectra have been scaled by the  $TO_1$  signal and corrected for the volume differences between samples. After these corrections are applied and the data are compared with the calculated shallow donor concentrations (not the overall carrier concentrations) in the virgin material, the relationship between the measured values of  $SD_1$  integrated area and donor concentration, as determined by modeling of the Hall effect data, are given by

$$Y_{SD1} = (2.262 \times 10^{-17} \text{ cm}^3) N_{SD} \quad (55)$$

where value of the proportionality constant varies with the scaling factors used, being different if a different mass scaling factor were chosen. The correlation coefficient ( $R^2$ ) of this fit is 0.9924, indicating an extremely linear relationship. Supporting data for this relationship are shown in Figure 54. The quality of the linear relationship, expected from a theoretical standpoint, is an indication that the corrections and scalings applied to the data have not resulted in large errors. Similar linear dependences on carrier concentration in the EPR spectra of Si doped GaN has been noted in [83].

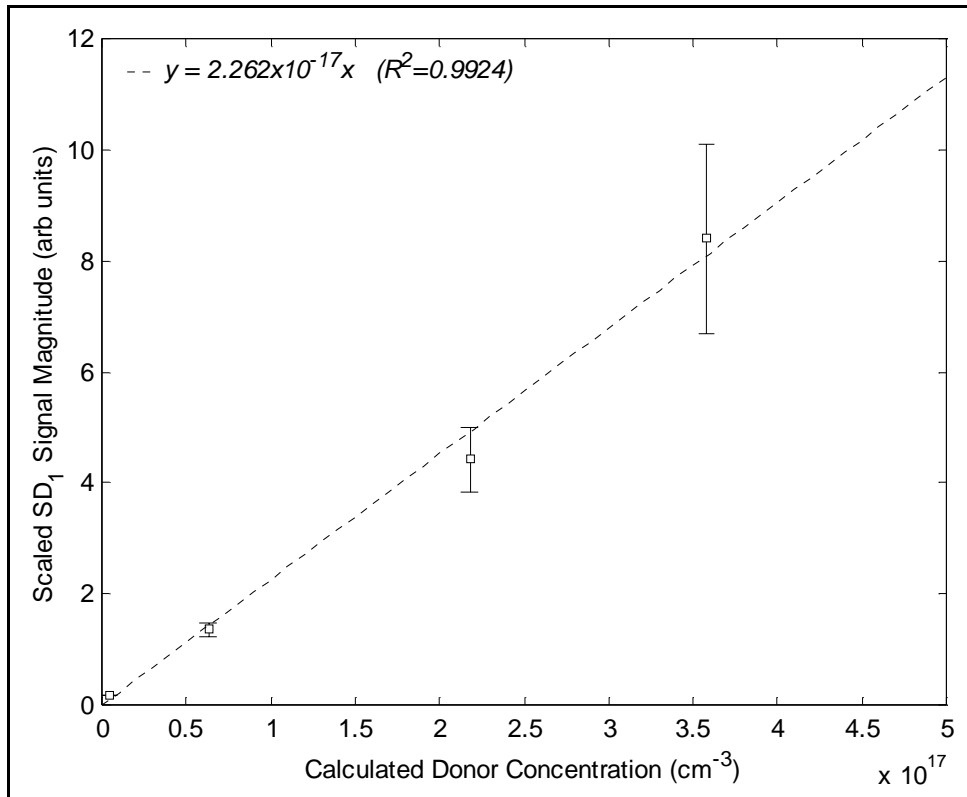


Figure 54.  $\text{SD}_1$  scaled EPR magnitude plotted against the calculated shallow donor concentration. Least squares fit is shown as dotted line.

Measurement uncertainty in the EPR magnitudes was found to increase with increasing  $\text{SD}_1$  signal magnitude. This is not unexpected, since the scaling process involves division by the integrated area of the  $\text{TO}_1$  signal, which is relatively constant in magnitude; therefore, as the  $\text{SD}_1$  signal grows in magnitude the spectrometer's signal channel response scales all of the data down to avoid signal channel overflows and the magnitude of the  $\text{TO}_1$  signal is reduced proportionally. As the  $\text{SD}_1$  signal magnitude increases and the relative magnitude of the  $\text{TO}_1$  signal is decreased, the quality of the fit used to estimate the peak's integrated intensity suffers, increasing the uncertainty in the magnitude of the resulting scaled data.



The demonstrated linear relationship between the EPR signal magnitude and the shallow (29 meV) effective mass donor concentration, as determined by Hall measurement, at 29 meV supports the contention that the EPR  $SD_1$  signal is associated with this Hall donor site. If the  $SD_1$  site were associated with some conglomeration of relatively shallow donor sites, the observed linear relationship would be expected to reflect the changing ratios of the various donor concentrations. The ratios of the two shallowest donors varied from 0.75 to 1.84 in the samples examined; more importantly, the sum of both donor concentrations in sample A351 results in total donor concentrations over  $10^{18} \text{ cm}^{-3}$ , which is incompatible with the good quality EPR spectra taken on this sample.

The single undoped HVPE sample is presented in the previous data set; it falls neatly on the linear fit, although at the lower donor densities ( $\approx 10^{16} \text{ cm}^{-3}$ ) that this sample represents the fit quality is relatively insensitive to large *relative* changes in the donor concentration. Still, the inclusion of the HVPE material in this linear series is suggestive of an underlying relationship. While the donor type in the HVPE sample is certainly different than the Si observed in the MBE samples, the unscreened activation energy in this sample is near 30 meV, consistent with either the nitrogen vacancy defect or the oxygen impurity at 30-35 meV [84]. In either case, the EPR spectra of the shallow donors vary only in the observed linewidth and the assignment of the  $SD_1$  signal to a single shallow donor site may be assumed.

Having demonstrated the linear relationship of the EPR signal magnitude and the corresponding donor concentration, analysis of the post-irradiation EPR data is simplified. The observed reduction of the  $SD_1$  signal can now be confidently linked

directly to a corresponding drop in the concentration of the 29.6 meV donor population. Reduction in the  $SD_1$  signal intensities in all samples following irradiation at an electron fluence of  $10^{18} e^-/cm^2$  was demonstrated in the Experimental Results section, resulting in signal decreases ranging from approximately 50% in the higher donor concentration samples to complete disappearance of the  $SD_1$  signal in the lower donor density samples. This would indicate that the shallow donor concentration has fallen below the  $10^{11}$ - $10^{12} cm^{-3}$  EPR detection threshold.

These EPR results, particularly those in the native GaN samples, immediately indicate that the native shallow donor at  $g \sim 1.95$  *cannot* be due to a simple defect such as the nitrogen vacancy ( $V_N$ ) as proposed by earlier authors [18,85,86], since the primary effect of the irradiation is to induce vacancy – interstitial pairs on both sublattices simultaneously [87]. The production of a defect primarily responsible for the native shallow donor signal ( $V_N$ ) would *increase* the magnitude of the signal, regardless of the intentional doping, whereas the signal magnitude is shown to *decrease* in every instance. This finding is in harmony with more recent theoretical studies, which point toward the inclusion of some sort of impurity doping rather than a native defect [88] and is one of two recent studies which offer experimental evidence for this theory [89]. The HVPE sample results strongly support this assertion, since in the MBE Si doped material the dopant donor states could conceivably mask the effect of the native donor states; no such process is possible in the *undoped* n-type HVPE sample. This result adds to the growing consensus that n-type auto-doping is due to impurities rather than defects.

The decrease of the shallow donor signal points to the interaction of the shallow donor in both doped and intrinsic GaN (whether *intentionally doped* Si, or unintentionally

introduced impurity donors such as O) with a direct radiation product such as vacancies or interstitials. As discussed previously, this interaction can take the form of either compensation of shallow donors due to the formation of stable acceptor traps due to the irradiation or direct interaction of the donors and radiation induced defects via the formation of donor-defect complexes by the oppositely charged donor and mobile defect sites. Obvious candidates for this complexation interaction are interstitials ( $\text{Ga}_i$  or  $\text{N}_i$ ) due to the higher mobility of these defects in comparison to the corresponding vacancies [20]. The results of this study, when combined with the results of lower energy irradiations conducted roughly in parallel by Look [20] point to some combination of donor-defect complexation and acceptor trap compensation. Look's low energy irradiations ( $\approx 300$  keV) were designed to produce nitrogen sublattice damage only; Hall effect measurements in both this study and Look's experiment show similar decreases in shallow donor populations. Single sample Hall data alone are unable to unambiguously determine whether the shallow donor populations are being complexed or compensated; while a series of irradiations on samples with different donor concentrations should be able to identify if the complex formation process is dominant, there is no obvious means to determine the relative contributions of these processes to the donor concentration reduction in the case where both processes are present.

Annihilation of the shallow donor EPR signature is indicative of the direct passivation (transition to a diamagnetic deep state) or compensation of the shallow donor sites, ruling out the possibility of a secondary impurity being forced out of the lattice, as was suggested as a less likely possibility by Look [20]. If a secondary impurity donor such as H were present, and the donor concentration were dropping due to the expulsion

of the donor from the lattice during the irradiation process, then the strong linear dependencies of the EPR data with the fluence and donor concentration would not be expected and, more importantly, the observed room temperature annealing behavior would not occur. The observed post irradiation data of Figure 55 on page 143 indicate that passivation by a radiation induced acceptor state *must* occur, since the post-irradiation measurements indicate a constant level of donor reduction independent of the initial donor concentration. It is important to understand that this constant decrease is a signature of acceptor compensation but does *not* rule out the presence of defect-donor complex formation.

A plausible model for this donor passivation posits the complexation of the single donor state (O or Si) with the nitrogen vacancy, which is expected to be a single acceptor [90], accompanied by compensation of the remaining donor sites by acceptors not involved in the donor-defect complexation process. While this complexation presumably occurs at the irradiation temperatures of 80-100K where many of the shallow donors are ionized, if the complexation process reduces the carrier concentration by transforming these donor sites into deep states this change should be preserved at the EPR measurement temperatures of 4K-10K. The rate constant associated with the formation of defect complexes is expected to be a function of the temperature in two regards: higher temperatures should lead to higher defect mobilities, and at temperatures sufficient to ionize the donor states a coulombic attraction exists between the donor and acceptor sites. This introduces the possibility that the contribution of the compensating acceptor sites may be determined by performing a series of irradiations at different irradiation temperatures to vary the value of the complexation rate constant. This approach would

presumably require lower temperatures than are currently available during irradiation – down to 4.2K or lower to prevent any complexation from occurring.

Regardless of the relative proportions of the two competing processes involved in annihilating the shallow donor sites, when both compensating centers and complexes are present the decrease in the donor concentration scales in a one to one fashion with the total defect concentration up to the saturation point. The difference between the pre-irradiation and post-irradiation data is thus equal to the total defect concentration as discussed earlier. In the case of the  $10^{18} \text{ e}^-/\text{cm}^2$  irradiation, the decrease is determined to be  $2.09 \times 10^{17} \text{ cm}^{-3}$ , which implies a defect introduction rate of approximately  $0.2 \text{ cm}^{-1}$ . This compares favorably with previously measured values using only Hall measurements and with theoretical values [6]. When Hall measurements alone are considered, performed on samples irradiated at fluences of  $10^{17} \text{ e}^- / \text{cm}^2$ ,  $3 \times 10^{17} \text{ e}^- / \text{cm}^2$ , and  $10^{18} \text{ e}^- / \text{cm}^2$  a damage constant of approximately  $0.145 \text{ cm}^{-1}$  is determined, in relatively good agreement with the EPR results.

While the data at the time of this writing are not overwhelming, the observed linear post-irradiation trend, coupled with the observation that the slopes of the pre- and post-irradiation lines are nearly identical, disputes the attribution of the donor decrease to complex formation. For reasonable values of  $\alpha$  (the complex formation rate constant) there should be some differentiable departure from the slope of the pre-irradiation curve. Instead of this behavior, the slopes of the high-dose exposure show an almost exact correspondence to the pre-irradiation values. This is in contrast to Look's explanation of the donor concentration drop as being due solely to complex formation [20]; however, the

irradiations for these two studies were conducted at different temperatures (80K in the present studies, over 300K in Look's study) which could drastically impact the value of the  $\alpha$  parameter. It is quite possible that our measurements exhibit incomplete complex formation and the resulting acceptor compensation, while the complex formation process at higher temperatures proceeds much more quickly, involving the great majority of radiation induced defects in the complex formation process. Since Look's irradiations were performed at lower energies (~350 keV) it is also possible that we are seeing a greater contribution from the action any acceptors produced by Ga sublattice damage.

Our data also indicate some level of room temperature annealing, leading to the belief that the nitrogen interstitial, which should be much more mobile than the corresponding vacancy and has been shown to readily form complexes in GaN [91], is a primary source of any complex formation. Additionally, this defect is expected to act as a single acceptor, and the recombination of vacancy-interstitial pairs at relatively low temperatures (300K) would reduce the compensating acceptor population as well.

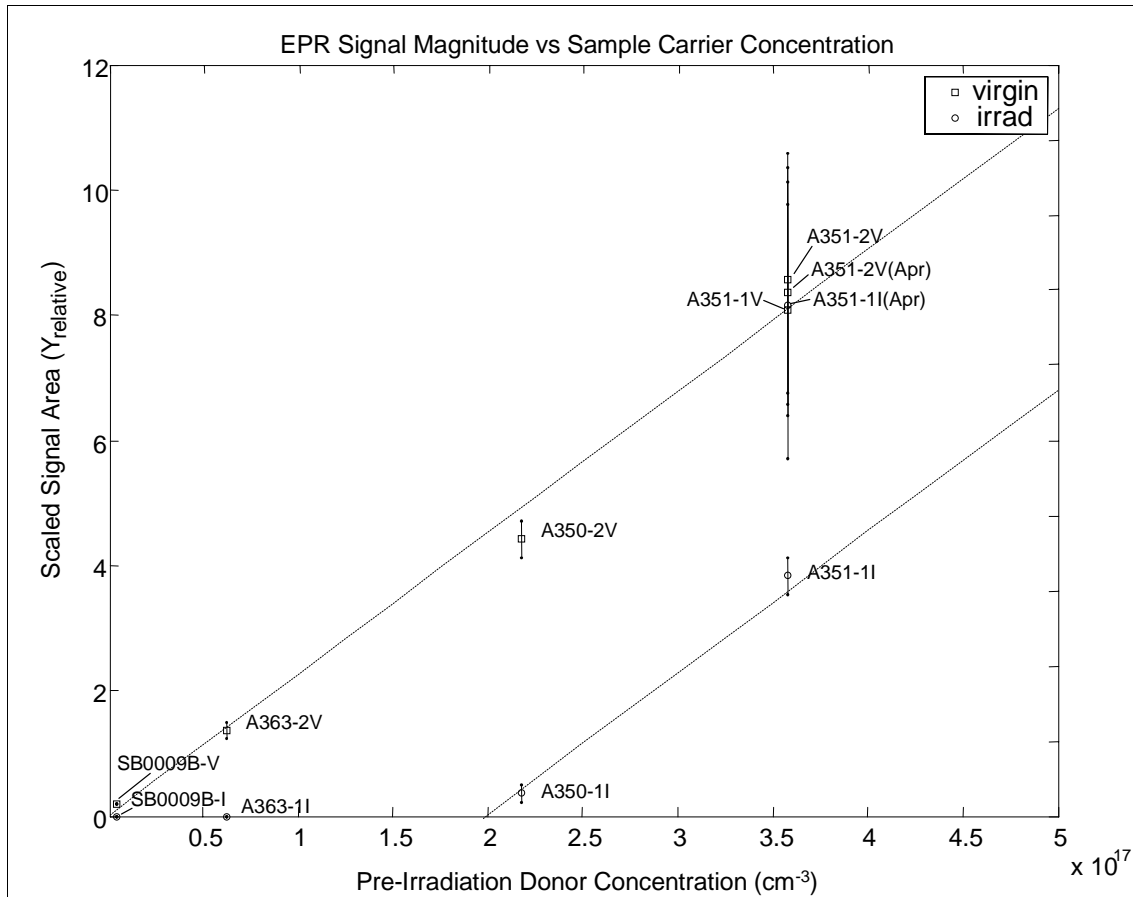


Figure 55. Pre- and post-irradiation values of the scaled EPR signal intensity as a function of the measured Hall carrier concentration. Black stars represent the post-irradiation value predicted for  $\sigma = 2.34 \times 10^{-18} \text{ cm}^2$ . The point labeled A351-1I(Apr) is the only irradiated data point at  $\phi = 10^{17} \text{ e}^- / \text{cm}^2$ , all other irradiated values are at  $\phi = 10^{18} \text{ e}^- / \text{cm}^2$ .

Data from sample A351 also validate the assumption that the ESR signal dependence on *fluence* is governed by equation (20) which predicts a linear relationship between fluence and shallow donor annihilation for low recombination rates. Reduction of the EPR SD<sub>1</sub> signal with increasing doses is demonstrated by the data shown in Figure 56, where the SD<sub>1</sub> peaks are isolated and compared for sample A351 for three values of absorbed dose.

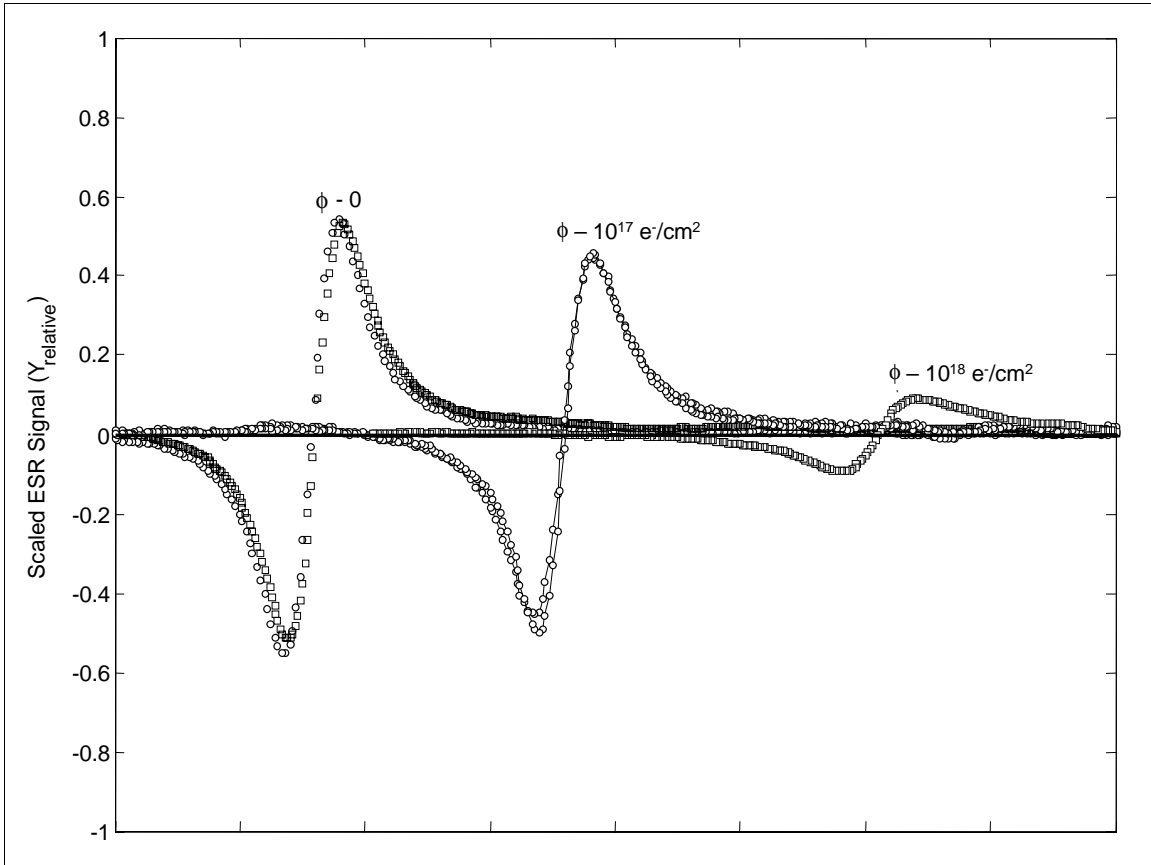


Figure 56. SD<sub>1</sub> spectra in sample A351 at fluences of  $0 e^- / cm^2$ ,  $10^{17} e^- / cm^2$ , and  $10^{18} e^- / cm^2$ . Data marked with filled dots was collected in April 2003 and the data marked with open squares was collected in May 2003. Peaks have been arbitrarily placed along the x axis by varying amounts to ease comparison.

The data of Figure 56 indicate that the SD<sub>1</sub> signal magnitudes decrease in a regular fashion with increasing electron dose; however, the linear relationship is not immediately obvious since the data shown are the measured absorption *derivative* functions. When the integrated peak magnitudes are examined, the data for electron fluences of  $0$ ,  $10^{17}$ , and  $10^{18} e^- / cm^2$  indicate that a linear relationship between fluence and



EPR magnitude exists with slope defined by the radiation damage constant and the spectrometer response function. This dependence is illustrated by the linear fit of Figure 57, which has an  $R^2$  value of 0.9898.

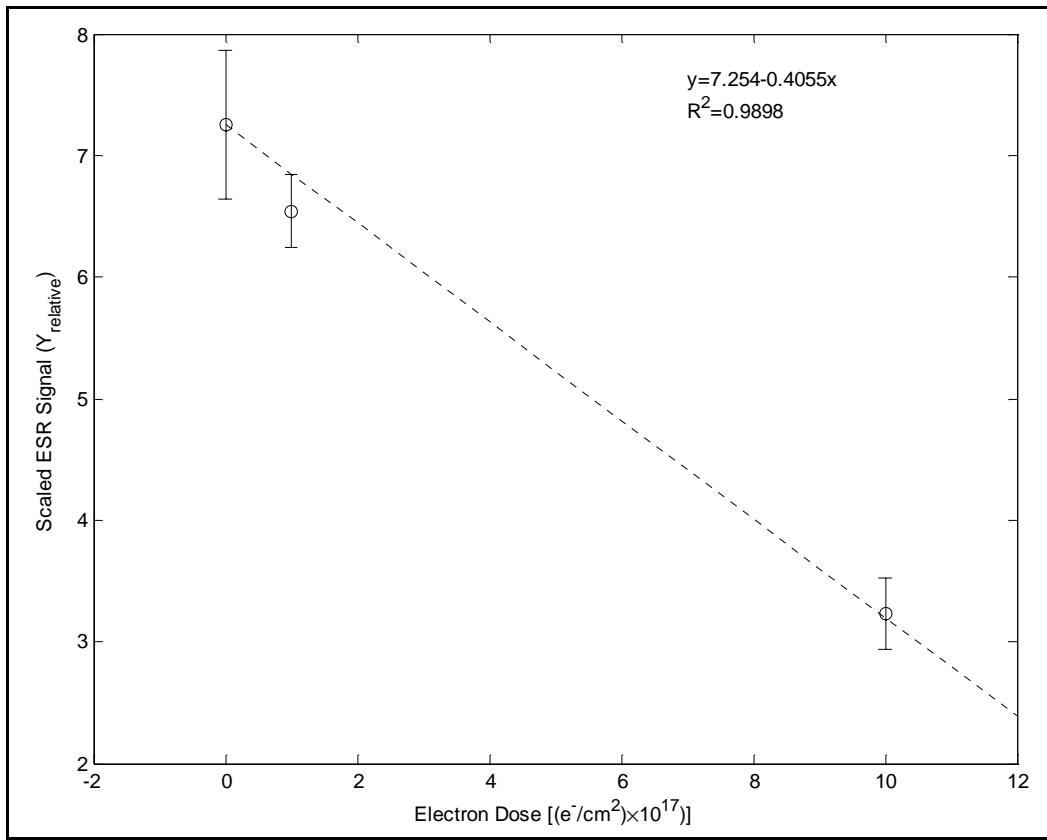


Figure 57. Linear fit to the dose dependence of the shallow donor passivation in sample A351. The  $R^2$  value of the linear fit is 0.9898.

The passivation process is also observed in the Hall effect measurements as well, where the resulting drop in the carrier concentration is seen to decrease after irradiation. In samples A350 and A351 the percentage decrease in the carrier concentration measured

by Hall effect is closely related to the signal magnitude reduction in the EPR measurements, as is shown in Figure 58.

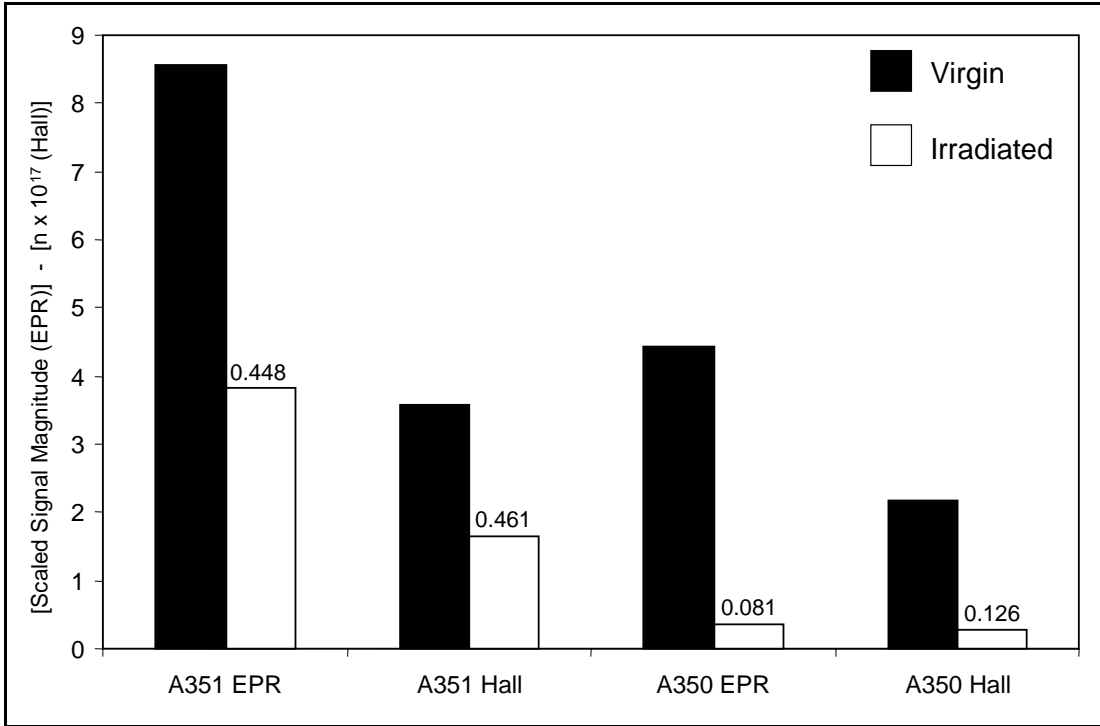


Figure 58. Comparison of EPR  $SD_1$  magnitudes and Hall concentration in A351 and A350, before and after irradiation to  $10^{18} \text{ e}^-/\text{cm}^2$ . The ratio of post-irradiation to pre-irradiation values is shown over the irradiated column in each set.

For sample A350, the Hall carrier concentration due to the 29.6 meV shallow donor decreases by approximately 88.4% following irradiation at a dose of  $10^{18} \text{ e}^-/\text{cm}^2$  whereas the EPR  $SD_1$  signal magnitude decreases by 91.8%. In sample A351, the correspondence is even closer, with the Hall carrier concentration due to the shallow donor dropping by 53.9% and the  $SD_1$  signal decreasing by 55.1%. This correlation is apparent only after the proper scaling is applied to the EPR data and the shallow donor concentration is extracted from the Hall measurements. This is one more indication of the identification of the  $SD_1$  signal as the 30 meV donor. The close degree of correlation

in these measurements is not surprising in a theoretical sense, since these values must scale together; however, in an experimental sense it is gratifying, but somewhat surprising, to observe such a close correlation following the corrections and scaling performed independently on each data set.

The conclusion to be drawn from the above analysis is that the primary effect on the carrier concentration of the sample due to irradiation at these levels is to simply passivate by complex formation and/or compensation of the previously active shallow donors, whether they are a shallow implanted donor or an unintentionally introduced impurity donor. Introduction of additional donors are viewed as second order effects in relation to the magnitude of this passivation process.

Evidence of a third donor in the Hall data occurs at the highest irradiation fluence in samples A350 and A351. Analysis of these data points yields an estimate of the unscreened activation energy of approximately 107-117 meV, which could be associated with the nitrogen vacancy at around 100 meV (see Figure 7, page 23). This assessment is only a suggestion; more data will be required to demonstrate that these are the nitrogen vacancy donor sites.

As alluded to previously, a single annealing data point was collected, representing the degree of SD<sub>1</sub> signal recovery over 17 hours of room temperature exposure, shown in Figure 59. This data point is clearly not intended to be an exhaustive investigation of the annealing behavior, but is indicative of the involvement of some relatively mobile radiation induced defect or defects in the passivation process. The SD<sub>1</sub> signal intensity is demonstrated to recover to approximately 24.1% of the virgin signal strength, an

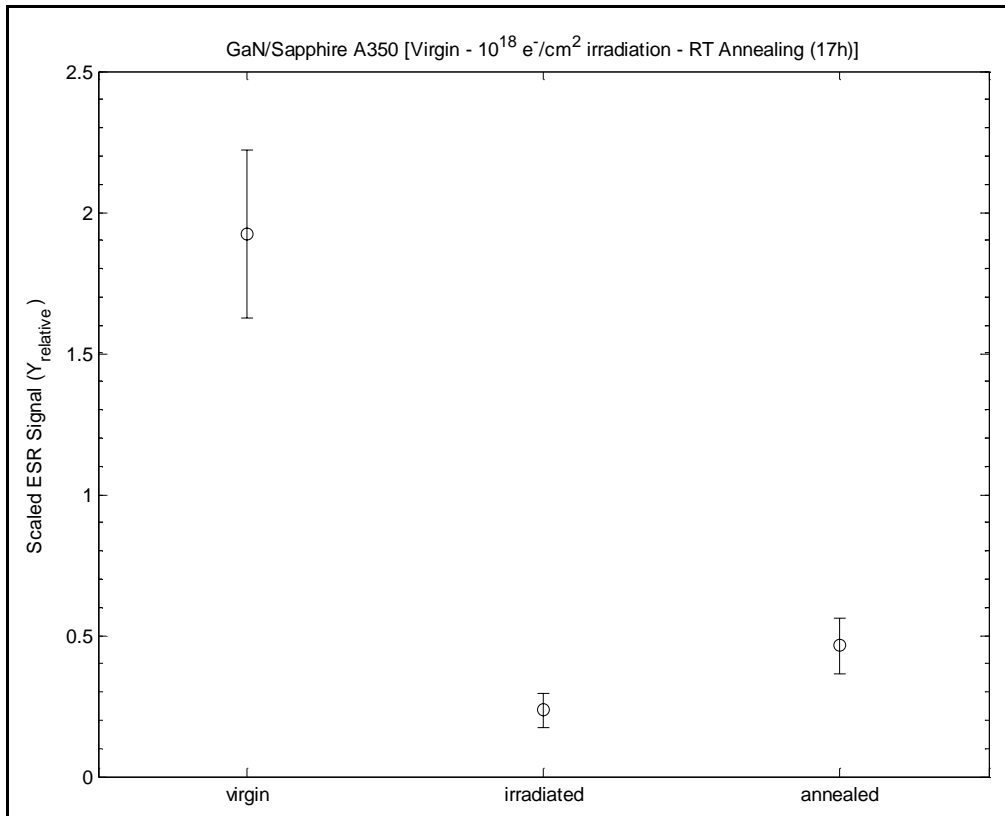


Figure 59. Measured annealing of the radiation effect in sample A350. Annealing was a room temperature over a 17 hour period.

increase of 1.97 times the pre-annealing signal strength of 12.2%.

### ***Hyperfine Structure Analysis***

After noting marked similarity between the data of Figure 37 and Figure 40 and defect hyperfine structure previously measured by EPR in GaAs [92] [93], a hyperfine coupling analysis was conducted. After initially fitting the spectra presented in these reference papers with the Breit-Rabi model to confirm its accuracy as implemented, the spectra observed in this study were fitted using the same general technique.

Analysis of resolved hyperfine structure begins with a determination of the appropriate spin Hamiltonian and proceeds by solving for the resulting eigenvalues,

allowable transitions, and accompanying resonant frequencies. In many cases the Breit-Rabi formula [62] can be used to determine the solutions of the eigenvalue problem.

The development and discussion of this model were presented earlier, and at this point only the application of this model to the observed experimental data will be discussed.

Energy levels of the spin Hamiltonian are computed via the Breit-Rabi formula using the nuclear g-values and nuclear spins for the two stable isotopes of Ga,  $^{69}\text{Ga}$  and  $^{71}\text{Ga}$ , which occur with isotopic abundances of 60.1% and 39.9% respectively. The nuclear parameters of these isotopes were presented in Table 4 on page 33. As discussed previously, the published g-values of the isotopes impose an additional constraint on the data analysis, in that for the  $^{69}\text{Ga} / ^{71}\text{Ga}$  case

$$\frac{{}^{69}A}{{}^{71}A} = \frac{{}^{69}g_N}{{}^{71}g_N} = 0.787 \quad (56)$$

so that the hyperfine coupling constants associated with these isotopes must occur in this constant ratio, no matter their values. Using the nuclear properties of these Ga isotopes, the energy eigenvalues calculated by equation 32 (the Breit-Rabi formula) are computed as a function of the external magnetic field strength. These eigenvalues are plotted in Figure 60 for gallium hyperfine coupling with a single electron. The transition energy of the microwave frequency is calculated ( $E = h(9.5\text{GHz}) = 6.295 \times 10^{-24} \text{ J}$ ) and resonant values of the magnetic field are found numerically, as denoted by the vertical arrows in Figure 60.

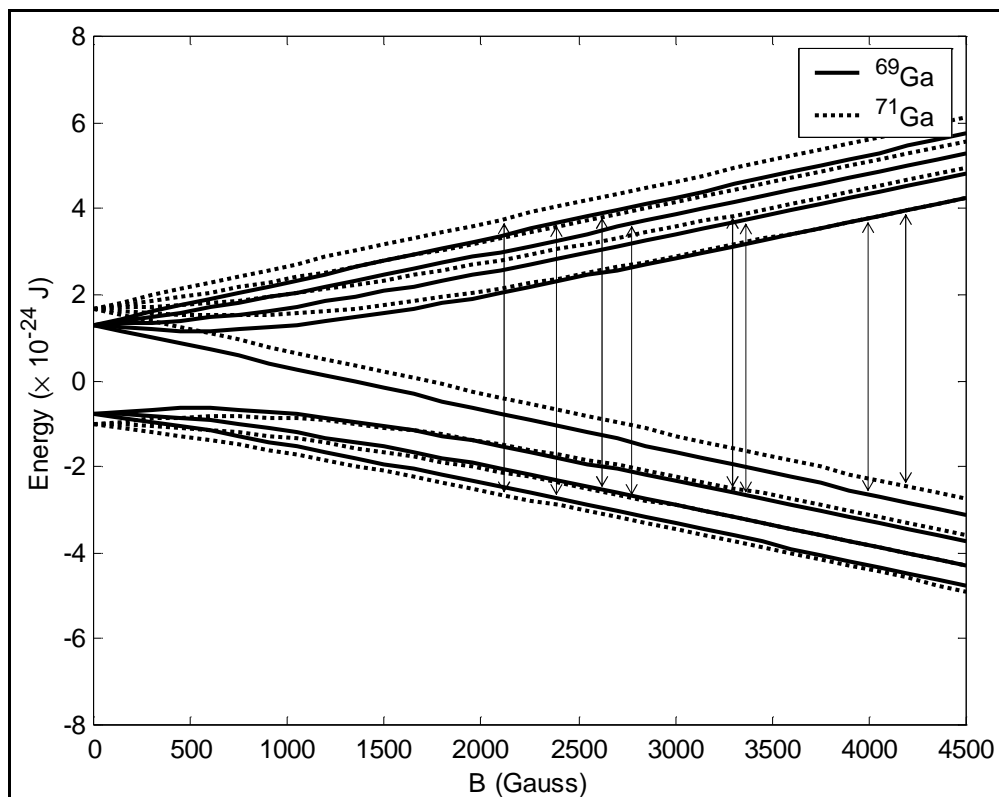


Figure 60. Breit-Rabi levels modeled for  $^{69}\text{Ga}$  and  $^{71}\text{Ga}$ . Vertical arrows represent the resonant magnetic field strengths corresponding to the resonant microwave energy (9.50 GHz)

Resonant field locations having been identified numerically, the model is completed by summing of Gaussian derivative functions centered at each of the resonant field values. These Gaussian derivative functions are summed for each of the isotopic constituents to form a spectrum associated with that isotope, and the resulting isotopic spectra are weighted by the appropriate isotopic abundances and summed as shown in Figure 61 to produce the total absorption spectrum.

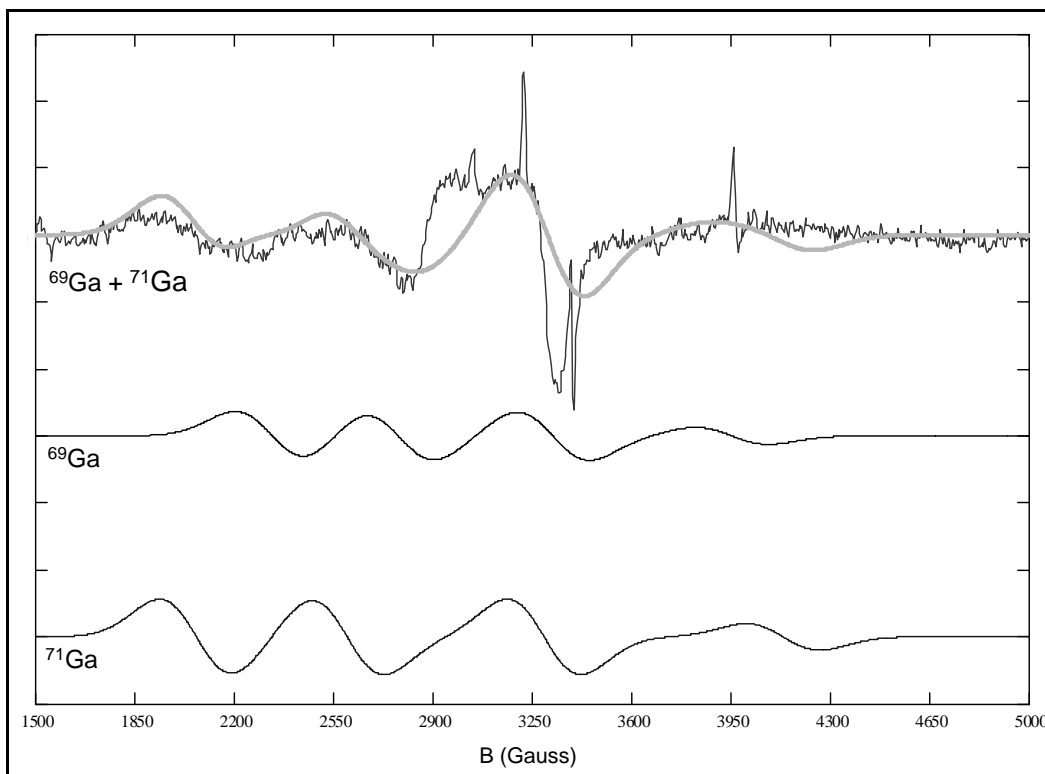


Figure 61. Model output showing placement of equal width Gaussian derivative functions at the calculated resonant field values. Curves are shown for the transitions due to  $^{71}\text{Ga}$  transitions (lower curve),  $^{69}\text{Ga}$  transitions (middle curve), and the weighted sum of these transitions (upper curve) plotted with the experimental data for sample A363.

The final results of the Breit-Rabi analysis are shown in Figure 62 along with the experimental data from sample A363 for comparison. Data for sample SB0009B shows a precisely identical structure, with the high field peaks again being obscured due to greater high field cavity absorption.

Model parameters for both samples (A363 and SB0009B) were found to be identical, with  $g = 2.116 \pm 0.005$ ,  $^{69}A = 0.0530 \pm 0.001 \text{ cm}^{-1}$ ,  $^{70}A = 0.0674 \pm 0.001 \text{ cm}^{-1}$  and a Gaussian line width of approximately 130 G. The ratio of the isotopic hyperfine splitting constants determined above ( $^{69}A / ^{70}A = 0.787$ ) matches the ratio of Ga isotopic

nuclear g-values ( $^{69}g_N / ^{71}g_N = 0.787$ ) and indicates that the splitting observed is due to hyperfine coupling with a Ga atom. Coupling with a Ga atom could indicate any of the following states:

- an electron bound to a gallium interstitial,
- a bound state of a nitrogen vacancy coupling with gallium nearest neighbors, or
- an electron in a bonded state of a complex involving gallium.

Fortunately, literature references exist that have measured similar paramagnetic states in related materials (GaP and AlGaAs) by EPR and in GaN by related techniques.

The similarity of the hyperfine coupling constant determined in this study ( $^{69}A = 1588.9 \pm 30 \text{ MHz}$ ) with that reported by Kennedy and Spencer in AlGaAs via EPR measurements ( $^{69}A = 1498 \pm 30 \text{ MHz}$ ) and identified as a Ga interstitial suggest that the signal under investigation is also Ga interstitial. Furthermore, the observed hyperfine splitting constant is in excellent agreement with values found via ODMR by Linde, et al [94] ( $^{69}A = 1580 \pm 50 \text{ MHz}$ ) and Bozdog, et al [95] ( $^{69}A = 1600 \pm 50 \text{ MHz}$ ) in electron irradiated GaN and attributed by both authors to an interstitial  $Ga_i^{2+}$  atom, possibly complexed with another defect or impurity, due to similarities with previous studies in related materials (GaP [96] and AlGaAs [97]).

An additional absorption signal overlaid with the hyperfine spectrum is noted at  $g=2.2$ ; however, no hyperfine structure is attributable to this spectral feature. It is possible that it may be a signal arising from free nitrogen interstitials or vacancies, which



would be expected to exhibit a much more closely spaced hyperfine structure than for Ga, possibly producing the relatively broad, structureless spectral feature observed.

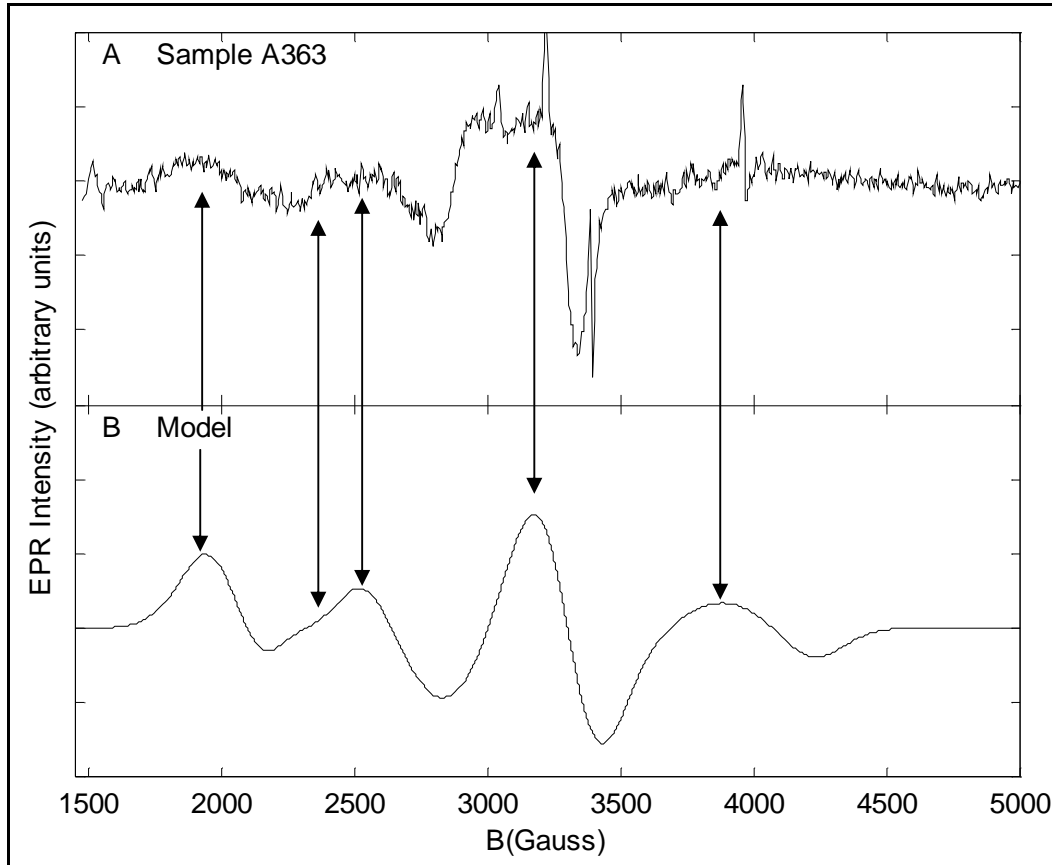


Figure 62. Plot A: Sample A363 widescan data (baseline subtracted). Plot B: Breit-Rabi formula model with  $A_{\parallel}^{69} = 0.0530 \pm 0.001 \text{ cm}^{-1}$  and  $g_{\parallel} = 2.116 \pm 0.005$ , summed for  $^{69}\text{Ga}$  and  $^{71}\text{Ga}$ . Vertical arrows are added to aid in comparison of the plots.

Given the good agreement in the measured hyperfine coupling constants in this study and in previous ODMR work in GaN [94],[95] it is reasonable to conclude that the post-irradiation defect observed here is of the same nature as those observed via ODMR. The observation of the  $Ga_i$  spectrum following irradiation along with the simultaneous passivation of the  $SD_1$  spectral line is a further indication that the passivation of the

dominant shallow donor is due primarily to the action of mobile nitrogen interstitials, although a lack of quantitative data regarding the introduction of the Ga interstitial makes this assessment speculative.

When viewed in light of the observed donor complexation process discussed previously, this observation is particularly exciting. For the first time, a means exists to directly observe the differing rates of Ga and N sublattice damage simultaneously in a single sample.

## VII. Conclusions

### *Experimental Conclusions*

The controversial origin of the native n-type doping in GaN is not due to defect doping by simple point defects, such as the nitrogen vacancy. The primary GaN shallow donor sites with activation energy of 29.6 meV are observed to decrease in density following irradiation in HVPE and MBE grown GaN samples with shallow donor concentrations from  $4.8 \times 10^{15} \text{ cm}^{-3}$  to  $1.38 \times 10^{18} \text{ cm}^{-3}$ , which is incompatible with a point defect source for the native shallow donor. Native n-type doping in GaN thus *must* be impurity-driven, rather than defect-driven.

It is clear from these irradiation studies that the shallow donor sites in GaN are effectively “passivated” as a result of low energy electron irradiation in moderate doses. This passivation is theorized to be the result of compensation by radiation-induced acceptor states (presumably N interstitials), possibly in combination with complex formation between the mobile negatively charged nitrogen interstitial and positively charged shallow donor sites. This theory is supported by:

- the observed dependence of the passivation on the initial shallow donor density,
- the observation of room temperature annealing indicative of a mobile defect,
- the observed reduction in both the Hall measured shallow donor density and accompanying decrease in the EPR absorption peak identified as the shallow donor in GaN,

- and the simultaneous observation of positively identified Ga interstitials in large concentrations in these samples.

Compensation and complexation are presented as competing processes, both of which decrease the shallow donor concentration. Donor-defect complex formation without accompanying acceptor compensation is tentatively rejected as an explanation for the observed donor density reduction based upon the dependence of the reduction on initial donor concentration. Damage constants for this process are determined to be between  $0.145 \text{ cm}^{-1}$  and  $0.209 \text{ cm}^{-1}$  as measured by Hall and EPR respectively.

First observation of the gallium interstitial hyperfine spectrum in GaN is reported and is supported by modeling of the observed spectrum. This defect is observed following high-dose irradiation. The identification of the gallium interstitial spectrum allows direct computation of the defect introduction rate in electron irradiated GaN. With this observation, radiation induced sublattice damage in GaN can be clearly identified and measured in single samples for both sublattices. The first simultaneous identification of gallium and nitrogen sublattice damage effects verifies the prediction that gallium and nitrogen sublattice damage are expected at 1.0 MeV irradiation energies.

### ***Proposed Experimental Direction***

Several avenues of research immediately suggest themselves as a consequence of the data garnered in this experimental effort. A few of the possibilities of highest interest are:

- Measurement of the ratios of passivation ( $N_i$  induced) vs  $Ga_i$  concentration as functions of particle energy, dose, and angle to parametrize sublattice damage

constants. Identification of defect introduction rates on each sublattice as a function of the radiation characteristics is now possible.

- An experimental investigation of radiation effects in different donor density samples with an emphasis on variations in the irradiation temperatures and the use of extremely low temperatures. This could perhaps reveal the relative contributions of acceptor concentration and donor-defect complex formation to the donor density decrease.
- A more thorough annealing study of both defects, to determine sublattice annealing rates and monitor formation of intermediary states
- A more thorough analysis of the Ga interstitial hyperfine spectra including performing angular measurements to identify elements of the hyperfine tensor and background levels in virgin materials.

The measurement and assessment of the gallium and nitrogen interstitial effects in irradiated GaN set the stage for effective, detailed analyses of defect formation and dynamics in GaN through the coupled use of the EPR and Hall experimental methodologies. This effort should be pursued in order to better understand the underlying physical processes governing radiation interactions in GaN materials.

## Bibliography

- 1 Lester Eastman and Umesh Mishra, IEEE Spectrum Online (May 2002), edited by Glenn Zorpette.
- 2 L. Shen, et al, IEEE Elec. Dev. Lett. **22**(10), 457 (2001).
- 3 Yi-Geng Wu, et al, IEEE Elec. Dev. Lett. **48**(3), 586 (2001).
- 4 F. Binet, J.Y. Duboz, E. Rosencher, F. Scholz, and V. Härle, Appl. Phys. Lett. **69**(2), 1202 (1996).
- 5 Thomas Gehrke, Manufacturing GaN, Nitronex Corporation publication.
- 6 D.C. Look, D.C. Reynolds, J.W. Hemsy, J.R. Sizelove, R.L. Jones, and R.J. Molnar, Phys. Rev. Lett. **79**(12), 2273 (1997).
- 7 Committee on the Assessment of Combat Hybrid Power Systems, National Research Council, Combat Hybrid Power System Component Technologies: Technical Challenges and Research Priorities (2003).
- 8 Triangle TechJournal, Nitronex Closes on \$11.3 Million in Funding, August 2003.
- 9 D.C. Look, Z. Fang, and L. Polenta, MRS Internet J. Nitride Semicond. Res. **5S1**, W10.5 (2000).
- 10 Morkoç, Nitride Semiconductors and Devices, Springer Verlag, 1999.
- 11 Chin et al, Journal of Applied Physics, **75**, 7365 (1994).
- 12 Weitzel, Wide Bandgap Semiconductor RF Power Devices, 1997 IEEE Symposium on Compound Semiconductors, pg 479.
- 13 Morkoc et al, Prog. Quant. Electron. **20**, 361 (1996).
- 14 Bougrov et al, Properties of Advanced Semiconductor Materials, Wiley 2001.
- 15 Suzuki et al, Phys. Rev. B, **52** (11), pp 8132 – 8139.
- 16 Fanciulli et al, Phy. Rev. B, **48** (20), pp 15144-15147.

- 17 Suzuki et al, Electron and Hole Effective masses of GaN and AlN, in Properties, Processing and Applications of Gallium Nitride and Related Semiconductors, INSPEC 1999. pp 175-178.
- 18 H.P. Maruska and J.J. Tietjen, Appl. Phys. Lett. **15**, 327 (1969).
- 19 J.E. Van Nostrand, J. Solomon, A. Saxler, Q.H. Xie, D.C. Reynolds, and D.C. Look, J. Appl. Phys, **87(12)**, 8766 (2000).
- 20 D.C. Look, G.C. Farlow, P.J. Drevinsky, D.F. Bliss and J.R. Sizelove, pending publication.
- 21 Y. Nakano and T. Kachi, Appl. Phys. Lett. **79(11)**, 1631 (2001).
- 22 Orton et al, Acceptors in GaN and related compounds, in Properties, Processing and Applications of Gallium Nitride and Related Semiconductors, INSPEC 1999. pp 98-100.
- 23 Keller, et al, IEEE Transaction on Electron Devices **48(3)**, 552.
- 24 Ambacher, et al, J. Appl. Phys. **85(6)**, 3222 (1999).
- 25 Showalter, BMDO Spring Update 2001 Internet Edition, <http://www.acq.osd.mil/bmdo/bmdolink/html/update/spr01/updhor3.htm>.
- 26 S.S. Park, I-W. Park, and S.H. Choh, Jpn. J. Appl. Phys., Part 2 **39**, L1141 (2000).
- 27 Jin-Cheng Zheng, Hui-Qiong Wang, A.T.S. Wee and C.H.A. Huan, Appl. Phys. Lett. **79(11)**, 1643 (2001).
- 28 DenBaars, SP. ITRI, Inc Report: "High Temperature Electronics in Japan", sponsored by Office of Naval Research and National Science Foundation (1998).
- 29 S.C. Jain, M. Willander, J. Nayaran, and R. Van Overstraeten, J. Appl. Phys. **87(3)**, 965 (2000).
- 30 Nasser, et al. Journal of Microwaves and Optoelectronics, **2(3)**, 22 (2001).
- 31 Debasis Sengupta, J. Phys. Chem. B **107(1)**, 297 (2000).
- 32 G.B. Stringfellow, Organometallic Vapor Phase Epitaxy: Theory and Practice (Academic Press, San Diego, 2002).
- 33 Carlos, et al. Phys. Rev. B, **48** (24), 17878 (1993).

- 34 D.C. Look, G.C. Farlow, P.J. Drevinsky, D.F. Bliss, and J.R. Sizelove, pending publication (2003).
- 35 Nord, et al. Nucl. Inst. and Meth. In Phys. Res. B, **202**, 93 (2003).
- 36 Look, DC. Private conversation, 12 April 2002.
- 37 K.H. Chow, G.D. Watkins, V. Härle, and F. Scholz, Phys. Rev. B **55** R10177 (1997).
- 38 D.C. Look, Phys. Stat. Sol. B **228**(1), 293 (2002).
- 39 Atherton, NM Principles of Electron Spin Resonance, edited by Ellis Horwood and T.J. Kemp (Prentice Hall, New York, 1993), pg 1.
- 40 A.R. Boate, J.R. Morton, and K.F. Preston, J. Mag. Res. **24**, 259 (1976).
- 41 B. Bleaney, in Hyperfine Interactions, edited by Arthur J. Freeman and Richard B. Frankel (Academic Press, New York, 1967) chap. 1, pg 41.
- 42 John A. Weil, James R. Bolton, and John E. Wertz, Electron Paramagnetic Resonance: Elementary Theory and Applications (Wiley-Interscience, New York, 1994) pg 386.
- 43 B. Langhanki, Electron Paramagnetic Resonance of Process Induced Defects in Silicon, dissertation, Paderborn University (2001).
- 44 M.W. Bayerl, M.S. Brandt, and M. Stutzmann, Phys. Stat. Sol. (a) **159**(2), R5 (1997).
- 45 John A. Weil, James R. Bolton, and John E. Wertz, Electron Paramagnetic Resonance: Elementary Theory and Applications (Wiley-Interscience, New York, 1994).
- 46 Charles Poole, Electron Spin Resonance: A Comprehensive Treatise on Experimental Techniques (Wiley, New York, 1983).
- 47 Atherton, NM Principles of Electron Spin Resonance, edited by Ellis Horwood and T.J. Kemp (Prentice Hall, New York, 1993), chap 4, pg 130.
- 48 John A. Weil, James R. Bolton, and John E. Wertz, Electron Paramagnetic Resonance: Elementary Theory and Applications (Wiley-Interscience, New York, 1994) App. B, pg 447.
- 49 Atherton, NM Principles of Electron Spin Resonance, edited by Ellis Horwood and T.J. Kemp (Prentice Hall, New York, 1993), chap 4, pg 23.



- 50 Author conversation with Dr. Mary Ellen Zvanut (August 2001).
- 51 Glaser, et al. Phys. Rev. B, **51** (19), 13326 (1995).
- 52 M. Linde, S.J. Uffring, G.D. Watkins, V. Harle, and F. Scholz, Phys. Rev. B, **55** (16), R10177 (1997).
- 53 Bruker Spin Resonance Almanac 2003, published by Bruker Inc.
- 54 John A. Weil, James R. Bolton, and John E. Wertz, Electron Paramagnetic Resonance: Elementary Theory and Applications (Wiley-Interscience, New York, 1994) Ch 3, pg 73.
- 55 Look DC Electrical Characterization of GaAs Materials and Devices (Wiley, Chichester, 1989) pp 1-2.
- 56 M Ahoujja, Y.K. Yeo, R.L. Hengehold, and J.E. Van Nostrand, Appl. Phys. Lett. **80**(8), 1382 (2002).
- 57 Charles Kittel, Introduction to Solid State Physics (John Wiley and Sons, New York, 1966) pg 313.
- 58 H. Boudinov, S.O. Kucheyev, J.S. Williams, C. Jagadish, and G. Li, Appl. Phys. Lett. **78**(7), 943 (2001).
- 59 A.I. Titov and S.O. Kucheyev, J. Appl. Phys. **92**(10), 5740 (2002).
- 60 Atherton, NM Principles of Electron Spin Resonance, edited by Ellis Horwood and T.J. Kemp (Prentice Hall, New York, 1993), chap 2, pp 49-50.
- 61 Cohen-Tannoudji, Diu, Laloë, Quantum Mechanics, (Wiley-Interscience, New York, 1977) pp 643-653.
- 62 G. Breit and I.I. Rabi, Phys. Rev. **38**, 2082 (1931).
- 63 D.A. Steck, Rubidium 87 D Line Data, Theoretical Division Los Alamos National Laboratory (2001).
- 64 Cohen-Tannoudji, Diu, Laloë, Quantum Mechanics, (Wiley-Interscience, New York, 1977) pp 1035-1039.
- 65 Atherton, NM Principles of Electron Spin Resonance, edited by Ellis Horwood and T.J. Kemp (Prentice Hall, New York, 1993), chap 2, pg 321.

- 66 Morkoç H. *Materials Science and Engineering R* **33**, 135-207 (2001).
- 67 Look, DC and Molnar, RJ, *Appl. Phys. Lett.* **70**(25), 3377 (1997).
- 68 Look, DC *Electrical Characterization of GaAs Materials and Devices*, edited by D.V. Morgan and H.L. Grubin (Wiley, Chichester, 1989), pp 107-131.
- 69 S.S. Park, I-W. Park, and S.H. Choh, *Jpn. J. Appl. Phys., Part 2* **39**, L1141 (2000).
- 70 Author conversations with Dr. Gary Farlow, Wright State University (January 2003).
- 71 Integrated TIGER Series of Coupled Electron/Photon Monte Carlo Transport Codes System, Radiation Safety Information Computational Center, Oak Ridge National Laboratory.
- 72 C.A. Bates, J.P. Bentley, B.F. Jones, and W.S. Moore, *J. Phys. C: Solid State Phys.* **3**, 570 (1970).
- 73 Author discussions with Dr. Mary Ellen Zvanut (August 2001).
- 74 Author discussions with Dr. William Carlos, Naval Research Laboratory, Washington DC (October 2002).
- 75 M. Ahoujja, Y.K. Yeo, R.L. Hengehold, and J.E. Van Nostrand, *Appl. Phys. Lett.* **50**(8), 1382 (2002).
- 76 C. Poole Jr and H. Farwell, *Theory of Magnetic Resonance*, (Wiley, New York, 1987).
- 77 F.K. Koschnick, K. Michael, J-M. Spaeth, B. Beaumont and P. Gibart, *MRS Internet J. Nitride Semicond. Res.* **1**, 9 (1996).
- 78 Author discussions with Dr. Bill Carlos, Naval Research Laboratory Washington DC (September 2002).
- 79 Author discussions with Dr. David Look, Wright State University Semiconductor Research Center (August 2003).
- 80 C. Mavroidis, J. Harris, M.J. Kappers, C.J. Humphries, and Z. Bougrioua, *J. Appl. Phys.* **93**(11), 9095 (2003).
- 81 D. Huang, et al, *Solid State Elec.* **45**, 711 (2001).

- 82 Look, DC Electrical Characterization of GaAs Materials and Devices, edited by D.V. Morgan and H.L. Grubin (Wiley, Chichester, 1989), pp 77-78.
- 83 Palczewska, et al. MRS Internet J. Nitride Semicond. Res. **3**, 45 (1998).
- 84 A.J. Ptak, et al, Appl. Phys. Lett. **79**(17), 2740 (2001).
- 85 M. Ilegems and H.C. Montgomery, J. Phys. And Chem. Of Sol. **34**, 885 (1973).
- 86 E.R. Glaser, T.A. Kennedy, H.C. Crookham, J.A. Freitas, Jr, M. Asif Khan, D. T. Olson, and J.N. Kuznia, Appl. Phys. Lett. **63**(19), 2673 (1993).
- 87 Bozdog et al, Phys Rev B, 59(19) 12479 (1999).
- 88 J. Neugebauer and C.G. Van de Walle, Appl. Phys. Lett. **69**, 503 (1996).
- 89 K.D. Greene, J.R. Petrosky, and D.C. Look, pending publication.
- 90 P. Boguslawski, E.L. Briggs, and J. Bernholc, Phys. Rev. B **51**, 17255 (1995).
- 91 K.H. Chow, G.D. Watkins, Akira Usui, and M. Mizuta, Phys. Rev. Lett. **85**(13), 2761 (2000).
- 92 H.J. von Bardeleben and J.C. Bourgoin, Phys. Rev. B **33**(4), 2890 (1986).
- 93 H.J. von Bardeleben, J.C. Bourgoin, and A. Miret, Phys. Rev. B **34**(2), 1360 (1986).
- 94 Matthias Linde, S J Uftring, G D Watkins, V Harle, and F Scholz, Phys. Rev. B **55**(16), R10177 (1997).
- 95 C Bozdog, et al. Phys. Rev. B, **59**(19), 12479 (1999).
- 96 K M Lee, Defects in Electronic Materials, MRS Symposia Proceedings No. 104, edited by M Stavola, SJ Pearton, and G Davies (Materials Research Society, Pittsburgh, 1988).
- 97 A Kennedy and M G Spencer, Phys. Rev. Lett. **57**(21), 2690 (1986).

